



universität
wien

DISSERTATION

Titel der Dissertation

“Elastography as a Hybrid Imaging Technique –
Coupling with Photoacoustics and
Quantitative Imaging”

Verfasser

Thomas Georg Widlak

angestrebter akademischer Grad

Doktor der Naturwissenschaften (Dr.rer.nat)

Wien, April 2015

Studienkennzahl lt. Studienblatt: A 791 405

Dissertationsgebiet lt. Studienblatt: Mathematik

Betreuer: Univ.Prof.DI Dr. Otmar Scherzer

Acknowledgement

The foremost acknowledgement of this thesis goes to the advisor of this work, Prof. Dr. Otmar Scherzer, whose inspiring working environment I joined; thanks to all members of the Computational Science Center! I thank Guillaume Bal and Habib Ammari for accepting to evaluate this doctoral thesis. Indirectly, I am also grateful for the environment of ambition, trust and confidence in the Faculty of Mathematics, fostered by the long-term dean Harald Rindler. My family and friends, whether singing or climbing or both, are also very important. Without them, this work definitely would not be have accomplished with so much joy, belief and support. During my work at the Computational Science Center, I was supported partly by the University of Vienna as a university assistant. Teaching took time, but gave me invaluable insights. Many of the things which the students themselves inspired me to teach them entered, in an indirect way, into the organization of my own work. So I have to be grateful to the students as well. Support from the FWF in project S10505-N20 is acknowledged.

T.W.

to my parents

Contents

I	Preamble	1
<hr/>		
1	Introduction to challenges in elasticity and coupled-physics imaging	5
1.1	From classical to hybrid and coupled-physics imaging methods . .	5
1.2	In quest for the elasticity contrast	7
1.3	Current technologies for elasticity imaging and their output . . .	9
2	The quantitative elasticity imaging problem	13
2.1	Fundamental laws for elastic media	13
2.2	Basic imaging model for elastography	15
2.3	From qualitative to quantitative elastography	15
3	Contribution of the thesis	17
3.1	Setups reframed, strategies adopted and methods employed . . .	17
3.2	Results obtained and outlook	21
3.3	Outline and interrelation of publications	23
II	Publications	25
<hr/>		
4	Stability in the linearized problem of quantitative elastography . . .	27
5	Convergent regularization methods for quantitative elastography . .	63
6	Texture generation for photoacoustic elastography	87
7	Texture generation for compressional photoacoustic elastography .	117
III	Appendix	125
<hr/>		
	Bibliography	127
	Abstracts	138

Part I.

Preamble

Classical medical imaging modalities are known to everyone. Computed tomography, ultrasound imaging and magnetic resonance imaging have been long-standing and successful innovations in science. Their contrast is understood very well by radiologists, the machines and the costs of taking images is constantly being optimized, and the image formation process is mathematically understood since longtimes.

Many functional properties and physiological states of the body, though, cannot be depicted with the classical imaging methods. This disadvantage is tied to the fact that the images depict physical parameters. This restricts the application of classical technologies, so that even with addition of chemical contrast agents, classical imaging remains blind to many diseases.

An example is the stiffness of tissue. As an elastic parameter, it cannot be directly seen in ultrasound or magnetic resonance imaging. The remedy to this situation is the sophisticated coupling of several physical modalities. By this, elasticity imaging, or elastography, is made possible.

This thesis concerns research in the field of elasticity imaging, from an applied mathematics point of view. The preliminary question

$$\text{Why do we map elastic properties of tissue?} \quad (0.1)$$

is exposed in more detail in Section 1.2.

Then comes the prime question in elasticity imaging, which is

$$\text{How can be elastic properties of tissue be mapped?} \quad (0.2)$$

This query is split here into two aspects: One is the engineering aspect. The imaging technologies used to obtain data are discussed in Section 1.3 from a technological point of view. – Another aspect is the mathematical part of elastography. This is discussed in Section 2. We expose several of the mathematical models used in elastography, and present the research fields which are involved.

The last question, most relevant for the reader of the subsequent chapters, is

$$\text{What are the contributions this thesis gives to elastography?} \quad (0.3)$$

This is treated in Section 3 of the introduction, where we give the methods we used in this thesis, the results we obtained, and how they interrelate with the broader field of elasticity imaging.

The thesis itself is cumulative in nature. After the introduction, there follow four chapters which, after preparation in the introduction, can be read separately.

1. Introduction to challenges in elasticity and coupled-physics imaging

1.1. From classical to hybrid and coupled-physics imaging methods

We take a look on three well-known classical imaging modalities. Their mathematical structure is an inverse problem with boundary measurements. Given new challenges to realize imaging of other parameters, we show how novel coupling methods of modalities lead to inverse problems with data in the interior. Elasticity imaging is one of them, and the various forms of qualitative elastography are introduced.

Classical imaging modalities

Computed tomography produces slice images of the body. The physical process underlying is this: X-ray beams, which radially transverse the body, are absorbed by tissue. This effect is exploited for imaging. If we parametrize a line by $\mathbf{x}(s)$, with $0 \leq s \leq S$, then along this line the intensity I of the radiation is described by [95, 118]

$$\partial_s I(\mathbf{x}(s)) = -\kappa(\mathbf{x}(s))I(\mathbf{x}(s)) \quad (1.1)$$

The radiologist wants to look at images of the absorption κ in the interior of the body. To obtain knowledge of this quantity, this is the procedure: One emits radiation $I(0)$ from the boundary into the body. When the radiation beam exits the body, one measures $I(S)$. Then the values $I(0)$ and $I(S)$ are compared and collected for a large amount of lines through the body. Considering the mathematics of the model (1.1), it is then possible to compute the absorption coefficient κ inside the tissue.

Ultrasound imaging is a technology based on emitting and measuring sound waves [95]. Viewing the imaging process in a general form, it is similar to computed tomography: Starting from the equation for a compression wave u , we have the model

$$\nabla \cdot (c(\mathbf{x})\nabla u(\mathbf{x}, t)) = \partial_{tt}u(\mathbf{x}, t) . \quad (1.2)$$

Boundaries of organs in the body manifest themselves in differences in the speed of sound, c . The first goal is therefore to reveal information on the inhom-

1. Introduction to challenges in elasticity and coupled-physics imaging

geneities in $c(\mathbf{x})$. To this purpose, an ultrasound transducer emits a wave from the boundary of the tissue. Then it travels into the tissue. There it is reflected, and travels back to the transducer. The signals are measured, compared and collected. Using physical principles for (1.2), one can compute the interfaces of c .

- The imaging routine converts boundary measurements to a reconstruction of internal parameters.

Magnetic resonance imaging, the third classical modality we mention, is based on specific microscopic effects in protons. These effects are macroscopically measurable in a coil outside the body. The signal in this coil is determined by the magnetization vector field \mathbf{M} . Simplifying, the behavior of \mathbf{M} is described by the Bloch equation [55]

$$\partial_t \mathbf{M} = \gamma \mathbf{M} \times \mathbf{B}. \quad (1.3)$$

Here, γ denotes the *gyromagnetic ratio* specific to hydrogen, and \mathbf{B} is a magnetic field. For imaging, one chooses an excitation by several specific fields \mathbf{B} . The tissue reacts, and one measures $\mathbf{M}|_{\partial\Omega}$ at the boundary of the domain [55, 135]. Using elementary transformations of the measured signal, one can reconstruct $\mathbf{M}|_{\Omega}$ in the interior. The radiologist then looks at the magnitude images $|\mathbf{M}|$.

Each of the problems in (1.1), (1.2), (1.3) is specific. But they all share a general mathematical structure of similar type: A differential operator $\mathcal{A} = \mathcal{A}(\gamma)$ depends on some quantity γ of diagnostic interest, with γ playing the role of κ , c , or \mathbf{M} . The model of the differential equation is completed by initial- or boundary values for a solution \mathbf{v} of a differential equation on a domain Ω (space- or time-dependent). The role of \mathbf{v} is played by I , u , or \mathbf{B} in (1.1), (1.2), (1.3), respectively. Then, a quantity \mathcal{M} depending on γ and \mathbf{v} is measured *at the boundary*:

$$\begin{aligned} \mathcal{A}(\gamma)\mathbf{v} &= 0, & \text{on } \Omega, & \quad \mathcal{B}(\gamma, \mathbf{v}) = \mathbf{g} & \text{on } \partial\Omega \\ \mathcal{M}(\gamma, \mathbf{v}) &= \mathbf{h} & \text{on } \partial\Omega. \end{aligned} \quad (1.4)$$

The inverse problem is to reconstruct from these boundary measurements $\mathcal{M}(\gamma, \mathbf{v})$ the quantity $\gamma|_{\Omega}$. This is an inverse boundary value problem.

New contrast by new technologies

Many physiological parameters like γ are inaccessible by classical imaging modalities, for example:

- optical
- mechanical
- electrical parameters

There exist variants of the inverse boundary value problem (1.4) for these parameters, like diffuse optical tomography, or electrical impedance tomography

1.2. In quest for the elasticity contrast

	Young's modulus E	
bone	18	GPa
liver	0.36-0.58	kPa
breast fat	18-24	kPa
breast tumour	100	kPa

Table 1.1.: The elastic contrast in Young's modulus. Sources: [4, 76, 115, 116]

[3, 15]. But in general, the reconstruction in these boundary value problems yields images of restricted resolution.

A new strategy evolved, which is tied to *hybrid*, or *coupled-physics* imaging methods (see [9, 16]). These methods use a physical coupling between several modalities, for different reconstruction problems [14, 68, 135]. The key point is that these methods exploit *interior data* for the reconstruction of γ . Instead of the boundary inverse problem (1.4), one solves problems of the type

$$\begin{aligned} \mathcal{A}(\gamma)\mathbf{v} &= 0, & \text{on } \Omega, & \quad \mathcal{B}(\gamma, \mathbf{v}) = \mathbf{g} & \text{on } \partial\Omega \\ \mathcal{H}(\gamma, \mathbf{v}) &= \partial^\alpha \gamma \partial^\beta \mathbf{v} & \text{on } \Omega. \end{aligned} \quad (1.5)$$

In contrast to the data \mathcal{M} in (1.4), the information which one starts, is in a way more “ample”. The data \mathcal{H} are given on the whole domain Ω (such that one also speaks of *full-field* data). This is possible only by some additional modality looking “in the inside”. The interior data can be several kinds of combinations of derivatives of γ and \mathbf{v} . The effect is that one has a more favourable setting for reconstructing the parameter γ .

In this work, we consider *elastography* imaging. In the following introductory sections, it is explained what the parameter γ , the operator \mathcal{A} and the measurement operator \mathcal{H} are for elastography. The formal expressions are given in Section 2. The rest of this section provides an informal explanation.

1.2. In quest for the elasticity contrast

The contrast in elasticity

Classical imaging modalities do not depict elastic parameters. Structures, which are harder or stiffer than the surrounding tissue, can therefore not be distinguished by them very well. For example, ultrasound cannot detect hard inclusions in soft tissue, and therefore for diagnosis of breast cancer, other means have to be adopted [116]. On the other hand, X-ray based mammography (which can detect calcifications) has the disadvantages of an overdose of radiation, so here also one relies on alternatives [95].

In clinical practice, physicians use manual examination, e.g., in breast examinations. While palpating the breast, the physician relies on a sensation of “softness”

1. Introduction to challenges in elasticity and coupled-physics imaging

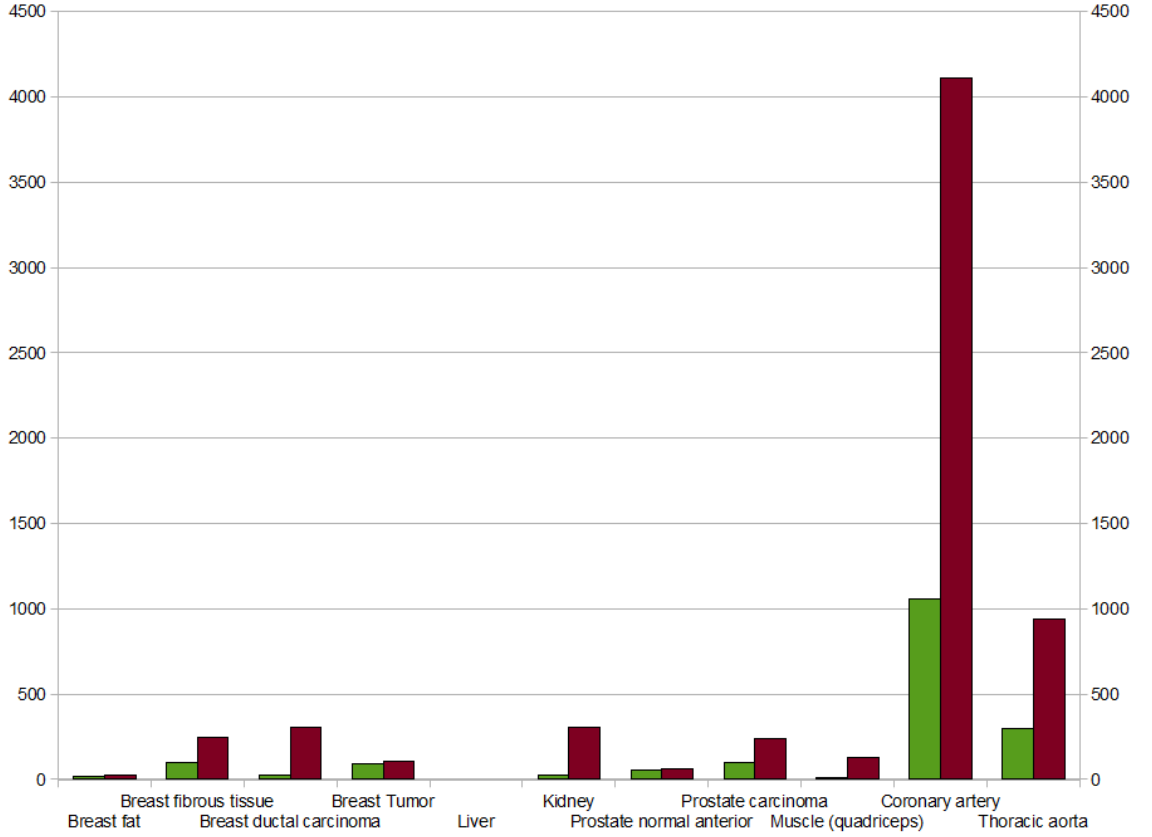


Figure 1.1.: Soft tissue and the contrast of Young's modulus (kPa), green: healthy state, red: malignant state. Sources: [4, 76, 115, 116]

and “stiffness”. Normally, the tissue is soft, which is the healthy state. Hardness or stiffness is related to a thickening of the cellular structures. This condition is often correlated with a pathological state.

If one wants to produce an automatic imaging tool, the sensation of “stiffness” has to be objectified. There are many material parameters in elasticity, but it turns out that the changes relevant for diagnostics are closely related to the so-called *Young's modulus*. The changes in Young's modulus with disease are depicted in Figure 1.1. A comparison is shown in Table 1.1.

The various organs in Figure 1.1 indicate different application areas of elastography. There is marked peak in the graph for the coronary artery. With calcifications and plaque detrimenting the flow of the blood, the artery gets harder. Note that the contrast in Young's modulus between healthy and malignant condition is in a ratio of about 1:4. In fact, this shows that imaging the Young's modulus of the coronary artery could provide an efficient diagnostic tool for the diagnosis of cardiovascular diseases [40].

The idea of elasticity imaging

In short, the idea in medical elasticity imaging is to look at the movements of the tissue through the “glasses” of another modality. If one deforms tissue, this deformation should be directly visible, say, in an ultrasound image. Assume that one particle has, at a particular time, the position $\mathbf{p}(t_1)$ in an ultrasound image. Then assume that it moves to $\mathbf{p}(t_2)$ in the next. One wants to record the quantity $\mathbf{u} = \mathbf{p}(t_2) - \mathbf{p}(t_1)$, which we call the *displacement*.

The goal is to realize an inverse problem with interior data (1.5) with a choice like:

$$\begin{array}{lll} \gamma & \dots & \text{Young's modulus, or a quantity proportional to it} \\ \mathcal{A} & \dots & \text{an operator describing the elastic deformation} \\ \mathcal{H} & \dots & \text{the displacement } \mathbf{u} \text{ of the tissue} \end{array} \quad (1.6)$$

In this way, the problem of elasticity imaging is split into two problems:

- Determine \mathbf{u}
- Determine the Young's modulus from \mathbf{u}

With this, we obtain quantitative information which then should be directly accessible to the clinician.

We mention here, that in contrast to relying on (1.5), elasticity imaging is sometimes realized as inverse problem of type (1.4): This is the case in non-destructive testing, with mechanical boundary measurements [32]. Often, one tries to identify cracks by this method, and there are also a host of new methods aiming at this at a very sophisticated level [10].

1.3. Current technologies for elasticity imaging and their output

The estimation of the displacement \mathbf{u} is referred to as *qualitative elastography*, and the following principle is adopted [40, 106]:

- Record an image in a ground modality
- Perturb the tissue mechanically
- Record a second image

We treat here three technologies and their coupling mechanisms. For a more comprehensive review, see, e.g. [108].

1. Introduction to challenges in elasticity and coupled-physics imaging

Ultrasound elastography

Ultrasound elastography is the oldest elastography technology [75, 103]. It measures components of the displacement field and is based on the coupling assumption that the contrast of the ultrasound image is simply advected by the mechanical deformation [102]. If we consider a whole time series of images $f(t)$, this means that

$$f(\mathbf{x}(t), t) = \text{const.} \quad (1.7)$$

In the image contrast f , a kind of texture is present, which is referred to as *speckle*. Then (1.7), together with additional assumptions, is used to infer one or several components of the corresponding displacement field \mathbf{u} [113, 139].

Magnetic resonance elastography

A first technique in magnetic resonance elastography is this: It was observed that part of tissue motion is invisible in magnitude images $M = |\mathbf{M}(\mathbf{x})|$ because of homogeneous regions. To overcome this limitation, artificial *tags* were introduced in the image [49, 110]. Using condition (1.7) for the tagged image contrast f , motion estimation is made possible in regions where no intensity is initially present. Then one can record the displacement field \mathbf{u} .

Another technique in magnetic resonance elastography is to relate the change of magnetization $\mathbf{M}(\mathbf{x}, t)$ with a displacement field [81, 93]. This is a nontrivial process: One records two vector fields, $\mathbf{g}_1(\mathbf{x}) = M_1(\mathbf{x}) e^{i\varphi(\mathbf{x})}$ (before displacement) and

$$\mathbf{g}_2(\mathbf{x}) = M_2(\mathbf{x} + \mathbf{u}(\mathbf{x})) e^{i\varphi(\mathbf{x}, \mathbf{u}, \mathbf{G})}, \quad (1.8)$$

after mechanical deformation. The magnitude is postulated to be advected with the deformation \mathbf{u} , like in (1.7). For the phase φ of a particle at \mathbf{x} , one has a specific expression $\varphi(\mathbf{x}, \mathbf{u}, \mathbf{G})$, depending on \mathbf{u} and the magnetic gradient field \mathbf{G} [93]. Inverting this relation, a more precise estimation of \mathbf{u} is possible.

Optical coherence elastography

Optical coherence imaging is in many ways the optical analogue of ultrasound imaging. The excitation and measurement is by laser beams, and the primary contrast the refractive index. The beam is sent into the tissue, and it is recorded when it travels back to the boundary. Using condition (1.7) for the contrast in elastography, one can with additional regularization determine a suitable displacement field [65, 94, 121, 127]. Similarly to ultrasound imaging, speckle patterns in the OCT image facilitate the estimation of the displacement \mathbf{u} .

Limitations

By the elastography methods mentioned, one obtains interior data of the displacement field \mathbf{u} . The magnitude of the displacement reveals structures with

1.3. Current technologies for elasticity imaging and their output

high and low stiffness. In regions, where the stiffness is high, the displacement is low. But to make the reconstruction of the Young's modulus precise, the inverse problem (1.5) along the strategy (1.6) has to be defined precisely, and solved. The definition is given in the next section.

2. The quantitative elasticity imaging problem

Elastographic imaging with ultrasound, MRI or OCT imaging, gives as a first step the displacement \mathbf{u} of the tissue. The goal is to reveal information on elastic material characteristics of the tissue. Therefore, the problem has to be quantified with a mathematical model. In this section we introduce a model for this purpose and survey research in in elastic parameter reconstruction from the last decade.

2.1. Fundamental laws for elastic media

Impulse conservation for elastic media

The principal equations for elasticity imaging can be recovered by fundamental principles of continuum mechanics, when applied to elastic media [40, 106].

A basic axiom is the principle of conservation of impulse. With ρ the density of the material, and \mathbf{u} the displacement, the impulse is given by $\rho \partial_t \mathbf{u}$. We assume that there is a surface force \mathbf{T} (the traction vector), and a body force \mathbf{F} . Then the impulse conservation law for a material in domain Ω is given in its integral form by

$$\partial_t \int_{\Omega} \rho \partial_t \mathbf{u} d\mathbf{x} = \int_{\partial\Omega} \mathbf{T} d\mathbf{x} + \int_{\Omega} \rho \mathbf{F} d\mathbf{x} .$$

We write then the traction vector as

$$\mathbf{T} = \sigma \cdot \mathbf{n},$$

Symbol	Denotation	Unit
\mathbf{u}	Displacement	m
\mathbf{T}	Traction	Pa = N/m ²
σ	Stress	Pa = N/m ²
ε	Strain	1
\mathbf{f}	Body force	N/m ³
ρ	Density	kg/m ³
λ	Lamé's first parameter	Pa = N/m ²
E	Young's modulus	Pa = N/m ²
μ	shear modulus	Pa = N/m ²

Table 2.1.: Quantities in elasticity

2. The quantitative elasticity imaging problem

where $\sigma = \sigma_{ij}$ is the stress tensor. Then the divergence theorem can be invoked to obtain the differential form of the impulse conservation:

$$\rho \partial_{tt} \mathbf{u} = \nabla \cdot \sigma + \rho \mathbf{F} \quad (2.1)$$

As body forces are not considered, with \mathbf{F} only imposed forces or excitations enter.

Hooke's law and material parameters in elasticity

Impulse conservation is a basic constituent of any elastic model. The constitutive equations, on the other hand, can be adapted for the relevant application. In elastography, one starts with the linearized strain ε given by

$$\varepsilon(\mathbf{u}) = \frac{1}{2}(\nabla \mathbf{u} + \nabla \mathbf{u}^\top).$$

Then one assumes a linear relation between the stress σ and the strain ε . The basic constitutive equation is Hooke's law,

$$\sigma = C : \varepsilon. \quad (2.2)$$

Here, C is the rank-four elasticity tensor, and operation $:$ is defined as $\sigma_{ij} = \sum_{k,l} C_{ijkl} \varepsilon_{kl}$.

Note that $\varepsilon \neq 0$ distinguishes elastic deformations from rigid deformations. (In a rigid deformation, there are no mutual changes of distance between particles of a body, so ε vanishes.)

In general, one assumes that in an *isotropic* material one can reduce the stress-strain relation according to

$$\sigma_{ij} = 2\mu \varepsilon_{ij} + \lambda \delta_{ij} \nabla \cdot \mathbf{u}, \quad (2.3)$$

with two scalar parameters μ and λ .

Young's modulus (which was discussed in Section 1.2) is denoted by E . It can be related to the shear modulus μ by

$$\mu = \frac{E}{2(1+\nu)},$$

where μ is a parameter referred to as *Poisson's ratio*. In biological tissue, which are nearly incompressible, one has that the value of ν is between 0.49 and 0.5, such that one has

$$\mu \xrightarrow{\nu \rightarrow 0.5} \frac{E}{3}. \quad (2.4)$$

In Section 1.2, we described the principal role of Young's modulus E for diagnostic purposes. Because of (2.4), Young's modulus

$$E \approx 3\mu \quad (2.5)$$

can be assumed to be directly proportional to the shear modulus μ . Therefore, reconstruction of μ gives the relevant diagnostic information for elasticity imaging.

2.2. Basic imaging model for elastography

We combine the impulse conservation principle (2.1) with the constitutive equation for linear isotropic elastic materials (2.3) to obtain

$$\nabla(\lambda \nabla \cdot \mathbf{u}) + 2\nabla \cdot (\mu \varepsilon(\mathbf{u})) + \mathbf{F} = \rho \mathbf{u}_{tt} \quad (2.6)$$

This model unifies most approaches to elasticity imaging and can be used as a basis for the needs of special applications [40, 106].

The most common and easiest setup is *quasi-static imaging*. Here, the specimen is deformed either with a low-frequency force, or statically, e.g., by a piston. In both cases, one can set $\mathbf{u}(\mathbf{x}, t) = \mathbf{u}(\mathbf{x})$, therefore $\mathbf{u}_{tt} = 0$ in (2.6). Depending on the case, one prescribes boundary data $\mathbf{u}|_{\partial\Omega}$, or additionally, a static force \mathbf{F} .

In time-harmonic excitations, model (2.6) is considered with the ansatz $\mathbf{u}(\mathbf{x}, t) = \text{Re}(\mathbf{u}(\mathbf{x})e^{i\omega t})$, and wave equations for the resulting compressional or shear waves can be obtained [40]. One prescribes the ingoing wave and therefore can set $\mathbf{F} = 0$. – In transient excitations, (2.6) is used with a nontrivial \mathbf{F} .

For several purposes, one changes the quantity $\nabla(\lambda \nabla \cdot \mathbf{u})$ in (2.6) by substituting $p = \lambda \nabla \cdot \mathbf{u}$. In many cases, one completely decouples the problem with λ and μ , and considers bodily tissue as incompressible media, $\nabla \cdot \mathbf{u} = 0$. For a domain $\Omega \subset \mathbb{R}^3$, a quasi-static *incompressible* model for elastography is then

$$\begin{aligned} 2\nabla \cdot (\mu \varepsilon(\mathbf{u})) + \mathbf{F} &= 0 \text{ in } \Omega \\ \mathbf{u} &= \mathbf{g} \text{ on } \partial\Omega \end{aligned} \quad (2.7)$$

More complex models are based on other constitutive equations than (2.3) or (4.2). In visco-elastic equations, for example, (4.2) is augmented with an additional time-dependent term [86].

In Chapter 4, models based on (2.6) are considered. In Chapter 5, the model (2.7) will be studied in more detail. This eventually reduces the unknown material parameters to only one, namely the shear modulus μ .

We mention that one can perform several elastic measurements by using different \mathbf{F}_i and \mathbf{g}_i , $1 \leq i \leq k$ in (2.6), resp. (2.7). Then more data \mathbf{u}_i can be collected. In many cases, this facilitates the reconstruction of the shear modulus μ (see Section 3).

2.3. From qualitative to quantitative elastography

To recover the shear modulus μ in (2.6) or (2.7), it is common to split the problem into two parts, which are *qualitative* elastography, and *quantitative* elastography:

Qualitative imaging of the displacement

As mentioned in Section 1.3, the aim in qualitative elastography is to determine the displacement $\mathbf{u}|_{\Omega}$. The basic research question is how and how accurately the

2. The quantitative elasticity imaging problem

displacement can be retrieved from signals or image data in a ground modality. There are many ground modalities and specific techniques for extracting the displacement [106], but often also generic techniques are used, based on (1.7). These generic techniques can be optical flow techniques or block-matching [31, 49, 109, 110, 121], or the correlation technique in [133]. To this part of research, also investigations like [24] pertain, who show that indeed, the diagnostic value of imaging \mathbf{u} is restricted, as it indeed yields only qualitative information (revealing parts where there is ample strain, or no strain at all).

Quantitative imaging of the shear modulus

In quantitative elastography, one determines $\mu|_{\Omega}$. This is the inverse problem of type (1.5). The operator \mathcal{A} is provided by a suitable variant of the operator in (2.6). The measurements \mathcal{H} are one or several displacements $\mathbf{u}_i|_{\Omega}$, $1 \leq i \leq k$ in the domain Ω .

The basic research questions are whether this reconstruction is unique, stable, what algorithms to use and whether the algorithms used to extract the shear modulus are convergent. Uniqueness has, e.g., been investigated for different models in [25, 54, 87, 114]. There are stability analysis for magnetic resonance elastography [131] and [8]. Much of the research is devoted to devise algorithms, or refine existent ones, and analyze them, see e.g. [11, 12, 19, 88, 101, 130]. Given the wealth of algorithmic approaches to the elasticity problem, there are few analyses of convergence of the algorithms. This is a gap the size of which this thesis aims to reduce.

3. Contribution of the thesis

Qualitative elasticity imaging exists since more than 20 years. Quantitative elastography, on the other hand, has gathered more and more attention only in the recent decade.

The new wave with emerging coupled-physics methods gives much inspiration for the treatment of elastography. Ideas from hybrid conductivity imaging, or photo-acoustic imaging, and general regularization techniques have therefore shaped many of the approaches adopted here. In this thesis, we look at qualitative and quantitative elastography from the point of view of other coupled-physics approaches.

In the following, we briefly discuss these methods sketch which results we obtained. The presentation is kept to a technical minimum here, but references for the detailed exposition in the latter parts are given.

3.1. Setups reframed, strategies adopted and methods employed

We discuss the stability approaches to general hybrid imaging problems with interior data. Then we introduce photoacoustic imaging as a ground modality for elastography. In view of the numerical realization, regularization methods are introduced at last.

Overdetermined systems as generic stability approach for hybrid inverse problems

The use of interior information in inverse problems like (1.5) has been observed to yield high contrast with high resolution – in contrast to the corresponding inverse problems using only boundary data like (1.4). The question was raised whether one can give a *generic* mathematical explanation for this phenomenon.

The inverse problem (1.5) is in general a nonlinear problem. One strategy, though, to exhibit the stability of a reconstruction like (1.5) is to use the stability properties of the *linearized inverse problem*. For the linearized problems tools from linear PDE theory can be employed [18, 22, 71, 72].

In several cases, stability of the linearization is formally seen to have the Fredholm property, i.e., for $\mathcal{A} : W \rightarrow Y$ being the linearized forward operator between Banach spaces, one has that there exists a bounded operator \mathcal{R} and a compact

3. Contribution of the thesis

operator \mathcal{T} , such that

$$\mathcal{R}\mathcal{A} = \mathcal{I} - \mathcal{T}. \quad (3.1)$$

This means that \mathcal{R} acts on \mathcal{A} as a *left regularizer*, that is, it inverts \mathcal{A} up to a compact perturbation. We note that this property only entails invertibility up to a finite dimensional kernel.

In [71, 72], a reconstruction problems in conductivity imaging and photoacoustic imaging have been treated. The Fredholm property was shown with the help of pseudodifferential theory. In [18, 22], on the other hand, an general framework was introduced and used using the results on overdetermined systems of partial differential equations in [126]. In this *overdetermined systems approach*, the parameters are considered as variables and the equations for the interior measurement and the forward problem are recast into a single redundant system of partial differential equations. (In this case, the operators \mathcal{A} and \mathcal{H} in (1.5) are, after linearization of the model, put into a single forward operator \mathcal{L} .) Using more measurements, this overdetermined system can be shown to be elliptic. Then, with the results in [126], the Fredholm property (3.1) can be shown.

Whereas previous the previous results using a linearization approach concerned only scalar equations, we wanted to explore and evaluate this method for the vector-valued elastography problem (2.6).

Linearizing (2.6) with respect to μ a reference state, one obtains a linear mapping

$$\mathcal{A}_\mu : \delta\mu \mapsto \delta\mathbf{u}.$$

We adapted the same procedure as in [18], recast the forward problem, and obtained ellipticity criteria and a stability estimate for two experiments $\mathbf{u}_1, \mathbf{u}_2$:

$$\|\delta\mu\|_{l+1} \leq C\|(\delta\mathbf{u}_1, \delta\mathbf{u}_2)\|_{l+2}. \quad (3.2)$$

The ellipticity criteria are conditions on the determinant of the strain :

$$\forall \mathbf{x} \exists i : \det(\mathbf{u}_i(\mathbf{x})) \neq 0.$$

Interestingly, these conditions turn out to be generalizations of the conditions in [19]; a specialization of the condition appears also in a related approach in [8].

Using theory from [86], we were able to show injectivity of the linearized problem $\delta\mu \mapsto \delta\mathbf{u}$. This treatment is contained in Chapter 4 of this work.

The inversion of *nonlinear* problem $\mu \rightarrow \mathbf{u}$ for the model (2.7) is studied in Chapter 5. Here, we connected the results on the linearization to convergence approaches using regularization theory (see below).

Photoacoustic imaging for elastography

The question arises how to obtain interior data $\mathbf{u}|_{\partial\Omega}$ of the mechanical displacement. In this work, this is done using data from photoacoustic imaging, an emerging modality for medical imaging [118]. The synergistic effects of ultrasound elastography and the photoacoustic contrast were already noticed in [43],

3.1. Setups reframed, strategies adopted and methods employed

where the relevant images have been fused for diagnostic purposes. Here we step further and pose the question how *photoacoustic elastography* is possible. – Below, we discuss the image formation process in photoacoustic imaging. We mention briefly the challenges encountered in photoacoustic elastography and the methods by which we overcame them.

The forward model in photoacoustic imaging is given by the wave equation with an initial pressure term f :

$$\begin{aligned}\partial_{tt}p(\mathbf{x}, t) - \Delta p(\mathbf{x}, t) &= 0, & \text{in } \mathbb{R}^n \times (0, \infty), \\ p(\mathbf{x}, 0) &= f(\mathbf{x}), & \text{in } \mathbb{R}^n, \\ p_t(\mathbf{x}, 0) &= 0, & \text{in } \mathbb{R}^n.\end{aligned}\tag{3.3}$$

To reconstruct f from measurements of $p|_{\partial\Omega \times T}$ at detectors outside the object, there exist various reconstruction algorithms [118].

Our goal is to use the reconstructed images f as interior information, and then reconstruct the displacement \mathbf{u} using (1.7). The obstacle is similar to magnetic resonance images: The images do not contain so much texture as in ultrasonic images. A similar issue exists in material science, where displacements should be inferred from objects which are homogeneous in their optical appearance [74, 142].

The solution for photoacoustic elastography is to modify the data $p|_{\partial\Omega \times T}$ in the reconstruction of f and use a band-pass-limited version. The corresponding reconstructions can be shown to be equal to

$$f * \Psi_\varepsilon$$

for a particular convolution kernel Ψ_ε . Then these images are used as a basis for further processing. The prime characteristic of these images is that they reveal texture in the images (and is similar to the speckle-like patterns one has in ultrasound).

A standard method for estimation of motion from images f is optical flow. For this, one starts with the constraint (1.7),

$$f(\mathbf{x}(t), t) = \text{const.}$$

Differentiating with respect to t yields $\nabla f \cdot \mathbf{u} + f_t = 0$, which is known as *optical flow constraint*. In the quasi-static case, we use the constraint

$$\nabla f_1 \cdot \mathbf{u} + (f_2 - f_1) = 0\tag{3.4}$$

and obtain $\mathbf{u}|_\Omega$ by additional regularization (see below eq. (3.11)).

In Chapter 6, we present this method of photoacoustic elastography, together with experiments using simulated data. We show that the introduction of texture into the image acts as a regularization in (3.4).

In Chapter 7, the first measurements using this method are used for the reconstruction. These results were obtained in collaboration with the Medical University of Vienna.

Regularization methods and analysis

For solving an inverse problem in practice, regularization methods have to be employed to deal with the problem of measurement noise. A framework for suitable methods is provided by regularization theory, as exposed, e.g., in [44]. Let $\mathcal{A} : W \rightarrow Y$ be the forward operator between Banach spaces, corresponding to some physical process. One wants to solve the (nonlinear or linear) inverse problem

$$\mathcal{A}x = y. \quad (3.5)$$

For $y \in Y$ in the range of \mathcal{A} , this is possible, and a minimum-norm-solution w^\dagger with

$$w^\dagger = \operatorname{argmin}_W \{ \|w\|_W : \mathcal{A}w = y \} .$$

gives a unique choice. But such a solution is impossible for $y \notin \operatorname{Ran}(\mathcal{A})$. Application of ordinary solution methods (like Newton's method) with noisy y outside the range of \mathcal{A} results in severe artifacts in the reconstructions.

Regularization methods provide a remedy for this situation. Such a method is a family $\{\mathcal{R}^\alpha\}_{\alpha>0}$ of bounded mappings $\mathcal{R}^\alpha : Y \rightarrow W$, which can be applied to noisy measurements y^δ not necessarily in the range of \mathcal{A} . Say that we have $\|y - y^\delta\|_Y < \delta$. The regularization method is said to be *convergent* if, for a sequence y^δ with $\delta \rightarrow 0$, one can choose regularization parameters $\alpha = \alpha(\delta, y^\delta)$ with $\alpha \rightarrow 0$, such that one has in the limit

$$\mathcal{R}^\alpha y^\delta \longrightarrow w^\dagger. \quad (3.6)$$

for $\delta \rightarrow 0$ and $\alpha \rightarrow 0$. – This convergence gives a kind of “consistency” between the regularized solutions $\mathcal{R}^\alpha y^\delta$ for the noisy data y^δ and the best possible solution w^\dagger for the ideal and clean data y .

The use of regularization theory in this work was threefold:

- The most popular regularization method is Tikhonov regularization, which is defined by solving a least-squares problem with a simple penalty term:

$$\mathcal{R}^\alpha y^\delta := \operatorname{argmin} \| \mathcal{A}w - y^\delta \|_Y^2 + \alpha \|w\|_W^2. \quad (3.7)$$

While for linear mappings \mathcal{A} , the properties of this variational problem are well understood, this is not the case for nonlinear problems (e.g. the forward operator $\mu \rightarrow \mathbf{u}$ in model (2.7)). Using the estimate (3.2) and the tools of the geometric theory of G. Chavent [34, 35], we showed well-posedness of the minimization in (3.7) and the convergence property (3.6). This analysis can be read in Chapter 5.

- Another strategy for solving nonlinear problems (3.5) is to employ Newton's method and iteratively compute

$$w_{k+1} = w_k + d\mathcal{A}^{-1}(y - \mathcal{A}(w_k)). \quad (3.8)$$

3.2. Results obtained and outlook

Unfortunately, this does not work well in many inverse problems with y replaced by noisy y^δ , and equation (3.8) has to be solved approximately. This, of course, can be done using Tikhonov regularization: Applying the minimization (3.7) to the Newton iteration (3.8), and doing a short computation, one obtains the iterative prescription of the *Levenberg-Marquardt iteration* (see also [64, 4.1]):

$$w_{k+1}^\delta - w_k^\delta = (d\mathcal{A}^*d\mathcal{A} + \alpha_k \mathbf{Id})^{-1} d\mathcal{A}^*(y^\delta - \mathcal{A}(w_k)). \quad (3.9)$$

Using this iteration, one wants to show that ideally, for decreasing noise level $\delta \rightarrow 0$, there exist parameters $\alpha_{k(\delta)}$ such that

$$w_{k(\delta)}^\delta \rightarrow w^\dagger.$$

Using estimate (3.2) and theory from [59], this convergence property is shown for the quantitative elasticity problem in Chapter 5.

- Interestingly, we could find an interpretation and justification for our texture addition method for photoacoustic elastography from the regularization point of view: For the motion estimation problem in (3.4), the standard method is to use Tikhonov regularization for the optical flow alias the Horn-Schunck model [61]:

$$\mathbf{u} = \underset{\mathbf{v}}{\operatorname{argmin}} \|\nabla f_1 \cdot \mathbf{v} + (f_2 - f_1)\|_{L^2(\Omega)}^2 + \lambda \int_{\Omega} |\nabla_{\mathbf{x}} \mathbf{v}|^2 d\mathbf{x}, \quad (3.10)$$

As mentioned, there is the problem with homogeneous regions and edges. One immediately sees in the formulation that one has some problem with $\nabla f = 0$ in homogeneous regions and $\nabla f \rightarrow \infty$ near edges. We proposed to use different images, therefore different $y^\delta = y^\varepsilon = (f_2 - f_1) * \Psi_\varepsilon$ (which amounts to the perturbation in the data) and a different $\mathcal{A}_\varepsilon = \nabla f_1 * \Psi_\varepsilon$ (this amounts to an additional model perturbation). Then we solved

$$w_{\alpha,\varepsilon} := \operatorname{argmin} \|\mathcal{A}_\varepsilon w - y^\varepsilon\|_Y^2 + \alpha \|w\|_W^2. \quad (3.11)$$

Using [91, Thm.11, p. 21], we showed that for these regularized solutions, one has with $\varepsilon \rightarrow 0$ and $\alpha \rightarrow 0$ the convergence

$$w_{\alpha,\varepsilon} \longrightarrow w^\dagger.$$

This is the third convergence result in this thesis, and it is exposed in Chapter 6.

3.2. Results obtained and outlook

For easier navigation, we collect here the references where the precise formulation of results is to be found in the subsequent text.

3. Contribution of the thesis

- Quantitative elastography linearization,
ellipticity criteria for one and several measurements:
Section 4.4.2 on page 41
- Quantitative elastography linearization,
stability and injectivity results for 2 measurements:
Section 4.4.4 on page 51
- Quantitative elastography,
convergence result for Tikhonov regularization:
Section 5.4 on page 70
- Quantitative elastography,
convergence result for Levenberg Marquardt iteration:
Section 5.5 on page 74
- Quantitative elastography,
reconstructions of shear modulus
Section 5.6 on page 77
- Photoacoustic elastography,
texture introduction into photoacoustic images:
Section 6.5 on page 96
- Photoacoustic elastography,
Interpretation as model-perturbation of Tikhonov regularization:
Section 6.6 on page 99
- Photoacoustic elastography,
qualitative displacement information in simulation experiments:
Section 6.7 on page 104
- Photoacoustic elastography,
displacement information in phantom experiments:
Section 7.2.3 on page 121

Discussion and outlook to further research

In general, the overdetermined theory has been seen as powerful tool for theoretical analysis of hybrid inverse problems, and the connection to other topics in regularization theory have been shown. This opens the door to more convergence analyses, possibly with less requirements on smoothness for other modalities, and it helps to close the gap between mathematical theory and algorithm development. The ellipticity conditions on the displacements \mathbf{u} should be of help in experimental design of elastography setups.

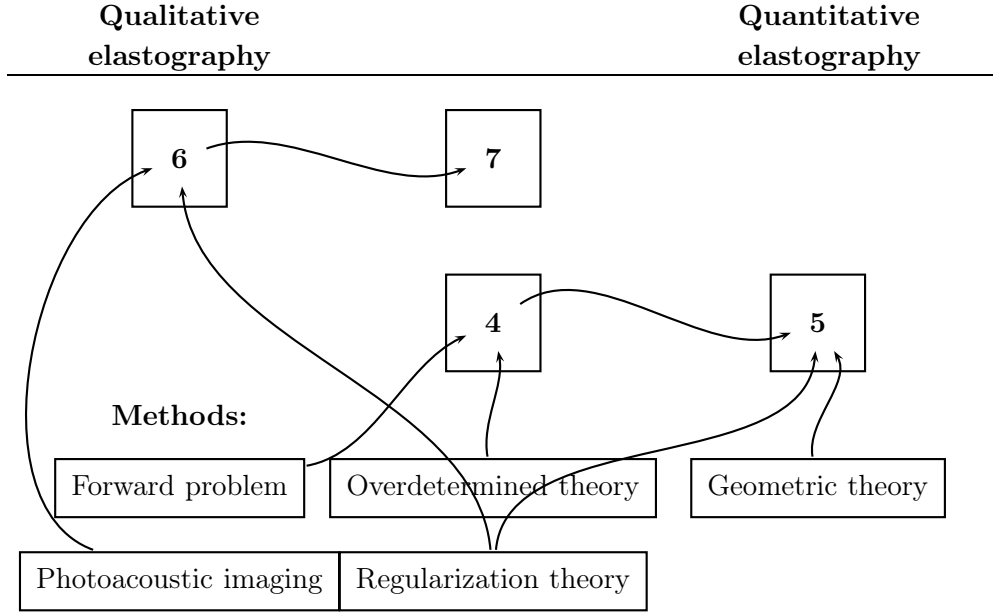


Figure 3.1.: Diagram of interrelations of chapters

The texturization method we developed for photoacoustic elastography shows that, unlike the classical experimental paradigms in photoacoustics, textured data can be used to extract more information from the images than previously thought. Instead of only using image fusion, the photoacoustic contrast can be used for elastography in a genuine coupling.

3.3. Outline and interrelation of publications

In the first part of this thesis, the analysis of quantitative elastography is presented. In Chapter 4, various linearizations of elastic models are introduced and studied, and the stability estimates due to the overdetermined approach are presented. In Chapter 5, these estimates are exploited for deriving convergence results for the quantitative elastography problem. – In the next part, photoacoustic elastography is developed in Chapter 6 and experimentally tested in Chapter 7.

The publications are interrelated as seen in Figure 3.1. From this diagram it also emerges where the different regularization approaches have been applied.¹

¹ Apart from the titles of the subsections in 3.1, two other items appear: Regularity theory such as [86] has been used for the analysis of the elasticity operator, which is denoted as “forward problem” in the diagram. For treating Tikhonov regularization, the “geometric theory” of [34, 35] was used.

Part II.

Publications

4. Stability in the linearized problem of quantitative elastography

Authors & Contributions The authors are TW and O. Scherzer. The development of this article was a gradual, cooperative process, and each of the authors made significant contributions to every aspect of the paper.

Publication status Published, reference [136]. The original publication is available at <http://dx.doi.org/10.1088/0266-5611/31/3/035005>. The version printed here is an extension of this version. This concerns additional material in Sections 4.2.2, 4.2.3, 4.4.3, the table in 4.4.4 and the discussion in Section 4.5.

Abstract:

The goal of quantitative elastography is to identify biomechanical parameters from interior displacement data, which are provided by other modalities, such as ultrasound or magnetic resonance imaging. In this paper, we analyze the stability of several linearized problems in quantitative elastography. Our method is based on the theory of redundant systems of linear partial differential equations. We analyze the ellipticity properties of the corresponding PDE systems augmented with the interior displacement data; we explicitly characterize the kernel of the forward operators and show injectivity for particular linearizations. Stability criteria can then be deduced. While joint reconstruction of all parameters suffers from non-ellipticity even for more measurements, our results show stability of the separate reconstruction of shear modulus, pressure and density; they indicate that singular strain fields should be avoided, and show how additional measurements can help in ensuring stability of particular linearized problems.

Stability in the linearized problem of quantitative elastography

Thomas Widlak¹, Otmar Scherzer^{1,2}

¹ Computational Science Center, University of Vienna,
Oskar-Morgenstern-Platz 1, 1090 Vienna, Austria

² RICAM, Austrian Academy of Sciences,
Altenberger Straße 69, 4040 Linz, Austria

Contents

4.1	Introduction	29
4.2	Modelling quantitative elastography	30
4.3	A result from linear PDE theory	33
4.4	Stability analysis	37
4.5	Discussion	58
4.6	Conclusion	60
4.7	Technical lemmas	60

4.1. Introduction

Elastography is a medical imaging technology; its current applications range from detection of cancer in the breast and in the prostate, liver cirrhosis and characterization of atherosclerotic plaque in hardened coronary vessels [7, 30, 40, 106, 132, 134, 137].

Elastography is based on the fact that tissue has high contrast in biomechanical quantities and the health state of organs is reflected in their elastic properties [4, 67]. The most important parameter for diagnosis is the shear modulus μ , which is the dominant factor in the propagation of shear waves in tissue; shear wave speed in tissue can change up to a factor of 4 with disease [116].

Elastography is performed by coupling with various established imaging techniques, such as ultrasound [75, 103], MRI [81, 93] or OCT [94, 127] – What is common to these elastography techniques is that they provide *interior data* of the displacement $\mathbf{u}|_{\Omega}$ of the tissue on the imaging domain Ω . According to the specific excitation used, \mathbf{u} can be space or space-time-dependent (both cases are considered in this work).

In some applications, knowledge of the displacement \mathbf{u} already gives qualitative diagnostic information (see, e.g., [141] for a dermatological application). More accurate information is provided by quantitative information of the underlying biomechanical parameters. For this, one formulates the elasticity problem as a model; various models based on linear elasticity, viscoelasticity or hyperelasticity have been considered for elastography [40].

To recover the material parameters, an inverse problem based on an elasticity model has to be solved. Given the displacement \mathbf{u} , the mathematical problems in *quantitative elastography* are the recovery of parameters such as the Lamé parameter λ , the shear modulus μ , the density ρ , or recovery of the shear wave speed $\sqrt{\frac{\mu}{\rho}}$ [24, 40]. These problems are non-linear inverse problems.

Much effort in elastography research has been concerned with developing adequate numerical inversion schemes for all kind of experimental varieties of elastography (see, e.g., [11, 54, 83, 84, 85] and the reviews in [40, 124]). Among the proposed algorithms, optimization procedures, which need the linearized inverse problem, form an important class.

Mathematical results about uniqueness and stability of the inverse problems in elastography have been gathered recently, mostly for the simplest models in linear elasticity. In [63, 87], it was proved, that – given one piece of dynamic interior information \mathbf{u} subject to restrictions such as $\mathbf{u} \neq 0$ –, one can uniquely recover material parameters. Other uniqueness results have been reported in [25] for two and more measurements, and in [114] for a hyperelastic model. The recent paper [20] showed unique reconstruction of λ and μ given two sets of exact measurements subject to some non-trivial conditions on the displacements. The stability of the nonlinear problem has been studied in [20] using ODE-based and variational tools.

4. Stability in the linearized problem of quantitative elastography

Elastography can be seen as part of *hybrid* (or coupled-physics) imaging methods (see [14] and the discussion in [82]). The coupling phenomenon can be simple advection for ultrasound and OCT elastography, or a more complicated coupling in magnetic resonance elastography [81].

The body of literature in hybrid or coupled-physics imaging centers on novel imaging methods involving more than one physical modality; emphasis is laid upon the quantitative imaging problems for mechanical, optical or electrical parameters that have high diagnostic contrast. For reviews on the typical problems in coupled-physics imaging, see [9, 14, 16, 68, 69, 135].

In many hybrid inverse problems, high resolution in the reconstructions was observed. To explain the high resolution in a unified manner, a general strategy is to linearize the corresponding nonlinear quantitative problems. Then the stability properties of the linearized problem have been treated with tools of linear PDE theory [18, 22, 71, 72]. In [71], problems in conductivity imaging and quantitative photoacoustic imaging were treated. The linearized forward operators were studied with pseudodifferential theory and shown to be Fredholm, i.e., with stable inversion up to a finite-dimensional kernel. In [18], a general framework was proposed for treating linearizations of quantitative problems with interior data; in this method, the parameters are considered as variables and the information is recast into a single redundant PDE system, to which theory such as [126] is applied. This method was applied to the power density problem in [18] and to the problem of acousto-optic imaging in [22]. In these analyses, information from multiple experiments has been assumed, as the ellipticity condition was easier to obtain in this case.

In this article, we treat the linearized problem in quantitative elastography using the general coupled-physics approach in [18], using [126]. This is the first time that this technique is applied to a problem in elasticity imaging. We treat stability and explicitly characterize the finite-dimensional kernel, and show injectivity in several versions of the linearized inverse problems.

The structure of the paper is as follows: in Section 4.2, we review the elasticity model which we are using, and in Section 4.3, we review necessary background of linear PDE theory. In Section 4.4, we apply this theory to the elasticity equation. This section contains the main results of the paper. We investigate how several kinds of linearizations perform analytically, derive the stability results and the characterization of the kernel. In Section 4.5, we discuss the stability conditions with respect to the literature. The appendix contains topological lemmas needed for the investigation of the kernel.

4.2. Modelling quantitative elastography

4.2.1. Experiments and interior information in elastography

The general principle in elastography [40] is to

- perturb the tissue using a suitable mechanical source
- determine the internal tissue displacement using an ultrasound, magnetic resonance or optical displacement estimation method
- infer the mechanical properties from the interior information, using a mechanical model

Note that in elastography, there are two forms of excitation: an elastic deformation from the mechanical source, and the excitation from the ground modality. Also, the reconstruction procedure involves two steps: the recovery of the mechanical displacement $\mathbf{u}(\mathbf{x})|_{\Omega}$ resp. $\mathbf{u}(\mathbf{x}, t)|_{\Omega}$ from measurements on the boundary, and the recovery of the mechanical parameters and properties from $\mathbf{u}|_{\Omega}$. In this last step of quantitative reconstruction (which is treated in this article), the mechanical displacement $\mathbf{u}|_{\Omega}$ is also referred to as *interior information*.

4.2.2. A linear elasticity model for inhomogeneous linear isotropic media

There exist different variants of elastography using quasi-static, transient or time-harmonic mechanical excitations, but they can be described by common PDE models [40, 106].

The elasticity models can be deduced from the equation of motion [79]

$$\nabla \cdot \sigma - \rho \mathbf{u}_{tt} = \mathbf{F} \quad (4.1)$$

where $\mathbf{F}(\mathbf{x}, t)$ is the excitation force density in N/m^3 . (We use the convention that letters printed in bold denote *vectors* in \mathbb{R}^3 .) The mechanical displacement $\mathbf{u}(\mathbf{x}, t)$ of the material point which is at position \mathbf{x} at time t is measured in $[\mathbf{u}] = \text{m}$. $\rho(\mathbf{x})$ is the density in kg/m^3 . $\sigma = (\sigma_{ij}(\mathbf{x}, t))_{ij}$ is the mechanical (or Cauchy) stress tensor with unit N/m^2 . Here, the divergence of a second-rank tensor A is computed column-wise:

$$\nabla \cdot A = \nabla \cdot (\mathbf{a}_1, \dots, \mathbf{a}_n) := (\nabla \cdot \mathbf{a}_1, \dots, \nabla \cdot \mathbf{a}_n).$$

The constitutive equation in linearized elasticity (also termed Hooke's law) is

$$\sigma = C : \varepsilon \quad (4.2)$$

with the stress tensor $\sigma = \sigma_{ij}(\mathbf{x}, t)$ and the dimensionless strain tensor $\varepsilon = \varepsilon_{kl}(\mathbf{x}, t)$. Here, $:$ denotes the tensor multiplication. The material properties are incorporated into $C = C_{ijkl}(\mathbf{x})$, which is the rank-four stiffness tensor (with unit N/m^2).

Isotropy means that C is reduced to knowledge of two scalar quantities λ and μ , such that one has

$$\sigma = 2\mu\varepsilon + \lambda \text{tr } \varepsilon \mathbf{Id}, \quad (4.3)$$

4. Stability in the linearized problem of quantitative elastography

instead of (4.2). Here, $\lambda(\mathbf{x})$ is called the first Lamé parameter, and $\mu(\mathbf{x})$ is called the shear modulus or the second Lamé parameter. The physical units of λ and μ are the same as of σ and C , i.e. N/m^2 .

In linear elasticity, one works with small deformations, and uses the following representation of the strain ε :

$$\varepsilon = \frac{1}{2}(\nabla \mathbf{u} + \nabla \mathbf{u}^\top). \quad (4.4)$$

Note that with this, the quantity $\text{tr } \varepsilon$ in (4.3) is equal to $\nabla \cdot \mathbf{u}$.

The equation of motion (4.1), with (4.3) and (4.4) is then augmented with boundary conditions and appropriate sources. There are different choices for initial and boundary conditions. One option is

$$\begin{aligned} \nabla(\lambda \nabla \cdot \mathbf{u}) + 2\nabla \cdot (\mu \varepsilon(\mathbf{u})) - \rho \mathbf{u}_{tt} &= \mathbf{F} && \text{on } \Omega \\ \mathbf{u}|_{\partial\Omega} &= 0 \\ \mathbf{u}|_{\Omega \times \{t=0\}} &= \mathbf{g} \\ \partial_t \mathbf{u}|_{\Omega \times \{t=0\}} &= \mathbf{h}. \end{aligned} \quad (4.5)$$

Existence, uniqueness and regularity properties for this model follow from the theory in [86] (for an earlier result for elastodynamic problems, see [38]). The initial and boundary values \mathbf{g} and \mathbf{h} are prescribed only for the complete mathematical analysis. In practical physical experiments, the varying excitations enter in the source term \mathbf{F} .

The standard problem of *quantitative elastography* is then to determine the material parameters $\lambda(\mathbf{x})$, $\mu(\mathbf{x})$ and $\rho(\mathbf{x})$ in the equation (4.5), given the interior information $\mathbf{u}(\mathbf{x}, t)|_\Omega$.

4.2.3. Adapting the quantities in the compressible model

Models based on (4.3) and (4.5) are widely used in elastography for simulating the elastic behavior of tissue [40, 106]. Nevertheless, the parameter which one reconstructs, is often only the shear modulus μ . Sometimes, one assumes the incompressibility condition $\nabla \cdot \mathbf{u} = 0$, or one sets $\lambda \nabla \cdot \mathbf{u} = 0$ [26, 81, 82]. In these cases, λ does not occur in the model at all.

We propose a different definition of quantities for the reconstruction assuming a *compressible* material. Precisely, we change the quantities and use the pressure p defined by

$$p(\mathbf{x}, t) := \lambda(\mathbf{x}) \nabla \cdot \mathbf{u}(\mathbf{x}, t). \quad (4.6)$$

With these quantities, it follows from (4.5) that

$$\nabla p + 2\nabla \cdot (\mu \varepsilon(\mathbf{u})) - \rho \mathbf{u}_{tt} = \mathbf{F}, \quad (4.7)$$

The inverse problem is now to recover $p(\mathbf{x}, t)$, as well as $\mu(\mathbf{x})$ and $\rho(\mathbf{x})$, given $\mathbf{u}(x, t)|_\Omega$. It is this problem which we address in our stability analysis.

4.3. A result from linear PDE theory

Definition (4.6) has been used before, see e.g. [88, 111]). Note that in tissue, one has that $\nabla \cdot \mathbf{u} \ll 1$. Because of ill-posedness of differentiation, the quantity $\nabla \cdot \mathbf{u}$ cannot be computed accurately from the data \mathbf{u} in experiments. On the other hand, one has that $\lambda \gg 1$. In numerical simulations, the pressure p turns out to be of order 1 and therefore should not be neglected [88].

Note that $p(\mathbf{x}, t)$ is an elastic quantity, but not a material parameter: it depends on the particular displacement field induced by the excitation. Knowledge of p may or may not prove to be useful for diagnostic purposes. The reason, though, for introducing this quantity in the inversion model is that it numerically turned out to be useful. It was numerically observed that keeping p in the model improves the reconstruction of the shear modulus μ [88].

In our analysis, we will give a mathematical reason for using (4.7) instead of the first equation in (4.5). Before we come to that, we give the relevant background from PDE theory which we use in our work.

4.3. A result from linear PDE theory

We first treat the background from the general theory of linear PDE systems in \mathbb{R}^n . This will later be applied to $n = 3, n = 4$. The essential information for the quick reader is: We write overdetermined redundant systems of form (4.8) like (4.21). If they satisfy the conditions in Definition 1 and 2, a stability estimate as in Theorem 1 holds.

Let Ω be a bounded domain in \mathbb{R}^n (smoothness requirements on Ω are specified later). We consider the redundant system of linear partial differential equations

$$\begin{aligned} \mathcal{L}(\mathbf{x}, \frac{\partial}{\partial \mathbf{x}}) \mathbf{w} &= \mathcal{S} \quad \text{on } \Omega \\ \mathcal{B}(\mathbf{x}, \frac{\partial}{\partial \mathbf{x}}) \mathbf{w} &= \varphi \quad \text{on } \partial\Omega \end{aligned} \tag{4.8}$$

for m unknown functions $\mathbf{w}(\mathbf{x}) = (w_1(\mathbf{x}), \dots, w_m(\mathbf{x}))$, comprising in total M equations. Here, $\mathcal{L}(\mathbf{x}, \frac{\partial}{\partial \mathbf{x}})$ is a matrix differential operator of dimension $M \times m$,

$$\mathcal{L}(\mathbf{x}, \frac{\partial}{\partial \mathbf{x}}) = \begin{pmatrix} L_{11}(\mathbf{x}, \frac{\partial}{\partial \mathbf{x}}) & \dots & L_{1m}(\mathbf{x}, \frac{\partial}{\partial \mathbf{x}}) \\ \vdots & \ddots & \vdots \\ L_{M1}(\mathbf{x}, \frac{\partial}{\partial \mathbf{x}}) & \dots & L_{Mm}(\mathbf{x}, \frac{\partial}{\partial \mathbf{x}}) \end{pmatrix}. \tag{4.9}$$

For each $1 \leq i \leq M, 1 \leq j \leq m$ and for each point \mathbf{x} , $L_{ij}(\mathbf{x}, \frac{\partial}{\partial \mathbf{x}})$ is a polynomial in $\frac{\partial}{\partial \mathbf{x}} = (\frac{\partial}{\partial x_1}, \dots, \frac{\partial}{\partial x_n})$. Redundancy of the system means that there are possibly more equations than unknowns: $M \geq m$.

Similarly, $\mathcal{B}(\mathbf{x}, \frac{\partial}{\partial \mathbf{x}})$ has entries $B_{kj}(\mathbf{x}, \frac{\partial}{\partial \mathbf{x}})$ for $1 \leq k \leq Q, 1 \leq j \leq m$, consisting of Q equations at the boundary. The operations are again polynomial in the second variable. $\mathcal{S}(\mathbf{x})$ is a vector of length M , and $\varphi(\mathbf{x})$ is a vector of length Q .

4. Stability in the linearized problem of quantitative elastography

We now define the notions of *ellipticity* and the *principal part* of \mathcal{L} and \mathcal{B} , respectively, in the sense of Douglis and Nirenberg [39].

Definition 1. Let integers $s_i, t_j \in \mathbb{Z}$ be given for each row $1 \leq i \leq M$ and column $1 \leq j \leq m$ with the following property: For $s_i + t_j \geq 0$, the order of L_{ij} does not exceed $s_i + t_j$. For $s_i + t_j < 0$, one has $L_{ij} = 0$. Furthermore, the numbers are normalized so that for all i one has $s_i \leq 0$. Such numbers s_i, t_j are called Douglis-Nirenberg numbers.

The principal part of \mathcal{L} for this choice of numbers s_i, t_j is defined as the matrix operator \mathcal{L}_0 whose entries $L_{0,ij}$ are composed of those terms in L_{ij} which are exactly of order $s_i + t_j$.

The principal part \mathcal{B}_0 of \mathcal{B} is composed of the entries $B_{0,kj}$, which are composed of those terms in B_{kj} which are exactly of order $\sigma_k + t_j$. The numbers $\sigma_k, 1 \leq k \leq Q$ are computed as

$$\sigma_k := \max_{1 \leq j \leq m} (b_{kj} - t_j), \quad (4.10)$$

where b_{kj} denotes the order of B_{kj} .

Real directions $\boldsymbol{\xi} \neq 0$ with $\text{rank } \mathcal{L}_0(\mathbf{x}, i\boldsymbol{\xi}) < m$ are called characteristic directions of \mathcal{L} at \mathbf{x} . (The complex unit is denoted by the symbol $i = \sqrt{-1}$.) The operator $\mathcal{L}(\mathbf{x}, \frac{\partial}{\partial \mathbf{x}})$ is said to be overdetermined elliptic in Ω if for all $\mathbf{x} \in \bar{\Omega}$ and for all real vectors $\boldsymbol{\xi} \neq 0$ one has that

$$\text{rank } \mathcal{L}_0(\mathbf{x}, i\boldsymbol{\xi}) = m \quad (4.11)$$

for the $M \times m$ matrix $\mathcal{L}_0(\mathbf{x}, i\boldsymbol{\xi})$.

Douglis-Nirenberg numbers allow that terms of order less than $\max\{\text{ord } L_{ij}\}$ appear in the symbol \mathcal{L}_0 . The maximum number of entries in the symbol is attained if one has that $s_i + t_j = \text{ord } L_{ij}$.

To illustrate in an example, we can consider the system

$$\begin{pmatrix} w_1 & + & \Delta w_2 \\ \frac{\partial}{\partial x_1} w_1 \\ \frac{\partial}{\partial x_2} w_1 \end{pmatrix} = \begin{pmatrix} 0 \\ f \\ g \end{pmatrix}, \quad \begin{pmatrix} w_1|_{\partial\Omega} & \nabla w_2 \cdot \boldsymbol{\nu}|_{\partial\Omega} \end{pmatrix} = \begin{pmatrix} h \\ k \end{pmatrix}, \quad (4.12)$$

where Ω is the unit circle in \mathbb{R}^2 . With $\boldsymbol{\nu}$, we denote the unit normal on $\partial\Omega$.

Here, we have

$$\mathcal{L}(i\boldsymbol{\xi}) = \begin{pmatrix} 1 & -|\boldsymbol{\xi}|^2 \\ i\xi_1 & 0 \\ i\xi_2 & 0 \end{pmatrix}, \quad \mathcal{B}(i\boldsymbol{\xi}) = \begin{pmatrix} 1 & 0 \\ 0 & i\boldsymbol{\xi} \cdot \boldsymbol{\nu} \end{pmatrix}. \quad (4.13)$$

If we choose numbers $(t_j)_{j=1}^2 = (1, 3)$, $(s_i)_{i=1}^3 = (-1, 0, 0)$, we have the principal symbols

$$\mathcal{L}_0(i\boldsymbol{\xi}) = \begin{pmatrix} 1 & -|\boldsymbol{\xi}|^2 \\ i\xi_1 & 0 \\ i\xi_2 & 0 \end{pmatrix}, \quad \mathcal{B}_0(i\boldsymbol{\xi}) = \begin{pmatrix} 1 & 0 \\ 0 & 0 \end{pmatrix} \quad (4.14)$$

4.3. A result from linear PDE theory

and $(\sigma_i)_{i=1}^2 = (-1, -1)$. – If we choose Douglis Nirenberg numbers $(t_j)_{j=1}^2 = (1, 2), (s_i)_{i=1}^3 = (0, 0, 0)$, we have the principal symbols

$$\mathcal{L}_0(\mathbf{i}\boldsymbol{\xi}) = \begin{pmatrix} 0 & -|\boldsymbol{\xi}|^2 \\ \mathbf{i}\xi_1 & 0 \\ \mathbf{i}\xi_2 & 0 \end{pmatrix}, \quad \mathcal{B}_0(\mathbf{i}\boldsymbol{\xi}) = \begin{pmatrix} 1 & 0 \\ 0 & \mathbf{i}\boldsymbol{\xi} \cdot \boldsymbol{\nu} \end{pmatrix} \quad (4.15)$$

and $(\sigma_i)_{i=1}^2 = (-1, -1)$.

Note that the principal symbols differ in this case. Nevertheless, with both choices of numbers, \mathcal{L} is overdetermined elliptic, as there exists a non-vanishing subdeterminant of \mathcal{L}_0 in both cases.

Next we define the condition of \mathcal{B} covering \mathcal{L} , or the *Lopatinskii boundary condition* [126].

Definition 2. Fix $\mathbf{y} \in \partial\Omega$, and let $\boldsymbol{\nu}$ be the inward unit normal vector at \mathbf{y} . Let $\boldsymbol{\zeta}$ be any non-zero tangential vector to Ω at \mathbf{y} . Consider the half-line $\{\mathbf{y} + z\boldsymbol{\nu}, z > 0\}$ and the following system of ordinary differential equations on it:

$$\begin{aligned} \mathcal{L}_0(\mathbf{y}, \mathbf{i}\boldsymbol{\zeta} + \boldsymbol{\nu} \frac{d}{dz}) \tilde{\mathbf{w}}(z) &= 0 & z > 0 \\ \mathcal{B}_0(\mathbf{y}, \mathbf{i}\boldsymbol{\zeta} + \boldsymbol{\nu} \frac{d}{dz}) \tilde{\mathbf{w}}(z) &= 0 & z = 0. \end{aligned} \quad (4.16)$$

Consider the vector space of all solutions $\tilde{\mathbf{w}}$ of (4.16) which satisfy $\tilde{\mathbf{w}}(z) \rightarrow 0$ for $z \rightarrow \infty$. If this vector space consists just of the trivial solution $\tilde{\mathbf{w}}(z) \equiv 0$, then the Lopatinskii condition is said to be fulfilled for the pair $(\mathcal{L}, \mathcal{B})$ at \mathbf{y} , or \mathcal{B} covers the operator \mathcal{L} at \mathbf{y} .

In the example (4.12) above, the equations (4.16), together with the orthogonality condition $\boldsymbol{\nu} \cdot \boldsymbol{\zeta} = 0$, yield

$$\begin{aligned} (-|\boldsymbol{\zeta}|^2 + \frac{d^2}{dz^2}) \tilde{w}_2(z) &= 0 \\ (\mathbf{i}\zeta_1 + \nu_1 \frac{d}{dz}) \tilde{w}_1(z) &= 0 \\ (\mathbf{i}\zeta_2 + \nu_2 \frac{d}{dz}) \tilde{w}_1(z) &= 0. \end{aligned}$$

The last two equations, together with $\boldsymbol{\zeta} \cdot \boldsymbol{\nu} = 0$, imply $\tilde{w}_1(z) = 0$. For $\tilde{w}_2(z)$, there is the solution $\tilde{w}_2(z) = Ce^{-|\boldsymbol{\zeta}|z}$ going to 0 for $z \rightarrow \infty$. – In the case (4.14), there is no requirement to restrain $w_2(z)$, therefore the Lopatinskii boundary condition is not satisfied with this choice of Douglis-Nirenberg numbers. In the other case (4.15), the requirement $\mathcal{B}_0(\mathbf{y}, \mathbf{i}\boldsymbol{\zeta} + \boldsymbol{\nu} \frac{d}{dz}) \tilde{\mathbf{w}}(z) = 0$ leads to $\frac{d}{dz} \tilde{w}_2(z) = -C|\boldsymbol{\zeta}|e^{-|\boldsymbol{\zeta}|z} = 0$, therefore $C = 0$ and consequently $\tilde{w}_2(z) = 0$. Therefore the Lopatinskii boundary condition is satisfied in this case.

A typical example of an overdetermined elliptic systems with Lopatinskii boundary conditions is

$$\begin{aligned} \nabla \times \mathbf{w} &= f \\ \nabla \cdot \mathbf{w} &= g \end{aligned} \quad (4.17)$$

4. Stability in the linearized problem of quantitative elastography

on a domain Ω with normal component $\mathbf{w} \cdot \mathbf{v}|_{\partial\Omega}$ given on the boundary.

In the context of hybrid imaging, examples of overdetermined elliptic systems with Lopatinskii boundary conditions have been considered in [18, 22].

For investigating the stability for linearized quantitative elastography, we are going to use the a-priori estimate in [126] for the solutions of system (4.8). This theory does not need smooth coefficients, but coefficients in the Sobolev spaces $W_p^\alpha(\Omega)$ (for the usual definition, also for noninteger values of α , see [1]). In the setting of [126] with Douglis-Nirenberg numbers t_j, s_i, σ_k , one has that the operator \mathcal{A} with

$$\mathcal{A}\mathbf{w} = \begin{pmatrix} \mathcal{L}\mathbf{w} \\ \mathcal{B}\mathbf{w} \end{pmatrix} \quad (4.18)$$

acts on the space

$$D(p, l) := W_p^{l+t_1}(\Omega) \times \dots \times W_p^{l+t_m}(\Omega), \quad (4.19)$$

where $l \geq 0, p > 1$. Under suitable restrictions on the coefficients L_{ij} and B_{kj} (specified below in the conditions of the theorem), the operator \mathcal{A} is bounded with range in

$$R(p, l) := W_p^{l-s_1}(\Omega) \times \dots \times W_p^{l-s_M}(\Omega) \times W_p^{l-\sigma_1-\frac{1}{p}}(\partial\Omega) \times \dots \times W_p^{l-\sigma_Q-\frac{1}{p}}(\partial\Omega). \quad (4.20)$$

Using the operator \mathcal{A} in (4.18), the equations (4.8) read

$$\mathcal{A}\mathbf{w} = \begin{pmatrix} \mathcal{S} \\ \varphi \end{pmatrix}. \quad (4.21)$$

In formulating the restrictions on the coefficients of \mathcal{L} and \mathcal{B} , we simplify the version of [126, Thm. 1.1] for the following result.

Theorem 1. *Let integers $l \geq 0, p > 1$ be given. Let (\mathcal{S}, φ) , the data from (4.8) be in $R(p, l)$ as defined in (4.20). Let Douglis-Nirenberg numbers s_i and t_j be given for \mathcal{L} in (4.8), and let σ_k be as in Definition 1. Let Ω be a bounded domain with boundary in $C^{l+\max t_j}$. Assume furthermore that $p(l - s_i) > n$ and $p(l - \sigma_k) > n$ for all i and k . Let the coefficients of L_{ij} be in $W_p^{l-s_i}(\Omega)$, and let the coefficients of B_{kj} be in $W^{l-\sigma_k-\frac{1}{p}}(\Omega)$. Then the following statements are equivalent:*

1. \mathcal{L} in (4.8) is overdetermined elliptic (see (4.11)) and the Lopatinskii covering condition (4.16) is fulfilled for $(\mathcal{L}, \mathcal{B})$ on $\partial\Omega$.
2. There exists a left regularizer \mathcal{R} for the operator $\mathcal{A} = \mathcal{L} \times \mathcal{B}$ in (4.18), that is, we have

$$\mathcal{R}\mathcal{A} = \mathcal{I} - \mathcal{T} \quad (4.22)$$

with \mathcal{T} compact from $R(p, l)$ in (4.20) to $D(p, l)$ in (4.19).

3. The following a-priori estimate holds

$$\sum_{j=1}^m \|w_j\|_{W_p^{l+t_j}(\Omega)} \leq C_1 \left(\sum_{i=1}^M \|\mathcal{S}_i\|_{W_p^{l-s_i}(\Omega)} + \sum_{k=1}^Q \|\varphi_k\|_{W_p^{l-\sigma_j-\frac{1}{p}}(\partial\Omega)} \right) + C_2 \sum_{t_j > 0} \|w_j\|_{L^p(\Omega)}, \quad (4.23)$$

where w_j is the j -th component of the solution \mathbf{w} of (4.18)

The assertion of the theorem gives a criterion for the existence of a left regularizer for the overdetermined redundant systems. For the case of boundary value problems for square systems with $M = m$, such an equivalence is established in the classical work of [5]. For square systems, one has the stronger statement that ellipticity and Lopatinskii condition are equivalent to the Fredholm property of a differential operator (which also needs the existence of a right regularizer). – The criterion for redundant systems with $M \geq m$ was established in [126], and investigates the stability estimate, and even gives a representation formula for the solution, provided it exists. The existence of a right regularizer \mathcal{Q} with $\mathcal{A}\mathcal{Q} = \mathcal{I} - \mathcal{T}$ (which would yield local existence) cannot be assured in general for overdetermined systems.

We will exploit this criterion for the linearized version of quantitative elastography.

4.4. Stability analysis

4.4.1. Setting and notation

For treating the hybrid imaging problem described in 4.2.1, we take the adapted forward model with (4.7) in the first equation in (4.5). We recast the equations of the forward problem for the displacement, and the interior information, respectively, into a single system of partial differential equations describing one experiment:

$$\begin{aligned} \nabla p + 2\nabla \cdot (\mu \varepsilon(\mathbf{u})) - \rho \mathbf{u}_{tt} &= \mathbf{F} \\ \mathbf{u}(x, t) &= \mathbf{H} \\ \mathbf{u}|_{\partial\Omega} &= 0 \\ \mathbf{u}|_{\Omega \times \{t=0\}} &= \mathbf{g} \\ \partial_t \mathbf{u}|_{\Omega \times \{t=0\}} &= \mathbf{h} \end{aligned} \quad (4.24)$$

Here, we are given \mathbf{F} (the excitation force), \mathbf{g} and \mathbf{h} , as well as the interior information \mathbf{H} . We formally keep \mathbf{u} and \mathbf{H} distinct in the second equation, as \mathbf{u} is treated as variable of the system, and \mathbf{H} represents the interior information as a separate object. – In this we keep the analogy with the formalism in [18]. We aim at a quantitative estimate such as (4.23) with the given interior information in the inhomogeneity.

We consider the system (4.24), for the variables \mathbf{u} , p , μ , ρ ; therefore, we consider it as nonlinear, involving multiplication of the unknowns. In order to make

4. Stability in the linearized problem of quantitative elastography

it tractable for the analysis, we linearize this system to provide equations of the form (4.8). Several of these linearizations will be considered in the subsequent theory.

We first consider the forward operator

$$\mathcal{V} : (p(\mathbf{x}, t), \mu(\mathbf{x}), \rho(\mathbf{x})) \mapsto \mathbf{u}(\mathbf{x}, t), \quad (4.25)$$

which maps the triple (p, μ, ρ) to the displacement field \mathbf{u} satisfying (4.24). Then we consider the linearization of \mathcal{V} at a reference state (p, μ, ρ) ,

$$\mathcal{V}'(p, \mu, \rho) : \begin{pmatrix} \delta p \\ \delta \mu \\ \delta \rho \end{pmatrix} \mapsto \begin{pmatrix} \delta u_1 \\ \delta u_2 \\ \delta u_3 \end{pmatrix} =: \delta \mathbf{u}.$$

By formal differentiation of (4.24), we find that, at the reference state $\mathbf{u} = \mathcal{V}(p, \mu, \rho)$, the increment $\delta \mathbf{u}$ satisfies the equations

$$\begin{aligned} \nabla \delta p + 2\nabla \cdot (\delta \mu \varepsilon(\mathbf{u})) + 2\nabla \cdot (\mu \varepsilon(\delta \mathbf{u})) - \delta \rho \mathbf{u}_{tt} - \rho(\delta \mathbf{u})_{tt} &= 0 \\ \delta \mathbf{u} &= \delta \mathbf{H} \\ \delta \mathbf{u}|_{\partial \Omega} &= 0 \\ \delta \mathbf{u}|_{\Omega \times \{t=0\}} &= 0 \\ \partial_t \delta \mathbf{u}|_{\Omega \times \{t=0\}} &= 0. \end{aligned} \quad (4.26)$$

Note that \mathbf{F} does not depend on the reference state, therefore no inhomogeneity appears in the first equation in (4.26). The quantity $\delta \mathbf{H}$ is the derivative of the interior information.

Observe that (4.26) is a system of differential equations for the functions $(\delta p, \delta \mu, \delta \rho, \delta u_1, \delta u_2, \delta u_3) = (\delta p, \delta \mu, \delta \rho, \delta \mathbf{u})$. The system is linear in these unknowns.

We now introduce the operator

$$\mathcal{L}_{p\mu\rho}(\delta p, \delta \mu, \delta \rho, \delta \mathbf{u}) := \begin{pmatrix} \nabla \delta p + 2\nabla \cdot (\delta \mu \varepsilon(\mathbf{u})) + 2\nabla \cdot (\mu \varepsilon(\delta \mathbf{u})) - \delta \rho \mathbf{u}_{tt} - \rho(\delta \mathbf{u})_{tt} \\ \delta \mathbf{u} \end{pmatrix}. \quad (4.27)$$

This operator is the linearization of the redundant system (4.24) with respect to p , μ and ρ . Note that $\mathcal{L}_{p\mu\rho}$ is a matrix differential operator like \mathcal{L} in (4.8).

In our analysis, we will treat the operator $\mathcal{L}_{p\mu\rho}$ as well as several specializations, corresponding to the directional derivatives with respect to only *one* parameter; these operators are denoted $\mathcal{L}_p, \mathcal{L}_\mu, \mathcal{L}_\rho$. We also treat the combination $\mathcal{L}_{p\mu}$. These operator specifications are summarized in Table 4.1.

In the model (4.24) which we started from, we incorporated the definition of the pressure in subsection 4.2.3 in (4.6). An alternative is to use the original model (4.5) only, which involved the first Lamé parameter λ . This corresponds to re-substituting $p = \lambda \nabla \cdot \mathbf{u}$ in (4.24). In exact analogy to constructing

4.4. Stability analysis

Operator name	Specification w.r.t. (4.27)	Explicit form
$\mathcal{L}_p(\delta p, \delta \mathbf{u})$	$\mathcal{L}_{p\mu\rho}(\delta p, 0, 0, \delta \mathbf{u})$	$\begin{pmatrix} \nabla \delta p + 2\nabla \cdot (\mu \varepsilon(\delta \mathbf{u})) - \rho(\delta \mathbf{u})_{tt} \\ \delta \mathbf{u} \end{pmatrix}$
$\mathcal{L}_\mu(\delta \mu, \delta \mathbf{u})$	$\mathcal{L}_{p\mu\rho}(0, \delta \mu, 0, \delta \mathbf{u})$	$\begin{pmatrix} 2\nabla \cdot (\delta \mu \varepsilon(\mathbf{u})) + 2\nabla \cdot (\mu \varepsilon(\delta \mathbf{u})) - \rho(\delta \mathbf{u})_{tt} \\ \delta \mathbf{u} \end{pmatrix}$
$\mathcal{L}_\rho(\delta \mu, \delta \mathbf{u})$	$\mathcal{L}_{p\mu\rho}(0, 0, \delta \rho, \delta \mathbf{u})$	$\begin{pmatrix} 2\nabla \cdot (\mu \varepsilon(\delta \mathbf{u})) - \delta \rho \mathbf{u}_{tt} - \rho(\delta \mathbf{u})_{tt} \\ \delta \mathbf{u} \end{pmatrix}$
$\mathcal{L}_{p\mu}(\delta p, \delta \mu, \delta \mathbf{u})$	$\mathcal{L}_{p\mu\rho}(\delta p, \delta \mu, 0, \delta \mathbf{u})$	$\begin{pmatrix} \delta p + 2\nabla \cdot (\delta \mu \varepsilon(\mathbf{u})) + 2\nabla \cdot (\mu \varepsilon(\delta \mathbf{u})) - \rho(\delta \mathbf{u})_{tt} \\ \delta \mathbf{u} \end{pmatrix}$

Table 4.1.: Operators \mathcal{L} used to study systems of kind (4.8) resp. (4.18)

$\mathcal{L}_{p\mu\rho}$ one can form the forward operator \mathcal{V}_λ . One then considers its linearization $\mathcal{V}'_\lambda(\lambda, \mu, \rho) : (\delta \lambda, \delta \mu, \delta \rho) \mapsto \delta \mathbf{u}$, and introduces the operator $\mathcal{L}_{\lambda\mu\rho}$. We particularly will consider

$$\mathcal{L}_\lambda(\delta \lambda, \delta \mathbf{u}) := \mathcal{L}_{\lambda\mu\rho}(\delta \lambda, 0, 0, \delta \mathbf{u}) = \begin{pmatrix} \nabla(\delta \lambda \nabla \cdot \mathbf{u}) + \nabla(\lambda \nabla \cdot \delta \mathbf{u}) + 2\nabla \cdot (\mu \varepsilon(\delta \mathbf{u})) - \rho(\delta \mathbf{u})_{tt} \\ \delta \mathbf{u} \end{pmatrix}, \quad (4.28)$$

which is also contained in Table 4.1.

We want to apply the methodology of Section 4.4.3 to the various linearizations and compare their properties. We keep the formalism consistent with (4.8) resp. (4.21) to study redundant systems of the form:

$$\mathcal{A}\mathbf{w} = \begin{pmatrix} \mathcal{L}\mathbf{w} \\ \mathcal{B}\mathbf{w} \end{pmatrix} = (\mathcal{L} \times \mathcal{B})\mathbf{w} = (\mathcal{S}, 0).$$

In Table 4.1, we already defined several operators \mathcal{L} . What rests is that we have to explain the operators \mathcal{A} and \mathcal{B} , as well as the inhomogeneity \mathcal{S} .

This is very easily done: Looking at (4.26), the boundary data are for each case

$$\mathcal{B}(\delta \mathbf{u}) := \begin{pmatrix} \delta \mathbf{u}|_{\partial\Omega} \\ \delta \mathbf{u}|_{\Omega \times \{t=0\}} \\ \partial_t \delta \mathbf{u}|_{\Omega \times \{t=0\}} \end{pmatrix}, \quad (4.29)$$

For the inhomogeneity \mathcal{S} , we have

$$\mathcal{S} = (0, 0, 0, \delta H_1, \delta H_2, \delta H_3)^\top. \quad (4.30)$$

All of these are linear differential systems which are redundant systems of form (4.8) with $M \geq m$. These are summarized in Table 4.2.

In the elastography literature, linearizations as in Table 4.1 have been treated in iterative algorithms to solve the non-linear problem. See, for example the discussion on the Newton-type algorithms in [40, Sec. 4.1.2], or [101, 130]. In these

4. Stability in the linearized problem of quantitative elastography

Operator name	Explicit form	# eqn. in Ω	# unknowns
\mathcal{A}_p	$\mathcal{L}_p(\delta p, \delta \mathbf{u}) \times \mathcal{B}(\delta \mathbf{u})$	6	4
\mathcal{A}_μ	$\mathcal{L}_p(\delta \mu, \delta \mathbf{u}) \times \mathcal{B}(\delta \mathbf{u})$	6	4
\mathcal{A}_ρ	$\mathcal{L}_p(\delta \rho, \delta \mathbf{u}) \times \mathcal{B}(\delta \mathbf{u})$	6	4
$\mathcal{A}_{p\mu}$	$\mathcal{L}_{p\mu}(\delta p, \delta \mu, \delta \mathbf{u}) \times \mathcal{B}(\delta \mathbf{u})$	6	5
$\mathcal{A}_\mu^{(2)}$	$\mathcal{L}_\mu^{(2)}(\delta \mu, \delta \mathbf{u}_1, \delta \mathbf{u}_2) \times \mathcal{B}(\delta \mathbf{u}_1) \times \mathcal{B}(\delta \mathbf{u}_2)$	12	7
$\mathcal{A}_{p\mu}^{(r)}$	$\mathcal{L}_{p\mu}^{(r)} \times \underbrace{\mathcal{B} \times \dots \times \mathcal{B}}_{r \text{ times}}$	6r	4r+1

Table 4.2.: Summary of the operators used to study the redundant systems (4.8) resp. (4.21); specification of the number of equations in the interior and the number of unknowns; due to space, the arguments of the operator $\mathcal{A}_{p\mu}^{(r)}$ have not been given explicitly

works, the respective linearizations have been computed in their discretized forms, and for only one experiment. Because most applications aim at reconstructing the shear modulus, often only the linearization with respect to μ is employed.

In the literature on hybrid imaging, often multiple measurements are considered. To incorporate the additional information, we can use different excitations \mathbf{F}_i and possibly different functions $\mathbf{g}_i, \mathbf{h}_i$ in (4.24) and obtain different versions of $\mathbf{u}_i(\mathbf{x}, t)$ and interior information $\mathbf{H}_i(\mathbf{x}, t)$. For each experiment, we also have a different variable p_i in the system. While these quantities change with each excitation, the material parameters λ, μ and ρ remain the same.

For example, we write \mathcal{L}_μ^i for the operator corresponding to the reference state \mathbf{u}_i and

$$\mathcal{A}_\mu^{(2)}(\delta \mu, \delta \mathbf{u}_1, \delta \mathbf{u}_2) := \begin{pmatrix} \mathcal{L}_\mu^1(\delta \mu, \delta \mathbf{u}_1) \\ \mathcal{B}(\delta \mathbf{u}_1)|_{\partial\Omega} \\ \mathcal{L}_\mu^2(\delta \mu, \delta \mathbf{u}_2) \\ \mathcal{B}(\delta \mathbf{u}_2)|_{\partial\Omega} \end{pmatrix} = \begin{pmatrix} \mathcal{S}^1 \\ 0 \\ \mathcal{S}^2 \\ 0 \end{pmatrix} \quad (4.31)$$

for the system corresponding to 2 experiments. In the inhomogeneity, we have the quantities $\mathcal{S}^i = (0, 0, 0, \delta \mathbf{H}^i)$ for $i = 1, 2$.

Note that the superscript in brackets denotes the *total* number of experiments, not the single equations for the experiments. Similarly, we also write $\mathcal{L}_\mu^{(2)}(\delta \mu, \delta \mathbf{u}_1, \delta \mathbf{u}_2) = \mathcal{L}_\mu^1(\delta \mu, \delta \mathbf{u}_1) \times \mathcal{L}_\mu^2(\delta \mu, \delta \mathbf{u}_2)$.

Comparison of \mathcal{A}_μ with $\mathcal{A}_\mu^{(2)}$ in Table 4.2 shows the effect of adding one more experiment in the system: there are 6 new equations and 3 new variables: together 12 equations and 7 unknowns.

The shown procedure of adding experiments can be applied to any of the operators \mathcal{A} previously introduced. For each experiment we add, the inequality $M \geq m$ in the formalism of Section 4.3 is fulfilled and the system is redundant. We summarize these operators also in Table 4.2.

4.4. Stability analysis

The reason why we study precisely these operators with several measurements will be apparent from the results in the next Section 4.4.2.

Note that in this section, we have given the general form of the linearization operators for the *dynamic case* on a cylindrical domain $\Omega \times T$. For (quasi-)static elastography, we will consider these operators in the *stationary case* with

$$\mathbf{u}_{tt} = (\delta \mathbf{u})_{tt} = 0, \quad (4.32)$$

using only the spatial domain Ω . This is specially indicated in each case.

4.4.2. Ellipticity

We want to apply the methodology of Section 4.3, and use the criterion in Theorem 1. Therefore, we have to determine the ellipticity condition in Definition 1 for the operators $\mathcal{L}_p, \mathcal{L}_\mu, \mathcal{L}_\rho$ in Table 4.1. We first determine the principal symbol and possible characteristic directions for the operator $\mathcal{L}_{p\mu\rho}$, which is treated in Proposition 1. From this analysis, we then draw some corollaries concerning the ellipticity of $\mathcal{L}_p, \mathcal{L}_\mu, \mathcal{L}_\rho$, as well as ellipticity of $\mathcal{L}_{p\mu}$.

For the analysis of $\mathcal{L}_{p\mu\rho}$, we choose Douglis-Nirenberg numbers $(t_j)_{j=1}^6 = (1, 1, 0, 2, 2, 2)$ and corresponding to the variables $(\delta p, \delta \mu, \delta \rho, \delta u_1, \delta u_2, \delta u_3)$ and numbers $(s_i)_{i=1}^6 = (0, 0, 0, -2, -2, -2)$ corresponding to the six equations. If there are fewer variables in the system (as in $\mathcal{L}_p, \mathcal{L}_\mu, \mathcal{L}_\rho, \mathcal{L}_{p\mu}$), then only the corresponding subset of Douglis-Nirenberg numbers is used (e.g., for the analysis of \mathcal{L}_p , we have the numbers $(1, 2, 2, 2)$ for the variables $(\delta p, \delta u_1, \delta u_2, \delta u_3)$ in \mathcal{L}_p). – We will see below in Proposition 1 that this choice of the numbers $s_i + t_j$ equals exactly the order of L_{ij} ; therefore, it is ensured that we treat the Douglis-Nirenberg symbol \mathcal{L}_0 with the maximum number of entries (see also Definition 1).

Proposition 1. *Let \mathcal{L} be the operator $\mathcal{L}_{p\mu\rho}$ in Table 4.1.*

a) *The principal symbol of $\mathcal{L}_{p\mu\rho}$ (in the dynamic case) is*

$$\mathcal{L}_0((\mathbf{x}, t), i\xi) = \begin{pmatrix} i\xi_1 & 2i\xi_s \cdot \varepsilon(\mathbf{u})_1 & -(u_1)_{tt} & -\mu\xi_1^2 - \mu|\xi|^2 + \rho\xi_4^2 & -\mu\xi_1\xi_2 & -\mu\xi_1\xi_3 \\ i\xi_2 & 2i\xi_s \cdot \varepsilon(\mathbf{u})_2 & -(u_2)_{tt} & -\mu\xi_1\xi_2 & -\mu\xi_2^2 - \mu|\xi|^2 + \rho\xi_4^2 & -\mu\xi_2\xi_3 \\ i\xi_3 & 2i\xi_s \cdot \varepsilon(\mathbf{u})_3 & -(u_3)_{tt} & -\mu\xi_1\xi_3 & -\mu\xi_2\xi_3 & -\mu\xi_3^2 - \mu|\xi|^2 + \rho\xi_4^2 \\ 0 & 0 & 0 & 1 & 0 & 0 \\ 0 & 0 & 0 & 0 & 1 & 0 \\ 0 & 0 & 0 & 0 & 0 & 1 \end{pmatrix}, \quad (4.33)$$

where $\xi_s := (\xi_1, \xi_2, \xi_3)$ for $\xi \in \mathbb{R}^4$.

4. Stability in the linearized problem of quantitative elastography

- b) For every point (\mathbf{x}, t) , the operator $\mathcal{L}_{p\mu\rho}$ is not overdetermined elliptic; also, the operator $\mathcal{L}_{p\mu\rho}^{(r)}$ corresponding to r experiments is not overdetermined elliptic.
- c) In the stationary case (4.32), we have $\mathcal{L}_{p\mu\rho} = \mathcal{L}_{p\mu}$, and the principal symbol is

$$\mathcal{L}_0(\mathbf{x}, i\xi) = \begin{pmatrix} i\xi_1 & 2i\xi \cdot \varepsilon(\mathbf{u})_1 & -\mu\xi_1^2 - \mu|\xi|^2 & -\mu\xi_1\xi_2 & -\mu\xi_1\xi_3 \\ i\xi_2 & 2i\xi \cdot \varepsilon(\mathbf{u})_2 & -\mu\xi_1\xi_2 & -\mu\xi_2^2 - \mu|\xi|^2 & -\mu\xi_2\xi_3 \\ i\xi_3 & 2i\xi \cdot \varepsilon(\mathbf{u})_3 & -\mu\xi_1\xi_3 & -\mu\xi_2\xi_3 & -\mu\xi_3^2 - \mu|\xi|^2 \\ 0 & 0 & 1 & 0 & 0 \\ 0 & 0 & 0 & 1 & 0 \\ 0 & 0 & 0 & 0 & 1 \end{pmatrix} \quad (4.34)$$

for $\xi \in \mathbb{R}^3$.

- d) For every point \mathbf{x} , consider $\mathcal{L} = \mathcal{L}_{p\mu\rho} = \mathcal{L}_{p\mu}$ in the stationary case (4.32). Then \mathcal{L} is not overdetermined elliptic at \mathbf{x} .
- e) For every point \mathbf{x} , consider the operator $\mathcal{L} = \mathcal{L}_{p\mu}^{(r)}$ corresponding to r measurements. Then \mathcal{L} is also not overdetermined elliptic at \mathbf{x} .

Proof. a) To compute the principal symbol (4.33), we refer to the definition of $\mathcal{L}_{p\mu\rho}$ in Table 4.1.

We write the first three equations in $\mathcal{L}_{p\mu\rho}(\delta p, \delta\mu, \delta\rho, \delta\mathbf{u}) = \mathcal{S}$ as

$$\partial_i \delta p + 2 \nabla \cdot (\delta\mu \varepsilon(\mathbf{u})_i) + 2 \nabla \cdot (\mu \varepsilon(\delta\mathbf{u})_i) - \delta\rho(u_i)_{tt} - \rho(\delta u_i)_{tt} = 0, \quad i = 1, 2, 3 \quad (4.35)$$

where we denote the columns of the (symmetric) strain as

$$\varepsilon(\mathbf{u}) = \frac{1}{2}(\nabla \mathbf{u} + \nabla \mathbf{u}^\top) = (\varepsilon(\mathbf{u})_1, \varepsilon(\mathbf{u})_2, \varepsilon(\mathbf{u})_3).$$

The meaning of $\varepsilon(\delta\mathbf{u})_i$ is analogous.

The last three equations in $\mathcal{L}_{p\mu\rho}(\delta p, \delta\mu, \delta\rho, \delta\mathbf{u}) = \mathcal{S}$ are written as

$$\delta u_i = \delta H_i \quad i = 1, 2, 3 \quad (4.36)$$

We now want to determine the entries $L_{0,ij}$ of the principal symbol $\mathcal{L}_0((\mathbf{x}, t), i\xi)$. Note that each of the columns in \mathcal{L}_0 exactly corresponds to one of the variables $(\delta p, \delta\mu, \delta\rho, \delta u_1, \delta u_2, \delta u_3)$. Starting with $j = 1$, we go through the variable list until $j = 6$. For each variable, we determine the term where the unknown appears in the equations (4.35) resp. in (4.36). Then we choose that component of the term which has order $t_j + s_i$. Substituting $i\xi$ for $\frac{\partial}{\partial(\mathbf{x}, t)}$ in that component gives the corresponding entries $(L_{0,ij})_{i=1}^6$ in the j -th column of \mathcal{L}_0 .

4.4. Stability analysis

For the first column corresponding to δp , the term $\partial_i \delta p$ in (4.35) is translated to $(i\xi_1, i\xi_2, i\xi_3)$ in $(L_{0,i1})_{i=1}^3$. The second column corresponding to $\delta\mu$, and the summand of highest order in the term $2 \nabla \cdot (\delta\mu \varepsilon(\mathbf{u})_i)$ translates to $2 \xi_s \cdot \varepsilon(\mathbf{u})_i$ in $(L_{0,i2})_{i=1}^3$ with $\xi_s = (\xi_1, \xi_2, \xi_3)$. In the third column corresponding to $\delta\rho$, no differentiation occurs, so we just have $-(u_i)_{tt}$ as entries in $(L_{0,i3})_{i=1}^3$.

The last three columns correspond to the variables $(\delta u_1, \delta u_2, \delta u_3)$. The relevant terms in (4.35) are

$$2 \nabla \cdot (\mu \varepsilon(\delta \mathbf{u})_i) - \rho(\delta u_i)_{tt} = \nabla \cdot \left(\mu \begin{pmatrix} \partial_1 \delta u_i \\ \partial_2 \delta u_i \\ \partial_3 \delta u_i \end{pmatrix} \right) + \nabla \cdot \left(\mu \begin{pmatrix} \partial_i \delta u_1 \\ \partial_i \delta u_2 \\ \partial_i \delta u_3 \end{pmatrix} \right) - \rho(\delta u_i)_{tt}. \quad (4.37)$$

We substitute $i\xi$ for differentiation in (4.37) and take the terms of highest order to find the entries of the columns $(L_0)_{i,j}$, $j = 4, 5, 6$; these are the terms $-\mu\xi_i^2 - \mu|\xi|^2 + \rho\xi_4^2$ in $(L_0)_{i,i+3}$, $i = 1, 2, 3$, and the term $-\mu\xi_i\xi_j$ in the entries $(L_0)_{i,j}$, $j = 4, 5, 6$, $j \neq i$. The last three equations (4.36) contain no derivatives and give rise to the identity matrix in the entries $(L_0)_{ij}$, $4 \leq i, j \leq 6$ of the principal symbol.

c) The calculations for the symbol (4.34) in the stationary case are exactly the same as for the dynamic case. The only change in this case is that there is no temporal derivative. Therefore there is no variable $\delta\rho$, and one column less than in (4.33), and ξ_4 can be set to zero everywhere.

b) In $\mathcal{L}_{p\mu\rho}$, we have the characteristic direction $\xi = (0, 0, 0, \xi_4)$, $\xi_4 \neq 0$. The same is true of $\mathcal{L}_{p\mu\rho}^{(r)}$.

d) We first observe that in (4.34), three of the columns are clearly linearly independent. The first two columns, though, can be linearly dependent:

Consider the symmetric strain $\varepsilon = \varepsilon^\top$. As the entries are real, there always exists an eigenvector \mathbf{v} such that

$$\varepsilon * \mathbf{v} = \left(\varepsilon_1 \cdot \mathbf{v}, \varepsilon_2 \cdot \mathbf{v}, \varepsilon_3 \cdot \mathbf{v} \right) = \kappa \mathbf{v}, \quad (4.38)$$

where $*$ denotes matrix multiplication. Choosing $(\xi_1, \xi_2, \xi_3) = \mathbf{v}$ gives linear dependence of $\mathcal{L}_0(i\xi)$ in the first two columns.

In conclusion, at each point (\mathbf{x}, t) resp. \mathbf{x} , there are choices of ξ such that the symbols in (4.34) do not have full rank. Therefore $\mathcal{L}_{p\mu}$ is not overdetermined elliptic.

e) Let $\mathcal{L} = \mathcal{L}_{p\mu}^{(r)}$ be the operator corresponding to r measurements $(\mathbf{u}^1, \dots, \mathbf{u}^r)$. Organising the unknowns in the order $(\delta\mu, \delta p_1, \delta \mathbf{u}_1, \dots, \delta p_r, \delta \mathbf{u}_r)$, we get the fol-

4. Stability in the linearized problem of quantitative elastography

lowing $6r \times 4r + 1$ matrix as symbol:

$$\mathcal{L}_0(\mathbf{x}, \mathbf{i}\boldsymbol{\xi}) = \begin{pmatrix} \boxed{2i\varepsilon(\mathbf{u}_1) * \boldsymbol{\xi}} & \boxed{i\boldsymbol{\xi}} & 0 & 0 & 0 & \dots & 0 & 0 \\ 0 & 0 & \boxed{\mathbf{Id}_{3 \times 3}} & 0 & 0 & \dots & 0 & 0 \\ \boxed{2i\varepsilon(\mathbf{u}_2) * \boldsymbol{\xi}} & 0 & 0 & \boxed{i\boldsymbol{\xi}} & 0 & \dots & 0 & 0 \\ 0 & 0 & 0 & 0 & \boxed{\mathbf{Id}_{3 \times 3}} & \dots & 0 & 0 \\ \vdots & \vdots & \vdots & \vdots & \vdots & \ddots & \vdots & \vdots \\ \boxed{2i\varepsilon(\mathbf{u}_r) * \boldsymbol{\xi}} & 0 & 0 & 0 & 0 & \dots & \boxed{i\boldsymbol{\xi}} & 0 \\ 0 & 0 & 0 & 0 & 0 & \dots & 0 & \boxed{\mathbf{Id}_{3 \times 3}} \end{pmatrix}. \quad (4.39)$$

Note that each experiment contributes 6 rows to \mathcal{L}_0 . – Ellipticity of \mathcal{L} is equivalent to the $4r + 1$ columns being linearly independent.

First, the blocks with $\mathbf{Id}_{3 \times 3}$ in the matrix immediately yield that $3r$ columns of the matrix are a linearly independent set. Also, these columns are independent of the remaining $r + 1$ columns corresponding to $(\delta\mu, \delta p_1, \dots, \delta p_r)$.

To investigate the ellipticity of $\mathcal{L}_{p\mu}^{(r)}$, we therefore build sub-matrices $\mathcal{D} = \mathcal{D}(\mathbf{x}, \mathbf{i}\boldsymbol{\xi})$ of size $r + 1 \times r + 1$ in the following way: We take the indexes of those remaining $r + 1$ columns and make any choice \mathbf{C} of $r + 1$ row indexes. Then we analyze whether the rank of such submatrices \mathcal{D} can be maximal.

Case 1: In the index choice \mathbf{C} , there are 3 consecutive entries $(6(j_0 - 1) + k)_{j=1,2,3}$, corresponding to one single experiment j_0 . Taking $\boldsymbol{\xi}$ an eigenvector of $\varepsilon(\mathbf{u}_{j_0})$ yields linear dependence of the columns 1 and $j_0 + 1$ in $\mathcal{D}(\mathbf{x}, \mathbf{i}\boldsymbol{\xi})$.

Case 2: There exists an experiment j_0 not represented in \mathbf{C} . In this case, the column $j_0 + 1$ of \mathcal{D} is degenerate.

Case 3: Of each experiment, there is one row in our choice \mathbf{C} , and from one experiment, there are two rows in \mathbf{C} . Without loss of generality, assume that it is the last experiment of which two rows have been chosen. Then we have that $\mathbf{C} = (k_1, 6 + k_2, \dots, 6(r - 1) + k_r, 6(r - 1) + l), (k_1, \dots, k_r, l) \in \{1, 2, 3\}, l \neq k_r$. In this case, the resulting submatrix $\mathcal{D} = \mathcal{D}_r$ is

$$\mathcal{D}_r(\mathbf{x}, \mathbf{i}\boldsymbol{\xi}) = \begin{pmatrix} 2i\varepsilon(\mathbf{u}_1)_{k_1} \cdot \boldsymbol{\xi} & i\xi_{k_1} & 0 & \dots & 0 \\ 2i\varepsilon(\mathbf{u}_2)_{k_2} \cdot \boldsymbol{\xi} & 0 & i\xi_{k_2} & \dots & 0 \\ \vdots & \vdots & \vdots & \ddots & \vdots \\ 2i\varepsilon(\mathbf{u}_r)_{k_r} \cdot \boldsymbol{\xi} & 0 & 0 & \dots & i\xi_{k_r} \\ 2i\varepsilon(\mathbf{u}_r)_l \cdot \boldsymbol{\xi} & 0 & 0 & \dots & i\xi_l \end{pmatrix}. \quad (4.40)$$

We now take an eigenvector $\boldsymbol{\xi} \neq 0$ of $\varepsilon(\mathbf{u}_r)$ and claim that the matrix $\mathcal{D}_r(\mathbf{x}, \mathbf{i}\boldsymbol{\xi})$ does not have full rank.

Inductively, we begin with $r = 1$. With κ being the corresponding eigenvalue, we have that $\mathcal{D}_1 = \begin{pmatrix} 2i\varepsilon(\mathbf{u}_1)_{k_1} \cdot \boldsymbol{\xi} & i\xi_{k_1} \\ 2i\varepsilon(\mathbf{u}_1)_l \cdot \boldsymbol{\xi} & i\xi_l \end{pmatrix} = \begin{pmatrix} 2i\kappa\xi_{k_1} & i\xi_{k_1} \\ 2i\kappa\xi_l & i\xi_l \end{pmatrix}$ is rank-deficient.

Now let $\det \mathcal{D}_{r-1}(\mathbf{x}, \mathbf{i}\boldsymbol{\xi}) = 0$ for $r - 1$. Choosing an experiment $j_0 \neq r$, and evaluating the Laplace expansion of the determinant of (4.40) along the column

$j_0 + 1$, the only nontrivial cofactor resulting equals $i\xi_{k_{j_0}} \cdot \det \mathcal{D}_{r-1}$ (where \mathcal{D}_{r-1} is the matrix corresponding to experiments $(\mathbf{u}_1, \dots, \mathbf{u}_{j_0-1}, \mathbf{u}_{j_0+1}, \dots, \mathbf{u}_r)$). But the induction assumption tells us that this expression vanishes. Therefore, with our choice of ξ , the matrix $\mathcal{D}_r(\mathbf{x}, i\xi)$ has a rank-deficiency for any $r \geq 1$.

The cases **1-3** exhaust all possibilities of forming the relevant sub-matrices \mathcal{D} of \mathcal{L}_0 . In the proof, we have seen that neither of them has full rank. Therefore, $\mathcal{L} = \mathcal{L}_{p\mu}^{(r)}$ is not over-determined elliptic. \square

We now restrict the focus on linearizations in only one direction, which were introduced in Section 4.4.1. Then the corresponding principal symbol contains fewer columns and results on ellipticity can be obtained.

Corollary 1. *The operator \mathcal{L}_p in Table 4.1, considered in the stationary case, is elliptic everywhere.*

Proof. Let $\mathcal{L} = \mathcal{L}_p$. The principal symbol consists of the first and the three last columns of the matrix in (4.34):

$$\mathcal{L}_0(\mathbf{x}, i\xi) = \begin{pmatrix} i\xi_1 & & & \\ i\xi_2 & & * & \\ i\xi_3 & & & \\ & \mathbf{Id}_{3 \times 3} & & \end{pmatrix}. \quad (4.41)$$

For $\xi \neq 0$, this symbol has maximal rank 4 everywhere, therefore \mathcal{L}_p is elliptic. \square

Corollary 2. *The operator \mathcal{L}_μ in Table 4.1, considered in the stationary case, is elliptic exactly at points which satisfy*

$$\det(\varepsilon(\mathbf{u}(\mathbf{x}, t))) \neq 0. \quad (4.42)$$

The operator $\mathcal{L}_\mu^{(r)}$, corresponding to r measurements $(\delta \mathbf{u})_k, 1 \leq k \leq r$, is elliptic exactly at points where at least one of $\det(\varepsilon(\mathbf{u}_k(\mathbf{x}, t))) \neq 0$.

Proof. Let $\mathcal{L} = \mathcal{L}_\mu$ (the case of one measurement). Then the principal symbol consists of the second and the three last columns of the matrix in (4.34):

$$\mathcal{L}_0(\mathbf{x}, i\xi) = \begin{pmatrix} i\xi_s \cdot \varepsilon(\mathbf{u})_1 & & & \\ i\xi_s \cdot \varepsilon(\mathbf{u})_2 & & * & \\ i\xi_s \cdot \varepsilon(\mathbf{u})_3 & & & \\ & \mathbf{Id}_{3 \times 3} & & \end{pmatrix} \quad (4.43)$$

This symbol has rank 4 provided that the first column is non-degenerate, which is equivalent to the condition (4.42) of non-singular strain.

Now let $\mathcal{L} = \mathcal{L}_\mu^{(r)}$ (the case of multiple measurements). This can be treated by induction on r . Let the principal symbol $\mathcal{L}_0^{(r-1)}$ corresponding to $r - 1$ measurements have dimension $a \times b$. Adding one measurement means adding three

4. Stability in the linearized problem of quantitative elastography

more columns (and six new lines) in the matrix, such that it has dimension $(a + 6) \times (b + 3)$. These three new columns are independent because of the identity component in $(L_{0,ij})$, $a + 4 \leq i \leq a + 6$, $b + 1 \leq j \leq b + 3$.

In the first column of $\mathcal{L}_0^{(r)}$, there are three new entries $(2i\xi_r \cdot \varepsilon(\mathbf{u}_r)_i)_{i=1}^3$ at position $(L_{0,i1})_{i=3r-2}^{3r}$. If we have that for $1 \leq k \leq r$, at least one of $\det(\varepsilon(\mathbf{u}_k(\mathbf{x}, t))) \neq 0$ is non-zero, then the principal symbol $\mathcal{L}_0^{(r)}$ has full rank: in the case $k < r$ because of the induction assumption, and in the case $k = r$ because of non-degeneracy in the first column due to the new measurement. \square

Corollary 3. *The operator \mathcal{L}_ρ in Table 4.1 is elliptic exactly at points with $\mathbf{u}_{tt} \neq 0$. For the case of several measurements, $\mathcal{L}_\rho^{(r)}$ is elliptic exactly at points (\mathbf{x}, t) where at least one of $(\mathbf{u}_k)_{tt}(\mathbf{x}, t) \neq 0$, $1 \leq k \leq r$.*

Proof. Let $\mathcal{L} = \mathcal{L}_\rho$. The principal symbol consists of the last four columns of the matrix in (4.33):

$$\mathcal{L}_0((\mathbf{x}, t), i\xi) = \begin{pmatrix} -(u_1)_{tt} & & & \\ -(u_2)_{tt} & & * & \\ -(u_3)_{tt} & & & \\ & \mathbf{Id}_{3 \times 3} & & \end{pmatrix} \quad (4.44)$$

This symbol has rank 4 iff \mathbf{u}_{tt} is nonzero. The statement for multiple measurements is proved by induction, analogous to the case of $\mathcal{L}_\mu^{(r)}$. \square

Remark 1. As starting point of our analysis, we have chosen the modified model (4.7) with the substitution $p = \lambda \nabla \cdot \mathbf{u}$ in (4.6). Of course, we could also analyze the system corresponding to the original model (4.5). Using linearization in direction of $\delta\lambda$, we have the operator \mathcal{L}_λ in (4.28).

Now let $\mathcal{L} = \mathcal{L}_\lambda$ in the stationary case. Doing calculations as in Proposition 1, and restricting the focus on the first and last three columns as in Corollary 1, one finds the resulting principal symbol as

$$\mathcal{L}_0(\mathbf{x}, i\xi) = \begin{pmatrix} i\xi_1 \nabla \cdot \mathbf{u} & & & \\ i\xi_2 \nabla \cdot \mathbf{u} & & * & \\ i\xi_3 \nabla \cdot \mathbf{u} & & & \\ & \mathbf{Id}_{3 \times 3} & & \end{pmatrix}. \quad (4.45)$$

But in experiments, it is most likely that there exist points \mathbf{x} with $\nabla \cdot \mathbf{u}(\mathbf{x}) = 0$ (in fact, tissue is often approximately assumed to fulfil $\nabla \cdot \mathbf{u}|_\Omega = 0$ on the whole domain). At such points \mathbf{x} , a characteristic direction of \mathcal{L}_λ occurs, therefore consideration of the elliptic operator \mathcal{L}_p seems preferable (see also the discussion in Section 4.5).

Remark 2. Corollary 2 gives the criterion (4.42) for the reference state (which will be used later in Theorem 2). This criterion means that at each point, at least one of the measured elastic displacement fields has *non-singular strain*. The requirement of such qualitative conditions for the solutions is typical for the

coupled-physics literature.

In fact, the condition (4.42) for $r = 2$ is a generalization of the invertibility condition for the nonlinear reconstruction problem in elastography, which was found in the research of [20], namely

$$\det(t_2\varepsilon(\mathbf{u}_1) - t_1\varepsilon(\mathbf{u}_2)) \neq 0. \quad (4.46)$$

Here, we have for $k = 1, 2$ that $t_k := \text{tr}(\varepsilon(\mathbf{u}_k)) = \nabla \cdot \mathbf{u}_k$. It can be verified by simple calculation that violation of (4.42) leads to violation of (4.46).

It is unknown whether (4.46) can be ensured with two vector fields for every distribution of material parameters. For several parameter classes, existence of boundary conditions ensuring (4.46) can be justified, see the discussion and examples in [20, Sec.3.3]. As (4.67) is a consequence of (4.46), the special argumentation for (4.46) can also be invoked for arguing for the premise of Corollary 2 (and later Theorem 2) in our case.

4.4.3. Lopatinskii condition

We want to use the stability criterion in Theorem 1 for the systems \mathcal{A}_p , \mathcal{A}_μ and \mathcal{A}_ρ in Table 4.2. For this purpose, we are checking the covering condition in Definition 2 for the various differential operators \mathcal{L} introduced in Section 4.4.1, together with the relevant boundary data where necessary.

Proposition 2. *The systems \mathcal{L}_p and \mathcal{L}_μ in Table 4.1 satisfy the Lopatinskii condition with arbitrary boundary data.*

Proof. For checking the Lopatinskii (or covering) condition in Definition 2, we have to consider the vector space of functions satisfying the system (4.16) and show that it is trivial.

Let $\mathcal{L} = \mathcal{L}_p$ with principal symbol (4.41), and let \mathbf{y} be a point on the boundary. Then the system of equations $\mathcal{L}_0(\mathbf{y}, i\zeta + \nu \frac{d}{dz})\tilde{\mathbf{w}}(z) = 0$ in (4.16) comprises 6 equations for 4 unknowns $(\tilde{w}_1(z), \tilde{w}_2(z), \tilde{w}_3(z), \tilde{w}_4(z))$.

In the entries $(L_0)_{ij}$, $4 \leq i \leq 6$, $2 \leq j \leq 4$ of (4.41), there is a 3-by-3 identity matrix. The three last equations of (4.16) therefore mean that

$$\tilde{w}_2(z) = \tilde{w}_3(z) = \tilde{w}_4(z) = 0. \quad (4.47)$$

The first three equations in (4.16) then reduce to

$$(i\zeta_k + \nu_k \frac{d}{dz})\tilde{w}_1(z) = 0, \quad k = 1, 2, 3. \quad (4.48)$$

Any functions which are in the vector space considered in Definition 2 have to satisfy (4.48).

The only possible solutions of (4.48) consist of functions of form $e^{i\lambda z}$, where the parameter $\lambda = \frac{\zeta_i}{\nu_i}$ is a real number; neither of these functions tends to 0 for $z \rightarrow \infty$. In this argument, we did not use any boundary constraint. Therefore

4. Stability in the linearized problem of quantitative elastography

the vector space to be considered in Definition 2 is trivial for every $\mathbf{y} \in \partial\Omega$, and the Lopatinskii covering condition is always satisfied.

Now let $\mathcal{L} = \mathcal{L}_\mu$ with principal symbol (4.43). Then, for \mathbf{y} on the boundary, consider the system $\mathcal{L}_0(\mathbf{y}, i\boldsymbol{\zeta} + \boldsymbol{\nu} \frac{d}{dz})\tilde{\mathbf{w}}(z) = 0$ in (4.16). Similarly to (4.47), the last three components vanish, and the system reduces to

$$\mathbf{g}_j \cdot (i\boldsymbol{\zeta}_s + \boldsymbol{\nu} \frac{d}{dz})\tilde{w}_1(z) = 0. \quad j = 1, 2, 3. \quad (4.49)$$

Here, we use fixed vectors $\mathbf{g}_j = \varepsilon(\mathbf{u}(\mathbf{y}))_j, j = 1, 2, 3$ and $\boldsymbol{\zeta}_s = (\zeta_1, \zeta_2, \zeta_3)$.

Suppose that the relation $\mathbf{g}_j \cdot \boldsymbol{\nu} \neq 0$ holds for all j . Then we have solutions of (4.49) of form $e^{i \frac{\mathbf{g}_i \cdot \boldsymbol{\zeta}_s}{\mathbf{g}_i \cdot \boldsymbol{\nu}} z}$. The numbers $\frac{\mathbf{g}_i \cdot \boldsymbol{\zeta}_s}{\mathbf{g}_i \cdot \boldsymbol{\nu}}$ are real, so neither of these functions tends to 0.

Suppose, on the other hand, that we have $\mathbf{g}_{j_0} \cdot \boldsymbol{\nu} = 0$ for one j_0 . Then, using $\boldsymbol{\nu} \cdot \boldsymbol{\zeta}_s = 0$, we have $\mathbf{g}_{j_0} \cdot \boldsymbol{\zeta}_s \neq 0$. Inserting this information in (4.49), we directly get $\tilde{w}_1(z) = 0$.

Therefore the Lopatinskii condition for \mathcal{L}_μ is satisfied with arbitrary boundary data. \square

Proposition 3. *The system \mathcal{L}_ρ in Table 4.1 satisfies the Lopatinskii condition with arbitrary boundary data if and only if $\mathbf{u}(\mathbf{y}, t)_{tt} \neq 0$ for all $(\mathbf{y}, t) \in \partial(\Omega \times T)$.*

Proof. Consider the system $\mathcal{L}_0(\mathbf{y}, i\boldsymbol{\zeta} + \boldsymbol{\nu} \frac{d}{dz})\tilde{\mathbf{w}}(z) = 0$ in (4.16) for the operator \mathcal{L}_ρ . As in the proof of Proposition 2, we get

$$\tilde{w}_2(z) = \tilde{w}_3(z) = \tilde{w}_4(z) = 0.$$

The equations for $\tilde{w}_1(z)$ therefore reduce to

$$(u_i)_{tt}\tilde{w}_1(z) = 0 \quad \text{for } i = 1, 2, 3 \quad (4.50)$$

If we suppose $\mathbf{u}(\mathbf{y}, t)_{tt} \neq 0$, then (4.50) implies $\tilde{w}_1(z) = 0$, therefore the Lopatinskii condition is satisfied.

Conversely, suppose that $\mathbf{u}(\mathbf{y}, t)_{tt} = 0$ for one (\mathbf{y}, t) . Then one can choose $\tilde{\mathbf{w}}(z) = (w_1(z), 0, 0, 0)$ satisfying (4.50) for any function w_1 that satisfies $w_1(z) \rightarrow 0$. Therefore the Lopatinskii condition would be violated. \square

For the study of $\mathcal{L}_{p\mu}$, we need the following boundary operator

$$\mathcal{B}'(\delta\mathbf{u}) = \begin{pmatrix} \delta\mathbf{u}|_{\partial\Omega} \\ \delta\mathbf{u}|_{\Omega \times \{t=0\}} \\ \partial_t \delta\mathbf{u}|_{\Omega \times \{t=0\}} \\ \delta p|_{\partial\Omega} \\ \delta\mu|_{\partial\Omega} \end{pmatrix} = 0, \quad (4.51)$$

incorporating additional constraints on δp and $\delta\mu$.

4.4. Stability analysis

Proposition 4. *The system $\mathcal{L}_{p\mu}$ in Table 4.1 satisfies the Lopatinskii condition with boundary data (4.51) at $\mathbf{y} \in \partial\Omega$, provided that the unit normal vector $\boldsymbol{\nu}(\mathbf{y})$ is not an eigenvector of $\varepsilon(\mathbf{u}(\mathbf{y}))$.*

Proof. Let $\mathcal{L} = \mathcal{L}_{p\mu}$. The principal symbol \mathcal{L}_0 consists of the two first and the three last columns of the matrix in (4.33). Consider then the system of equations

$$\mathcal{L}_0(\mathbf{y}, i\zeta + \boldsymbol{\nu} \frac{d}{dz}) \tilde{\mathbf{w}}(z) = 0$$

from (4.16) for the vector $\tilde{\mathbf{w}}(z) = (\tilde{w}_1(z), \dots, \tilde{w}_5(z))$. The last three equations of this system yield that $\tilde{w}_3(z) = \tilde{w}_4(z) = \tilde{w}_5(z) = 0$, similar to (4.47). For the two remaining functions $\tilde{w}_1(z)$ and $\tilde{w}_2(z)$, the equations reduce to

$$(i\zeta_j + \nu_j \frac{d}{dz}) \tilde{w}_1(z) + \mathbf{g}_j \cdot (i\zeta_s + \boldsymbol{\nu} \frac{d}{dz}) \tilde{w}_2(z) = 0, \quad j = 1, 2, 3. \quad (4.52)$$

Here, $\zeta_s = (\zeta_1, \zeta_2, \zeta_3)$ and we use the fixed vectors

$$\mathbf{g}_j = \varepsilon(\mathbf{u}(\mathbf{y}))_j, \quad j = 1, 2, 3. \quad (4.53)$$

Now let us assume that there exist non-zero solutions to this system. By elimination of $\tilde{w}_2(z)$ and $\frac{d}{dz} \tilde{w}_2(z)$ from (4.52) with $j = 1, 2, j = 1, 3, j = 2, 3$, respectively, we find the following three equations which $\tilde{w}_1(z)$ has to satisfy:

$$a_{1,2} \frac{d^2}{dz^2} \tilde{w}_1(z) + b_{1,2} \frac{d}{dz} \tilde{w}_1(z) + c_{1,2} \tilde{w}_1(z) = 0 \quad (4.54)$$

$$a_{1,3} \frac{d^2}{dz^2} \tilde{w}_1(z) + b_{1,3} \frac{d}{dz} \tilde{w}_1(z) + c_{1,3} \tilde{w}_1(z) = 0 \quad (4.55)$$

$$a_{2,3} \frac{d^2}{dz^2} \tilde{w}_1(z) + b_{2,3} \frac{d}{dz} \tilde{w}_1(z) + c_{2,3} \tilde{w}_1(z) = 0, \quad (4.56)$$

with the coefficients

$$a_{p,q} = \nu_p \mathbf{g}_q \cdot \boldsymbol{\nu} - \nu_q \mathbf{g}_p \cdot \boldsymbol{\nu} \quad (4.57)$$

$$b_{p,q} = i(\zeta_p \mathbf{g}_q \cdot \boldsymbol{\nu} + \nu_p \mathbf{g}_q \cdot \zeta_s - \zeta_q \mathbf{g}_p \cdot \boldsymbol{\nu} - \nu_q \mathbf{g}_p \cdot \zeta_s) \quad (4.58)$$

$$c_{p,q} = \zeta_q \mathbf{g}_p \cdot \zeta_s - \zeta_p \mathbf{g}_q \cdot \zeta_s. \quad (4.59)$$

The same equations are obtained for $\tilde{w}_2(z)$ also, by elimination of $\tilde{w}_1(z)$ from (4.52) with $j = 1, 2, j = 1, 3, j = 2, 3$, respectively.

Let us consider the matrix of the coefficients in (4.54)-(4.56),

$$A = \begin{pmatrix} a_{1,2} & b_{1,2} & c_{1,2} \\ a_{1,3} & b_{1,3} & c_{1,3} \\ a_{2,3} & b_{2,3} & c_{2,3} \end{pmatrix}. \quad (4.60)$$

We claim that under our assumption, the system (4.54)-(4.56) is nontrivial, which is equivalent to $A \neq 0$.

4. Stability in the linearized problem of quantitative elastography

Assume, on the contrary, that all entries in A vanish:

$$A = 0. \quad (4.61)$$

Incorporating the information (4.57)-(4.59), the nine equations in (4.61) can be written in matrix form as

$$\begin{pmatrix} 0 & 0 & 0 & -\nu_2 & \nu_1 & 0 \\ 0 & 0 & 0 & -\nu_3 & 0 & \nu_1 \\ 0 & 0 & 0 & 0 & -\nu_3 & \nu_2 \\ -\nu_2 & \nu_1 & 0 & -\zeta_2 & \zeta_1 & 0 \\ -\nu_3 & 0 & \nu_1 & -\zeta_3 & 0 & \zeta_1 \\ 0 & -\nu_3 & \nu_2 & 0 & -\zeta_3 & \zeta_2 \\ \zeta_2 & -\zeta_1 & 0 & 0 & 0 & 0 \\ \zeta_3 & 0 & -\zeta_1 & 0 & 0 & 0 \\ 0 & \zeta_3 & -\zeta_2 & 0 & 0 & 0 \end{pmatrix} * \begin{pmatrix} \mathbf{g}_1 \cdot \boldsymbol{\zeta}_s \\ \mathbf{g}_2 \cdot \boldsymbol{\zeta}_s \\ \mathbf{g}_3 \cdot \boldsymbol{\zeta}_s \\ \mathbf{g}_1 \cdot \boldsymbol{\nu} \\ \mathbf{g}_2 \cdot \boldsymbol{\nu} \\ \mathbf{g}_3 \cdot \boldsymbol{\nu} \end{pmatrix} = 0 \quad (4.62)$$

Here, $*$ denotes matrix multiplication.

The system (4.62) can be seen as linear system of equations for the unknown variables $\{\mathbf{g}_1 \cdot \boldsymbol{\zeta}_s, \mathbf{g}_2 \cdot \boldsymbol{\zeta}_s, \mathbf{g}_3 \cdot \boldsymbol{\zeta}_s, \mathbf{g}_1 \cdot \boldsymbol{\nu}, \mathbf{g}_2 \cdot \boldsymbol{\nu}, \mathbf{g}_3 \cdot \boldsymbol{\nu}\}$. The system can then be solved by elimination. The one dimensional solution space is generated by the vector $(\zeta_1, \zeta_2, \zeta_3, \nu_1, \nu_2, \nu_3)$. In particular, we have

$$\mathbf{g}_j \cdot \boldsymbol{\nu} = \kappa \nu_j \quad \text{for } j = 1, 2, 3.$$

Using the definition of \mathbf{g}_j in (4.53), it follows that

$$\varepsilon(\mathbf{u}(\mathbf{y})) * \boldsymbol{\nu}(\mathbf{y}) = \kappa \boldsymbol{\nu}(\mathbf{y}), \quad (4.63)$$

as we have that $\varepsilon = \varepsilon^\top$. But, by assumption, $\boldsymbol{\nu}(\mathbf{y})$ must not be an eigenvector of the strain $\varepsilon(\mathbf{u}(\mathbf{y}))$, so this cannot happen. Therefore (4.61) is wrong and $A \neq 0$.

Consequently, the equations (4.54)-(4.56) are always nontrivial in our case. As these are linear ordinary differential equations of second order, the basis of solutions consists of functions of form $e^{\lambda z}$ and $z e^{\lambda z}$.

We now claim that there can be no solutions of form $z e^{\lambda z}$ to the system of differential equations in (4.52).

Assume, on the contrary, that a solution of form $z e^{\lambda z}$ exists. According to the theory of linear ODE, λ is a double zero of the three characteristic polynomials

$$a_k \lambda^2 + b_k \lambda + c_k = 0 \quad \text{for } k = (1, 2), (1, 3), (2, 3).$$

The discriminant has to vanish, so we have $\lambda = \frac{-b_k \pm \sqrt{b_k^2 - 4a_k c_k}}{2a_k} = \frac{-b_k}{2a_k}$, thus $b_k = -2\lambda a_k$ for $k = (1, 2), (1, 3), (2, 3)$; consequently we also have $c_k = 4\lambda^2 a_k$. Because of these proportionalities between a_k , b_k and c_k , the matrix A in (4.60) has rank 1. Therefore we have also a proportionality between the rows in A , i.e. the relations

$$\begin{aligned} a_{1,3} &= \gamma a_{1,2} & b_{1,3} &= \gamma b_{1,2} & c_{1,3} &= \gamma c_{1,2} \\ a_{2,3} &= \delta a_{1,2} & b_{2,3} &= \delta b_{1,2} & c_{2,3} &= \delta c_{1,2} \end{aligned} \quad (4.64)$$

4.4. Stability analysis

for some constants γ, δ . Using (4.57)-(4.59), the equations in (4.64) can be written in matrix form as

$$\begin{pmatrix} 0 & 0 & 0 & -\nu_3 + \gamma\nu_2 & -\gamma\nu_1 & \nu_1 \\ 0 & 0 & 0 & 0 & \delta\nu_2 & -\nu_3 - \delta\nu_1 & \nu_2 \\ -\nu_3 + \gamma\nu_2 & -\gamma\nu_1 & \nu_1 & -\zeta_3 + \gamma\zeta_2 & -\gamma\zeta_1 & \zeta_1 \\ \delta\nu_2 & -\nu_3 - \delta\nu_1 & \nu_2 & +\delta\zeta_2 & -\zeta_3 - \delta\zeta_1 & \zeta_2 \\ \zeta_3 - \gamma\zeta_2 & +\gamma\zeta_1 & -\zeta_1 & 0 & 0 & 0 \\ -\delta\zeta_2 & \zeta_3 + \delta\zeta_1 & -\zeta_2 & 0 & 0 & 0 \end{pmatrix} * \begin{pmatrix} \mathbf{g}_1 \cdot \boldsymbol{\zeta}_s \\ \mathbf{g}_2 \cdot \boldsymbol{\zeta}_s \\ \mathbf{g}_3 \cdot \boldsymbol{\zeta}_s \\ \mathbf{g}_1 \cdot \boldsymbol{\nu} \\ \mathbf{g}_2 \cdot \boldsymbol{\nu} \\ \mathbf{g}_3 \cdot \boldsymbol{\nu} \end{pmatrix} = 0, \quad (4.65)$$

which we interpret, as in (4.62), as linear system for the unknown variables $\{\mathbf{g}_1 \cdot \boldsymbol{\zeta}_s, \mathbf{g}_2 \cdot \boldsymbol{\zeta}_s, \mathbf{g}_3 \cdot \boldsymbol{\zeta}_s, \mathbf{g}_1 \cdot \boldsymbol{\nu}, \mathbf{g}_2 \cdot \boldsymbol{\nu}, \mathbf{g}_3 \cdot \boldsymbol{\nu}\}$. Now the matrix in (4.65) has rank 6, so the equations reduce to

$$\begin{aligned} \mathbf{g}_j \cdot \boldsymbol{\zeta}_s &= 0 & j &= 1, 2, 3 & \text{and} \\ \mathbf{g}_j \cdot \boldsymbol{\nu} &= 0 & j &= 1, 2, 3. \end{aligned} \quad (4.66)$$

As in (4.63), it follows from the second equation in (4.66) that $\boldsymbol{\nu}$ is an eigenvector of the strain $\varepsilon(\mathbf{u}(\mathbf{y}))$ corresponding to the eigenvalue 0. But this has been ruled out by hypothesis.

So the only solutions of (4.52) are of form $e^{\lambda z}$. The boundary condition (4.51) then leads to the unique solution of $\tilde{w}_1(z) = 0$. The same chain of arguments can be invoked to obtain $\tilde{w}_2(z) = 0$. Therefore the Lopatinskii condition is satisfied at \mathbf{y} . \square

4.4.4. Stability estimates and kernel characterization

In this section, we derive the main results of the paper. In Sections 4.4.2 and 4.4.3, we collected results about the systems \mathcal{A}_p , \mathcal{A}_μ and \mathcal{A}_ρ in Table 4.2. We now treat these operators on a case-by-case basis. For each operator, we give a stability estimate. In general, this estimate holds up to a finite dimensional kernel for operators with one experiment. We characterize this kernel, and show also injectivity of the operators for a larger number of measurements in the linearized problem in quantitative elastography.

We choose $p = 2$ and a number $l > 0$ with $p; l > n$, and a bounded and connected domain Ω with C^{l+2} -boundary.

The theory of [126], which we apply, requires that the solution variables lie in Sobolev spaces. In the following statements, we therefore suppose that we have a reference state (p, μ, ρ) with $\mu \in C^{2l+3}(\Omega)$, $\rho \in C^{2l+2}(\Omega)$ and for the reference displacement $\mathbf{u} = \mathcal{V}(p, \mu, \rho)$ in (4.25) we require $\mathbf{u} \in H^{l+2}(\Omega)$, $\mathbf{u}_{tt} \in H^l(\Omega)$. The existence of such a displacement field \mathbf{u} can be ensured by the regularity theory [86, Thm.8.1]. Moreover, we consider the solutions of the linearized equations (4.26) as follows: $\delta p \in H^{l+1}(\Omega)$, $\delta \mu \in H^{l+1}(\Omega)$, $\delta \rho \in H^l(\Omega)$, $\delta u_i \in H^{l+2}(\Omega)$ for $i = 1, 2, 3$.

4. Stability in the linearized problem of quantitative elastography

Note that, as exposed in section 4.4.1, the variables of the relevant systems are $(\delta p, \delta \mu, \delta \rho, \delta u_1, \delta u_2, \delta u_3)$. For subsequent analysis, we use the Douglis-Nirenberg numbers $(t_j)_{j=1}^6 = (1, 1, 0, 2, 2, 2)$, corresponding to the variables $(\delta p, \delta \mu, \delta \rho, \delta u_1, \delta u_2, \delta u_3)$, as well as $(s_i)_{i=1}^6 = (0, 0, 0, -2, -2, -2)$. – Note that for the particular operators $\mathcal{A}_\mu, \mathcal{A}_\rho, \mathcal{A}_p, \mathcal{A}_\lambda$, only four of those variables are used in the corresponding system.

In the following results, we apply Theorem 1 to obtain a *left regularizer* the particular operators \mathcal{A} , as in (4.22). Another name for \mathcal{A} possessing a left regularizer are that \mathcal{A} is a *left semi-Fredholm operator* [37, Ch. XI, §2], [66].

Theorem 2. *The operator $\mathcal{A}_\mu^{(r)}$ for $r \geq 1$ measurements, described in (4.31) and considered in the stationary case, has a left regularizer on Ω precisely when, for all $\mathbf{x} \in \Omega$,*

$$\det(\varepsilon(\mathbf{u}_k(\mathbf{x}))) \neq 0 \quad \text{for at least one measurement } 1 \leq k \leq r. \quad (4.67)$$

Then the stability estimate

$$\|\delta \mu\|_{H^{l+1}(\Omega)/K_1} \leq C \sum_{k=1}^r \|\delta \mathbf{u}_k\|_{H^{l+2}(\Omega)} \quad (4.68)$$

holds with a finite-dimensional kernel K_1 .

Proof. We first treat the case of \mathcal{A}_μ .

Recall that we are treating the equation

$$\mathcal{A}_\mu(\delta \mu, \delta \mathbf{u}) = (\mathcal{S}, \varphi),$$

and that the operator

$$\mathcal{A}_\mu = \mathcal{L}_\mu \times \mathcal{B} : D(p, l) \rightarrow R(p, l)$$

as described in Table 4.2, Section 4.4.1, has 6 equations in the interior and four variables $(\delta \mu, \delta u_1, \delta u_2, \delta u_3) = (\delta \mu, \delta \mathbf{u})$. The inhomogeneity is $\mathcal{S} = (0, 0, 0, \delta K_1, \delta K_2, \delta K_3)^\top$ and $\varphi = 0$.

The choice of Douglis-Nirenberg numbers corresponding to these variables is $(t_j)_{j=1}^4 = (1, 2, 2, 2)$ and $(s_i)_{i=1}^6 = (0, 0, 0, -2, -2, -2)$, $(\sigma_k)_{k=1}^3 = (-2, -2, -1)$, and the principal symbol of \mathcal{L}_μ is (4.43). Therefore, we have (according to (4.19) and (4.20)) the domain and range, respectively, as

$$\begin{aligned} D(p, l) &= H^{l+1}(\Omega) \times (H^{l+2}(\Omega))^3 \\ R(p, l) &= H^l(\Omega) \times (H^{l+2}(\Omega))^3 \times H^{l+\frac{5}{2}}(\Omega) \times H^{l+\frac{5}{2}}(\Omega) \times H^{l+\frac{3}{2}}(\Omega). \end{aligned}$$

By Corollary 2, the assumption (4.67) on the determinant of the strain $\varepsilon(\mathbf{u})$ of the reference state, is equivalent to \mathcal{L}_μ being elliptic. According to Proposition 2, the Lopatinskii condition is satisfied for $\mathcal{A}_\mu = \mathcal{L}_\mu \times \mathcal{B}$. Therefore, condition 1 of Theorem 1 is precisely when (4.67) holds, and this is true also for the two equivalent conditions 2-3 in Theorem 1.

Theorem 1 therefore implies the existence of a bounded operator $R_\mu : R(p, l) \rightarrow D(p, l)$ with

$$\mathcal{R}_\mu \mathcal{A}_\mu = \mathcal{I} - \mathcal{T}_\mu \quad (4.69)$$

and compact $\mathcal{T}_\mu : R(p, l) \rightarrow D(p, l)$.

The spectral theory for compact operators asserts that the kernel of $\mathcal{I} - \mathcal{T}_\mu$ is finite-dimensional [37, Ch.VII, Thm. 7.1]. By (4.69), the kernel $K = \ker(\mathcal{A}_\mu)$ is a subspace of $\ker(\mathcal{I} - \mathcal{T}_\mu)$. Consequently, K is finite-dimensional also, and hence closed. Therefore we can consider the quotient $D(p, l)/K$ as a Hilbert space.

Existence of the left regularizer in (4.69) implies that $\text{ran}(\mathcal{A}_\mu)$ is closed [37, Ch.XI, Thm. 2.3(ii)]. Therefore $\text{ran}(\mathcal{A}_\mu)$ is a Hilbert space. We apply the open mapping theorem [37, Ch.III, Thm. 12.1] to find that the inverse $\mathcal{A}_\mu^{-1} : \text{ran}(\mathcal{A}_\mu) \rightarrow D(p, l)/K$ is continuous:

$$\begin{aligned} \|(\delta\mu, \delta\mathbf{u})\|_{D(p, l)/K} &= \|\mathcal{A}_\mu^{-1} \mathcal{A}_\mu(\delta\mu, \delta\mathbf{u})\|_{D(p, l)/K} \\ &\leq C \|\mathcal{A}_\mu(\delta\mu, \delta\mathbf{u})\|_{R(p, l)} = C \|(\mathcal{S}, \varphi)\|_{R(p, l)}. \end{aligned} \quad (4.70)$$

holds. By (4.26), we have $\delta\mathbf{H} = \delta\mathbf{u}$ in \mathcal{S} . We set $K = K_1 \times K_2$ with $K_1 \subset H^{l+1}(\Omega)$. Then from (4.70), we obtain the estimate (4.68) for $r = 1$.

The case of $\mathcal{A}_\mu^{(r)}$ follows straight-forwardly by induction. \square

The availability of reference states satisfying (4.67) for $r = 2$ has already been discussed in Remark 2.

Note that the estimate (4.68) shows that there is the loss of only one derivative in the linearized problem of reconstructing $\delta\mu$ from $\delta\mathbf{u}$, thus this inverse problem is mildly ill-posed.

We now give an explicit characterization of the kernel of the operator $\mathcal{A}_\mu = \mathcal{A}_\mu^{(1)}$, which will be exploited in Corollary 4 to show injectivity of $\mathcal{A}_\mu^{(2)}$, the operator corresponding to two measurements.

Theorem 3. *Consider \mathcal{A}_μ , and suppose that the condition (4.67) with $r = 1$ holds. Then the estimate (4.68) holds with a one-dimensional kernel K_1 . The subspace K_1 is generated by the element*

$$\exp \int_{\mathbf{p}}^{\mathbf{x}} \mathbf{a}(\mathbf{y}) d\mathbf{y} \quad (4.71)$$

with fixed $\mathbf{p} \in \Omega$. Here, the vector field $\mathbf{a}(\mathbf{x})$ is uniquely determined by

$$\mathbf{a} \cdot \varepsilon(\mathbf{u})_i = -\nabla \cdot \varepsilon(\mathbf{u})_i, \quad i = 1, 2, 3, \quad (4.72)$$

where \mathbf{u} is a reference state for which (4.67) holds.

Proof. In the proof of the statement, we derive a representation for $\delta\mu$ on a connected set and then infer that the representation is valid on Ω by a topological argument.

Suppose, to begin with, that $(\delta\mu, \delta\mathbf{u}) \in D(p, l)$ is in the kernel of $\mathcal{A}_\mu = \mathcal{L}_\mu \times \mathcal{B}$.

4. Stability in the linearized problem of quantitative elastography

As we have $pl > n$, the Sobolev imbedding theorems (see [1, Thm.5.4.C]) imply that $\delta\mu \in H^{l+1}(\Omega)$ is continuously differentiable on Ω . In particular, we have that the set

$$A = \{\mathbf{x} \in \Omega : \delta\mu(\mathbf{x}) \neq 0\} \quad (4.73)$$

is open in Ω .

If $\delta\mu \equiv 0$, then the assertion is trivially satisfied. Otherwise, there exists a point $\mathbf{p} \in A$. In this case, consider the connected component V of \mathbf{p} in the topology of $A \subset \Omega$, that is

$$V = \bigcup \{U : \mathbf{p} \in U \subset A \text{ with } U \text{ connected in } A\}.$$

Lemma 1 implies that $V \subset A \subset \mathbb{R}^n$ is open; therefore, V is also path-connected.

Suppose now $\mathbf{x} \in V$. We analyze the 6 equations

$$\mathcal{L}_\mu(\delta\mu, \delta\mathbf{u}) = \begin{pmatrix} 2\nabla \cdot (\delta\mu \varepsilon(\mathbf{u})) + 2\nabla \cdot (\mu \varepsilon(\delta\mathbf{u})) \\ \delta\mathbf{u} \end{pmatrix} = 0 \quad \text{on } V.$$

From the last three equations, we immediately get $\delta\mathbf{u}|_V = 0$. From the first three equations, we then get that

$$\nabla \cdot (\delta\mu \varepsilon(\mathbf{u})) = 0 \quad \text{on } V$$

for the element $\delta\mu$, and hence

$$\nabla \delta\mu \cdot \varepsilon(\mathbf{u})_i = -\delta\mu \nabla \cdot \varepsilon(\mathbf{u})_i \quad i = 1, 2, 3 \text{ on } V. \quad (4.74)$$

Evaluating (4.74) at the point $\mathbf{x} \in V \subset A$ and dividing by $\delta\mu(\mathbf{x})$ (which, by (4.73), is non-zero) shows that

$$\frac{\nabla \delta\mu(\mathbf{x})}{\delta\mu(\mathbf{x})} = \nabla \log \delta\mu(\mathbf{x}) = \mathbf{a}(\mathbf{x}), \quad (4.75)$$

with \mathbf{a} determined by (4.72).

Actually, the conditions (4.67) and (4.72) can be used to define $\mathbf{a}(\mathbf{x})$ uniquely for $\mathbf{x} \in \Omega$ and that \mathbf{a} is continuous. To see this, observe that from (4.72), we have that $\varepsilon(\mathbf{u}) * \mathbf{a} = -[\nabla \cdot \varepsilon(\mathbf{u})_1, \nabla \cdot \varepsilon(\mathbf{u})_2, \nabla \cdot \varepsilon(\mathbf{u})_3]$. With (4.67), we then have

$$\mathbf{a} = -(\varepsilon(\mathbf{u}))^{-1} * [\nabla \cdot \varepsilon(\mathbf{u})_1, \nabla \cdot \varepsilon(\mathbf{u})_2, \nabla \cdot \varepsilon(\mathbf{u})_3]. \quad (4.76)$$

Now $\mathbf{u} \in (H^{l+2}(\Omega))^3$ implies that the entries of $\varepsilon(\mathbf{u})$ lie in $H^{l+1}(\Omega)$ and that $\nabla \cdot \varepsilon(\mathbf{u})_i \in H^l(\Omega)$ for $i = 1, 2, 3$. Applying Cramer's rule to (4.76) yields that $\mathbf{a} \in H^l(\Omega)$. Using the inequality $pl > n$ and the Sobolev embedding theorem [1, Thm.5.4.C], we then conclude that \mathbf{a} is continuous on Ω .

Now consider the vector field \mathbf{a} and calculate the path integral from \mathbf{p} to \mathbf{x} to find

$$\int_{\mathbf{p}}^{\mathbf{x}} \mathbf{a}(\mathbf{y}) d\mathbf{y} \stackrel{(4.75)}{=} \int_{\mathbf{p}}^{\mathbf{x}} \nabla \log \delta\mu(\mathbf{y}) d\mathbf{y} = \log \delta\mu(\mathbf{x}) - \log \delta\mu(\mathbf{p}) = \log \left(\frac{\delta\mu(\mathbf{x})}{\delta\mu(\mathbf{p})} \right).$$

From this identity, we have the representation

$$\delta\mu(\mathbf{x}) = \delta\mu(\mathbf{p}) \exp \int_{\mathbf{p}}^{\mathbf{x}} \mathbf{a}(\mathbf{y}) d\mathbf{y}, \quad \mathbf{x} \in V \quad (4.77)$$

for the values $\delta\mu$ on the set $V \subset A \subset \Omega$. Note that the function on the right hand side of (4.77) is continuous and defined on the whole domain Ω .

We now claim that actually, we have

$$V = \Omega, \quad (4.78)$$

such that the representation formula (4.77) holds for $\mathbf{x} \in \Omega$.

Assume, on the contrary, that $V \subsetneq \Omega$. We then also have that

$$A \subsetneq \Omega$$

(otherwise $\Omega = A = V \cup V_1$, with $V_1 = A \setminus V$ open and nontrivial, $V \cap V_1 = \{\}$, so Ω would not be connected).

Therefore, the assumptions of Lemma 2 are satisfied. Consequently, there exists a point $\mathbf{q} \in \partial V \setminus A$, where ∂V is the boundary of V in Ω . As $\mathbf{q} \notin A$, we have, by (4.73), that

$$\delta\mu(\mathbf{q}) = 0. \quad (4.79)$$

As $\mathbf{q} \in \partial V$, there exists a sequence $\mathbf{v}_n \in V$ with

$$\mathbf{v}_n \rightarrow \mathbf{q} \quad \text{in } \Omega. \quad (4.80)$$

By the representation (4.77), together with (4.80), we have

$$\delta\mu(\mathbf{v}_n) \stackrel{(4.77)}{=} \delta\mu(\mathbf{p}) \exp \int_{\mathbf{p}}^{\mathbf{v}_n} \mathbf{a}(\mathbf{y}) d\mathbf{y} \rightarrow \underbrace{\delta\mu(\mathbf{p})}_{\neq 0} \underbrace{\exp \int_{\mathbf{p}}^{\mathbf{q}} \mathbf{a}(\mathbf{y}) d\mathbf{y}}_{> 0} \neq 0 \quad (4.81)$$

On the other hand, the continuity of $\delta\mu$, equation (4.79) and (4.80) imply that

$$\delta\mu(\mathbf{v}_n) \rightarrow 0. \quad (4.82)$$

As (4.81) and (4.82) contradict each other, we infer that the assumption $V \subsetneq \Omega$ is wrong. Therefore, as asserted in (4.78), $V = \Omega$ holds.

Therefore, for any $(\delta\mu, \delta\mathbf{u}) \in \ker \mathcal{A}_\mu = K_1 \times \{0\}$ with $\delta\mu \neq 0$, the representation of $\delta\mu$ in (4.77) is valid for $\mathbf{x} \in \Omega$. This shows that (4.71) is a generating element for K_1 . Therefore $\dim(K_1) = 1$. \square

Corollary 4. *Let $\mathbf{u}_1 \neq \mathbf{u}_2$ be two quasi-static elastic deformations satisfying (4.5) with different force terms $\mathbf{F}_1, \mathbf{F}_2$. Let the condition (4.67) hold.*

As described in (4.31), let $\mathcal{A}_\mu^{(2)}(\delta\mu, \delta\mathbf{u}_1, \delta\mathbf{u}_2)$ be the corresponding linearized operator. Then we have that

$$\ker(\mathcal{A}_\mu^{(2)}) = \{(0, 0, 0)\}.$$

4. Stability in the linearized problem of quantitative elastography

Proof. Let $(\delta\mu, \delta\mathbf{u}_1, \delta\mathbf{u}_2) \in \ker(\mathcal{A}_\mu^{(2)})$.

From (4.31), we immediately get that $\delta\mathbf{u}_1 = \delta\mathbf{u}_2 = 0$ on $\overline{\Omega}$. The other equations in (4.31) yield

$$\begin{aligned}\nabla \cdot (\delta\mu \varepsilon(\mathbf{u}_1)) &= 0 \\ \nabla \cdot (\delta\mu \varepsilon(\mathbf{u}_2)) &= 0.\end{aligned}$$

such that together with the boundary data we have

$$\begin{aligned}\nabla \cdot (\delta\mu \varepsilon(\mathbf{u}_1 - \mathbf{u}_2)) &= 0 \\ (\mathbf{u}_1 - \mathbf{u}_2)|_{\partial\Omega} &= 0.\end{aligned}\tag{4.83}$$

Suppose that $\delta\mu \neq 0$. Then there exists a point $\mathbf{p} \in \Omega$ with $\delta\mu(\mathbf{p}) \neq 0$. As in the proof of Theorem 3, where we derived the representation formula (4.77) for $\mathbf{x} \in \Omega$, there exists a continuous vector field \mathbf{a} such that

$$\delta\mu(\mathbf{x}) = \delta\mu(\mathbf{p}) \exp \int_{\mathbf{p}}^{\mathbf{x}} \mathbf{a}(\mathbf{y}) d\mathbf{y}, \quad \mathbf{x} \in \Omega.\tag{4.84}$$

This implies that $\delta\mu(\mathbf{x}) > 0$ for all $\mathbf{x} \in \Omega$. Therefore, the condition $\text{ess inf}_\Omega \mu = \text{ess inf}_\Omega \mu_0 > 0$ in [86, (2.2)] is satisfied.

The uniqueness result [86, Thm.5.2] then implies that, from (4.83), we have that $\mathbf{u}_1 = \mathbf{u}_2$. But this is contradiction to our assumption.

Therefore, we have $\ker(\mathcal{A}_\mu^{(2)}) = \{(0, 0, 0)\}$. \square

Remark 3. We note that equation (4.74) and the analytical solution (4.77) has been found in [26] in a different context for the analysis of the non-linear problem with constant coefficients λ and ρ . Applying the technique of Corollary 4 to the inverse problem in [26, sec. 4b] yields that for two measurements, the coefficient μ in [26] can be uniquely reconstructed without prior knowledge of $\mu(x_0)$.

In the subsequent part of the section we give the stability criteria for the operators \mathcal{A}_ρ , \mathcal{A}_p and \mathcal{A}_λ .

Theorem 4. *The operator $\mathcal{A}_\rho^{(r)}$ for r measurements has a left regularizer on any smooth subdomain $W \subset \Omega \times [0, T]$ precisely when, for all $(\mathbf{x}, t) \in \overline{W}$,*

$$(\mathbf{u}_k)_{tt}(\mathbf{x}, t) \neq 0 \quad \text{for at least one measurement } 1 \leq k \leq r.\tag{4.85}$$

One has the stability estimate

$$\|\delta\rho\|_{H^{l+1}(W)} \leq C \sum_{k=1}^r \|\delta\mathbf{u}_k\|_{H^{l+2}(W)}.\tag{4.86}$$

Proof. We first treat \mathcal{A}_ρ . The case of $\mathcal{A}_\rho^{(r)}$ follows by induction.

The stability criterion in Theorem 1 is established for domains with $C^{l+\max t_j}$ boundary. Upon careful checking of the proof [126, §6], the only place where this assumption enters is the existence of a partition of unity. Now our domain is $\Omega \times [0, T]$, The construction of a partition of unity easily generalizes to cylindrical

4.4. Stability analysis

domains $\Omega \times [0, T]$, where Ω has $C^{l+\max t_j}$ boundary. Therefore, we can apply Theorem 1 to the problems with cylindrical domains.

The ellipticity condition has been assured in Corollary 3, and the Lopatinskii condition is satisfied according to Proposition 3. The assumptions in these results give the requirement $\mathbf{u}_{tt}(\mathbf{x}, t)_{\overline{W}} \neq 0$. With that, the equivalent conditions of Theorem 1 are fulfilled and we apply the result as in the proof of Theorem 2.

There appears no kernel in (4.86) for the following reason: The Douglis-Nirenberg numbers for the operator \mathcal{A}_ρ are $(t_j)_{j=1}^4 = (0, 2, 2, 2)$ and $(s_i)_{i=1}^6 = (0, 0, 0, -2, -2, -2)$. On the right hand side of estimate (4.23), only the variables with $t_j > 0$ appear, which are in this case $\delta \mathbf{u}_k$ for $k = 1, 2, 3$. \square

Theorem 5. *The operator \mathcal{A}_p in Table 4.2, considered in the stationary case, has a left regularizer on Ω , and we have the estimate*

$$\|\delta p\|_{H^{l+1}(\Omega)/K_3} \leq C \|\delta \mathbf{u}\|_{H^{l+2}(\Omega)}. \quad (4.87)$$

Here, the kernel K_3 consists of the (one-dimensional) space of constant functions on Ω .

Proof. The proof of the stability estimate with a finite-dimensional kernel is the same as in Theorem 2, using Corollary 1 and Proposition 2 in this case.

Suppose that $(\delta \mu, \delta \mathbf{u})$ is in the kernel $K = \ker(\mathcal{A}_p) = \mathcal{L}_p \times \mathcal{B}$. Consideration of the system

$$\mathcal{L}_p(\delta p, \delta \mathbf{u}) = \begin{pmatrix} \nabla \delta p + 2 \nabla \cdot (\mu \varepsilon(\delta \mathbf{u})) \\ \delta \mathbf{u} \end{pmatrix} = 0 \quad \text{on } \Omega$$

shows that $\delta \mathbf{u} = 0$, and consequently $\nabla \delta p = 0$. Therefore, we have $K = K_3 \times \{0\}$, with K_3 the constant functions on Ω . \square

Note that, with the same method, but using Remark 1, one obtains a conditional stability result for the operator \mathcal{A}_λ :

Theorem 6. *The operator $\mathcal{A}_\lambda^{(r)}$ corresponding to r measurements, considered in the stationary case, has a left regularizer on Ω precisely when, for all $\mathbf{x} \in \Omega$,*

$$\nabla \cdot \mathbf{u}_k(\mathbf{x}) \neq 0 \quad \text{for at least one measurement } 1 \leq k \leq r, \quad (4.88)$$

Then the stability estimate

$$\|\delta \lambda\|_{H^{l+1}(\Omega)/K_4} \leq C \sum_{k=1}^r \|\delta \mathbf{u}_k\|_{H^{l+2}(\Omega)} \quad (4.89)$$

holds for a finite-dimensional kernel K_4 .

By the same method or proof as in Theorem 7, one proves the following kernel characterization for \mathcal{A}_λ :

4. Stability in the linearized problem of quantitative elastography

operator	$\mathcal{A}_\mu^{(r)}$	$\mathcal{A}_\rho^{(r)}$	$\mathcal{A}_p^{(r)}$	$\mathcal{A}_\lambda^{(r)}$
ellipticity cond.	$\det(\varepsilon(\mathbf{u}_k)) \neq 0$	$(\mathbf{u}_k)_{tt} \neq 0$	–	$\nabla \cdot \mathbf{u}_k \neq 0$
stability est.	$\ \delta\mu\ _{H^{l+1}/K_1} \leq$ $C \sum \ \delta\mathbf{u}_k\ _{H^{l+2}}$	$\ \delta\rho\ _{H^{l+1}} \leq$ $C \sum \ \delta\mathbf{u}_k\ _{H^{l+2}}$	$\ \delta p\ _{H^{l+1}/K_3} \leq$ $C \ \delta\mathbf{u}\ _{H^{l+2}}$	$\ \delta\lambda\ _{H^{l+1}/K_4} \leq$ $C \sum \ \delta\mathbf{u}_k\ _{H^{l+2}}$
$\dim(\ker \mathcal{A}^{(1)})$	1	0	1	1
$\dim(\ker \mathcal{A}^{(2)})$	0	0	2	≤ 1

Table 4.3.: Stabilities estimates for various linearized problems in elastography; conditions for the reference state in Theorems 2, 4, 5, 6 to hold for every point for at least one displacement field \mathbf{u}_k , $1 \leq k \leq r$ in an imaging experiment in elastography; results of the kernel characterizations in Theorems 3, 4, 5, 7.

Theorem 7. Consider \mathcal{A}_λ , and suppose that the condition (4.88) with $r = 1$ holds. Then the estimate (4.89) holds with a one-dimensional kernel K_4 . The subspace K_4 is generated by the element

$$\exp \int_{\mathbf{p}}^{\mathbf{x}} \mathbf{a}(\mathbf{y}) d\mathbf{y} \quad (4.90)$$

with fixed $\mathbf{p} \in \Omega$. Here, the vector field $\mathbf{a}(\mathbf{x})$ is uniquely determined by

$$\mathbf{a} = -\frac{1}{\nabla \cdot \mathbf{u}} \nabla(\nabla \cdot \mathbf{u}), \quad (4.91)$$

where \mathbf{u} is a reference state for which (4.88) holds.

However, for the analysis of $\mathcal{A}_\lambda^{(2)}$, the technique of Corollary 4 is not applicable, as the condition $\text{ess inf}_\Omega \mu_0 > 0$ in [86, (2.2)] is not satisfied.

4.5. Discussion

1. The theorems show that the interior information \mathbf{u} provided in elastography makes the reconstruction of the biomechanical parameters μ , ρ , as well as reconstruction of p , stable. While the operators $\mathcal{A}_{p\mu}$ and $\mathcal{A}_{p\mu\rho}$ are non-elliptic for any number of measurements, we obtained criteria for the ellipticity of the linearizations \mathcal{A}_p , \mathcal{A}_μ and \mathcal{A}_ρ of the quantitative elastography problems defined in Section 4.4.1, see table 4.3. In the stability

estimates in (4.68), (4.87) and (4.86), one has the loss of only one derivative, thus mild ill-posedness.

In the research for hybrid conductivity problems, ellipticity has been investigated theoretically and numerically. Ellipticity was found to yield optimal stability estimates, avoid blurring effects, accurate reconstruction of edges, and absence of propagation of singularities [18, 21, 68, 70, 71, 90].

Note that failure of ellipticity in our cases entails non-existence of a left regularizer non-existence of a left regularizer is equivalent to either $\dim \ker(\mathcal{A}) = \infty$ or the range of \mathcal{A} not being closed for the particular Sobolev spaces involved [37, XI, Thm. 2.3]. This does not mean that necessarily, the linearized problem will be unstable for all data in any function space. For example, consider the case of Corollary 2: at a point \mathbf{x} , there might be just one direction $\boldsymbol{\xi}$ for which ellipticity does not hold. Then one can form the conjecture that reconstruction can still be stable if there is no edge along this direction (see the related discussion in [71, 6(ii)]). We plan to address this in future work.

2. The ellipticity conditions for \mathcal{A}_λ and \mathcal{A}_ρ seem to be natural. Concerning λ , literature actually often assumes the incompressibility condition $\nabla \cdot \mathbf{u} = 0$ on the whole of Ω [11, 25, 81, 111]. In this case, of course, the measurement data are not dependent on λ , so this parameter cannot be reconstructed then. – But in the compressible case, where $\nabla \cdot \mathbf{u} \neq 0$ on the whole of Ω , there still might be single points \mathbf{x} at which $\nabla \cdot \mathbf{u}(\mathbf{x}) = 0$. Notice that, as stated in Remark 1, the ellipticity analysis along the lines of this article then entails that at such points \mathbf{x} , ellipticity is lost and every direction is a characteristic. – Concerning the particular data one has, it might then be better to reconstruct the pressure $p = \lambda \nabla \cdot \mathbf{u}$, with the operator \mathcal{A}_p being always elliptic.

Similarly for ρ : If $\mathbf{u}_{tt} = 0$ on the whole of Ω , the parameter ρ does not appear in the model, so it cannot be reconstructed from the measurements. If, on the other hand, $\mathbf{u}_{tt}(\mathbf{x}) = 0$ only for particular points \mathbf{x} , the analysis says that ellipticity is lost at these points \mathbf{x} , and every direction is a characteristic for \mathcal{A}_ρ there.

3. The ellipticity condition for reconstruction of μ turned out to be the non-singular strain condition in (4.42) resp. (4.67); this condition is a generalization of the condition (4.46), whose relevance for the inversion has been proposed and discussed in [20, 3.3]. – Apart from this characterization, points of singular strain have been found in experiments, namely at the intersection of nodal lines or surfaces in early experiments of elastography using eigenmodes (see [107, 108, 128]). Empirically, it was observed that these patterns could be avoided by choosing multi-frequency excitation functions \mathbf{F} [108].

4.6. Conclusion

We have applied a general method of linear PDE to linearized problems in quantitative elastography in \mathbb{R}^3 , with interior data given. We analyzed ellipticity conditions of the PDE problem augmented with the interior data. We deduced simple criteria for the stability of the linearization. This analysis revealed non-ellipticity for the joint reconstruction of all parameters, but stable reconstruction of the shear modulus μ and the hydrostatic pressure $p = \lambda \nabla \cdot \mathbf{u}$. For the reconstruction of μ and ρ , the kernel in the linearization was shown to be trivial for choice of two measurements. The results give a mathematical explanation which biomechanical parameters can be stably reconstructed from interior measurement data \mathbf{u} .

Acknowledgements

We thank Joyce McLaughlin, Dustin Steinhauer, Guillaume Bal, Josef Schicho, José A. Iglesias and Kristoffer Hoffmann for fruitful discussions. Moreover, we want to express our gratitude to the referees and their comments. Support from the Austrian Science Fund (FWF) in project S10505-N20 is also acknowledged.

4.7. Technical lemmas

We give here the proof of two topological lemmas which we use in the determination of the kernel in Theorem 3.

Lemma 1. *Let $A \subset \Omega$ be open, and let $\mathbf{p} \in A$. Let V be the connected component of \mathbf{p} in the topology of $A \subset \Omega$. Then V is open in Ω .*

Proof. Let $\mathbf{x} \in V \subset A$ be an arbitrary point in V . As $\mathbf{x} \in A$ and A is open, there exists an $\varepsilon > 0$ such that

$$U_1 := \{\mathbf{z} \in \Omega : |\mathbf{x} - \mathbf{z}| < \varepsilon\} \subset A.$$

Observe that the set U_1 is connected and $\mathbf{x} \in V \cap U_1$. From [92, Thm.23.3], it then follows that $V \cup U_1 \subset A$ is a connected set.

Among all subsets of A which are connected and contain \mathbf{p} , the component V is maximal. Therefore $\mathbf{p} \in V \cup U_1 = V$, or equivalently $U_1 \subset V$. This shows that V is open in Ω . \square

Lemma 2. *Let $A \subsetneq \Omega \subset \mathbb{R}^n$ be open and bounded, and let $\mathbf{p} \in A$. Let V be the connected component of \mathbf{p} in the topology of $A \subset \Omega$. Let ∂V be the boundary of V in the topology of Ω . Then there exists a point*

$$\mathbf{q} \in \partial V \setminus A.$$

Proof. We use Lemma 1 and prove the statement in two steps: first, we find a point $\mathbf{q} \in \partial V \setminus V$; second, we show that $\mathbf{q} \notin A$.

Claim 1: There exists a point $\mathbf{q} \in \partial V \setminus V$.

We have that $V \subset A \subsetneq \Omega$. Therefore, there exists an element

$$\mathbf{y} \in \Omega \setminus V. \quad (4.92)$$

Consider the mapping

$$\begin{aligned} f : \overline{V} &\rightarrow \mathbb{R} \\ \mathbf{v} &\mapsto |\mathbf{y} - \mathbf{v}|. \end{aligned}$$

Observe that $\overline{V} \subset \Omega$ is closed and bounded, hence a compact set; observe also that f is continuous. Therefore, a minimum exists, that is:

$$\exists \mathbf{q} \in \overline{V} : |\mathbf{y} - \mathbf{q}| = \min_{\mathbf{v} \in \overline{V}} \{|\mathbf{y} - \mathbf{v}|\}. \quad (4.93)$$

We now show that, actually, the point $\mathbf{q} \in \overline{V} = V \cup \partial V$ is not contained in V . Once this is shown, Claim 1 is proven.

Assume, on the contrary, that $\mathbf{q} \in V$. According to Lemma 1, we then would have an ε , such that

$$U_2 := \{\mathbf{z} : |\mathbf{q} - \mathbf{z}| < \varepsilon\} \subset V.$$

Without loss of generality, we can assume $\varepsilon < 2$. Now, using the element \mathbf{y} from (4.92), define the point

$$\mathbf{w} := \mathbf{q} + \frac{\varepsilon}{2}(\mathbf{y} - \mathbf{q}), \quad \mathbf{w} \in U_2.$$

Then calculate

$$\begin{aligned} |\mathbf{y} - \mathbf{w}| &= |\mathbf{y} - \mathbf{q} - \frac{\varepsilon}{2}(\mathbf{y} - \mathbf{q})| = |(\mathbf{y} - \mathbf{q})(1 - \frac{\varepsilon}{2})| \\ &\leq |\mathbf{y} - \mathbf{q}| \underbrace{(1 - \frac{\varepsilon}{2})}_{< 1} < |\mathbf{y} - \mathbf{q}|. \end{aligned}$$

This would contradict (4.93). – Therefore, $\mathbf{q} \notin V$.

Claim 2: The point \mathbf{q} in (4.93) does not belong to A .

We prove this claim indirectly. Assume that

$$\mathbf{q} \in A. \quad (4.94)$$

Recall that, according to Claim 1, $\mathbf{q} \in \partial V$, where ∂V is the boundary of V in Ω . Hence there exists a sequence $\mathbf{v}_n \in V$ with $\mathbf{v}_n \rightarrow \mathbf{q}$ in the topology of Ω .

We assert that

$$\mathbf{v}_n \rightarrow \mathbf{q} \quad \text{in the topology of } A. \quad (4.95)$$

4. Stability in the linearized problem of quantitative elastography

To see this, choose an open set $U_3 \subset A$ with $\mathbf{q} \in U_3$. Because A is open in Ω , U_3 is open in Ω as well. Now the elements \mathbf{v}_n converge to \mathbf{q} in Ω ; therefore, there exists an N , such that for all $n \geq N : \mathbf{v}_n \in U_3$; hence we have (4.95).

The set V , which is the connected component of the point \mathbf{p} , is closed in the topology of A [92, Thm.23.4]. But a closed set contains all its limit points. Therefore, with (4.95), we would have that the limit of the sequence $\mathbf{v}_n \in V$ lies in V , so $\mathbf{q} \in V$. But this is a contradiction to Claim 1. – Therefore, contrary to (4.94), we have $\mathbf{q} \notin A$.

□

5. Convergent regularization methods for quantitative elastography

Authors & Contributions The authors are TW and O. Scherzer. The development of this article was a gradual, cooperative process, and each of the authors made significant contributions to every aspect of the paper.

Publication status Manuscript in preparation for publication

Abstract:

Iterative algorithms are widely employed in quantitative elastography. However, in most cases they are used without a detailed convergence analysis. Such an analysis is the scope of this paper. In particular, in this paper we analyze Tikhonov regularization and the Levenberg-Marquardt iteration method, respectively. A convergence analysis for Tikhonov regularization is obtained from the geometric theory of Chavent and Kunisch, which provides sufficient conditions for global optimization in a neighborhood of the solution in terms of the curvature of the forward problem. The convergence analysis for the Levenberg-Marquardt iteration relies on the tangential cone condition. We apply the theory for both methods for quasi-static elastography. Numerical experiments are provided.

Convergent regularization methods for quantitative elastography

Thomas Widlak¹, Otmar Scherzer^{1,2}

¹ Computational Science Center, University of Vienna,
Oskar-Morgenstern-Platz 1, 1090 Vienna, Austria

² RICAM, Austrian Academy of Sciences,
Altenberger Straße 69, 4040 Linz, Austria

Contents

5.1	Introduction	65
5.2	Model for quantitative elastography for incompressible media	67
5.3	Stability of the linearization and implications of the implicit function theorem	68
5.4	Convergence for Tikhonov regularization: Geometric theory .	70
5.5	The Levenberg Marquardt iteration and its convergence prop- erties	74
5.6	Minimization process	77
5.7	Conclusion	82
5.8	Technical results	83

5.1. Introduction

Elastography is a medical imaging technology; its current applications range from detection of cancer in the breast and in the prostate, liver cirrhosis and characterization of atherosclerotic plaque in hardened coronary vessels [7, 30, 40, 106, 132, 134, 137]. Medical elastography utilizes the fact that the health state is reflected by elastic properties [4, 67]. The most important elastic property for medical diagnosis is the shear modulus μ . The contrast of healthy versus malignant tissue can change up to a factor of 4 [116].

Besides medical elastography, imaging elastic properties is important in non-destructive testing, such as the detection of cracks and inclusions, and advanced applications, such as imaging of nano-particles [10, 32].

In this work, we restrict the focus to elastography as it is used in medicine; this problem has a peculiar structure, as interior information is used, as explained in the following:

Medical elastography is performed in combination with various established imaging techniques, such as ultrasound imaging [75, 103], MRI [81, 93] or OCT [94, 127]. The measurement principle is this:

1. record data with the ground modality (e.g., US, MRI or OCT);
2. perturb the tissue mechanically, and
3. record data of the perturbed tissue again.

Qualitative elastography (see references just cited) then provides *interior data* of the displacement $\mathbf{u}|_{\Omega}$ of the tissue on the imaging domain Ω . According to the specific excitation used, \mathbf{u} can be space or space-time-dependent. In this article, we consider the quasi-static elastography experiment, using space-dependent $\mathbf{u}(\mathbf{x})$. – Using different mechanical excitations (e.g., pushing from different directions), several experiments can be performed, and a family of interior data $\mathbf{u}_i|_{\Omega}$, $1 \leq i \leq k$ are collected. *Quantitative elastography* then determines elastic parameters from $\mathbf{u}_i|_{\Omega}$ [40].

To recover the material parameters, an inverse problem based on an elasticity model has to be solved [9, 40]. Various models based on linear elasticity, viscoelasticity or hyperelasticity have been considered for elastography [40]. Given the displacement \mathbf{u} , the mathematical problems in quantitative elastography are the recovery of parameters such as the Lamé parameter λ , the shear modulus μ , the density ρ , or recovery of the shear wave speed $\sqrt{\frac{\mu}{\rho}}$ [24, 40]. These problems are non-linear inverse problems.

Numerical inversion schemes for all kind of experimental varieties of elastography (see, e.g., [11, 54, 83, 84, 85] and the reviews in [40, 124]) have been developed. The proposed algorithms are either direct algorithms, using reconstruction formulae, or iterative algorithms.

5. Convergent regularization methods for quantitative elastography

For the simplest models in quantitative elastography, *mathematical* results have been obtained also. Uniqueness results, for example have been obtained in [20, 25, 63, 87, 114]. For particular algorithms, stability and convergence has been treated. E.g., [20] analyzed an algorithm to recover two material parameters using ODE-based and variational tools. In [8], the problem of reconstructing one parameter μ was studied and Lipschitz estimates for the nonlinear problem are obtained in a quasi-static incompressible setting. This was used to show convergence of the Landweber iteration.

In the paper [136], we analyzed several models in the framework of [18, 126] and studied the ellipticity properties of the *linearized* problem $\mathbf{u}_i \rightarrow \mu$. Using two static measurements $\mathbf{u}_1, \mathbf{u}_2$, injectivity and stability results for the linearized reconstruction problem have been obtained.

In this paper, we apply those ellipticity results to study the *nonlinear* reconstruction problem of μ in a quasi-static incompressible model. In particular, we apply the theory for an analysis of the *Tikhonov regularization* and for the *Levenberg-Marquardt iteration* for recovery of μ .

The Tikhonov regularization technique is the most popular regularization technique. For linear inverse problems, it is mathematically well understood, and well-posedness and convergence of the method is a standard result[44]. For nonlinear problems, the problem has to be studied separately.

We employ here the geometric theory of [34, 35] together with [136] to obtain well-posedness of Tikhonov regularization for recovery of μ as well as a convergence analysis.

The Levenberg-Marquardt iteration, on the other hand, is a quasi-Newton method for iterative regularization of inverse problems [64]. A convergence theory is provided in [59] (see also [64]), and that analysis hinges on the *tangential cone condition*.

Inspired by [23], we use the ellipticity analysis in [136] to derive the tangential cone condition. By this, we obtain a convergence result of the Levenberg-Marquardt iteration to recover μ .

The structure of the paper is as follows: in Section 5.2, we review the elasticity model which we are using. In Section 5.3, we review the results on the linearized problem and the implications of the implicit function theorem. The main results are contained in the next two sections: In Section 5.4, the geometric theory is exposed, and applied to Tikhonov regularization. In Section 5.5, the convergence analysis of the Levenberg-Marquardt iteration is treated, and we give a discussion of the results. In Section 5.6, we give numerical experiments demonstrating the inversion procedure, reconstructing the shear modulus from two internal measurements. The appendix contains technical results.

5.2. Model for quantitative elastography for incompressible media

In [136] we investigated mathematical formulations of quantitative elastography; we studied the linearization of several imaging models and analyzed their ellipticity properties. For some of the models, we could derive stability estimates and also injectivity. One of these results concerned the case of incompressible media and the reconstruction of a single parameter, the shear modulus μ . We therefore investigate convergence issues for the corresponding nonlinear problem.

We model the response of a linear elastic and isotropic incompressible material with the shear modulus μ and to (quasi-) static forces $\mathbf{f}_1, \mathbf{f}_2$:

$$\nabla \cdot (\mu \varepsilon(\mathbf{u}_i)) = \mathbf{f}_i, \quad i = 1, 2 \quad (5.1)$$

$$\mathbf{u}_i|_{\partial\Omega} = \mathbf{g}_i, \quad i = 1, 2. \quad (5.2)$$

Here, \mathbf{u} is the elastic displacement of the material, and $\varepsilon(\mathbf{u}) = \frac{1}{2}(\nabla \mathbf{u} + \nabla \mathbf{u}^\top)$.

As outlined in the introduction, in quasi-static elastography, the displacement field \mathbf{u} is estimated by a comparison of imaging data before and after mechanical compression. The recovery the shear modulus μ from \mathbf{u} is the problem of quantitative elastography.

For inversion, we assume that \mathbf{g}_i (on $\partial\Omega$) and \mathbf{f}_i (on Ω) are determined by the experiment. Then we define the nonlinear mapping

$$\varphi : \mu \mapsto (\mathbf{u}_1, \mathbf{u}_2). \quad (5.3)$$

The inverse problem is to recover μ from knowledge of $(\mathbf{u}_1, \mathbf{u}_2)$.

Let Ω be a bounded, domain with smooth boundary in \mathbb{R}^n , and let $\mathbf{f} = (\mathbf{f}_1, \mathbf{f}_2)$ be in $(H^l(\Omega))^2$. We have (see appendix 5.8.1) that this is a continuous mapping in the following spaces:

$$E := H^{l+1}(\Omega) \rightarrow F := (H^{l+2}(\Omega))^n. \quad (5.4)$$

Here, l is chosen such that $l > \frac{n}{2}$. Then, according to [1, Thm.5.23], one has that $H^l(\Omega)$ is a Banach algebra, which will be needed later.

We will consider the mapping for a defined subset $C \subset E$:

$$\varphi : C \rightarrow F, \quad (5.5)$$

where the subset C consists of bounded parameters:

$$C = \{\mu \in H^{l+1}(\Omega) \cup L^\infty(\Omega) : 0 < a \leq \|\mu\|_{l+1} \leq b < \infty, \\ 0 < c \leq \text{ess inf}(\mu) \leq \text{ess sup}(\mu) \leq d < \infty\} \quad (5.6)$$

Note that, as in [18, 23], we use the Sobolev setting (5.4) for the theoretical analysis. For the actual inversion, we compose (5.4) with the embedding $i : F = (H^{l+1}(\Omega))^n \hookrightarrow (L^2(\Omega))^n$.

5.3. Stability of the linearization and implications of the implicit function theorem

We recall the setting and results from the theory [136] on the linearized problem in quantitative elastography.

Consider a reference state μ with two measurements $\mathbf{u}_1, \mathbf{u}_2$ as above. We calculate for $\delta\mu \in E = H^{l+1}(\Omega)$ the linearization with respect to μ , denoted by $\delta\mathbf{u}_i = \delta\mathbf{u}_i[\mu](\delta\mu)$. (Dependence of $\delta\mathbf{u}_i$ from μ or $\delta\mu$ is dropped when they are clear from the context.) As seen from [136, Table 1], this quantity is characterized by the following equations:

$$\nabla \cdot (\mu \varepsilon(\delta\mathbf{u}_i)) = -\nabla \cdot (\delta\mu \varepsilon(\mathbf{u}_i)), \quad \text{on } \Omega, \quad i = 1, 2 \quad (5.7)$$

$$\delta\mathbf{u}_i|_{\partial\Omega} = 0 \quad i = 1, 2. \quad (5.8)$$

Fréchet differentiability of $\mathbf{u}_i = \mathbf{u}_i(\mu)$ is shown in appendix 5.8.2. Therefore, the forward map φ in (5.3), (5.5) is Fréchet differentiable with derivative

$$\delta\varphi = (\delta\mathbf{u}_1, \delta\mathbf{u}_2) : E = H^{l+1} \rightarrow F = (H^{l+2})^n. \quad (5.9)$$

If, for a reference state μ and fixed data \mathbf{u}_1 and \mathbf{u}_2 , we have that the nonsingular strain condition

$$\forall \mathbf{x} \quad \det(\varepsilon(\mathbf{u}_i(\mathbf{x}))) \neq 0 \quad \text{for one } i = 1, 2, \quad (5.10)$$

holds, we can infer from [136, Thm.2+Cor.4] that for all $\delta\mu \in E$, we have that

$$\|\delta\mu\|_{H^{l+1}} \leq K_\mu \|(\delta\mathbf{u}_1, \delta\mathbf{u}_2)\|_{H^{l+2}}, \quad (5.11)$$

holds. This, together with boundedness of $\delta\varphi = (\delta\mathbf{u}_1, \delta\mathbf{u}_2)$ implies that $\delta\varphi$ is a Banach space isomorphism between $E = H^{l+1}(\Omega)$ and $F = (H^{l+2}(\Omega))^3$.

The constant K_μ in (5.11) comes from a regularity estimate in [126], which uses the functional analytic method of the proof in [5], and it does not depend on $\delta\mu$. We also assume the dependence of K from μ continuous, at least for bounded parameters. Given the regularity results in [51, Ch.8], it can be expected that it is independent of μ , but only depends on the bounds a and b in (5.6).

5.3.1. General approach: implicit function theorem

We now exploit the stability and injectivity results of [136] with the implicit function theorem.

Implicit function theorem for Banach spaces

The implicit function theorem allows to deduce local invertability of the nonlinear operator from continuous and invertible linearizations of a nonlinear operator in a neighborhood of a point. The precise formulation can for instance be found in [73]:

5.3. Stability of the linearization and implications of the implicit function theorem

Theorem 8. *Let E, F be Banach spaces, $C \subset E$ an open subset and $\varphi : C \rightarrow F$ be a differentiable mapping. Let $\delta\varphi : E \rightarrow F$ be its Fréchet derivative corresponding to a variable μ , and let $\delta\varphi$ be continuous as well as a Banach space isomorphism between E and F at a particular point μ_0 (i.e., continuously invertible there). Then the mapping φ can be uniquely and stably inverted locally with respect to μ .*

The application of the implicit function theorem

We now consider the forward map φ . Suppose that we have a reference state $\mu \in C$, and corresponding measurements $\varphi(\mu) = (\mathbf{u}_1, \mathbf{u}_2)$ given, and that (5.10) holds for all $\varphi(\mu)$ in a neighborhood $V \subset C$.

As mentioned in (5.11), we have shown in [136] that $\|\delta\mu\|_{l+1} \leq K\|(\delta\mathbf{u}_1, \delta\mathbf{u}_2)\|_{l+2}$. Applying additionally Theorem 14 in Appendix 5.8.1 yields the desired inequality for Banach space isomorphism,

$$\exists C \in \forall \delta\mu \in H^{l+1}(\Omega) : \quad \frac{1}{C}\|\delta\mu\|_{H^{l+1}} \leq \|(\delta\mathbf{u}_1, \delta\mathbf{u}_2)\|_{H^{l+2}} \leq C\|\delta\mu\|_{H^{l+1}}.$$

We conclude that due to the implicit function theorem, there exist neighborhoods $U \subset H^{l+1}(\Omega), V \subset (H^{l+2}(\Omega))^6$ and a unique solution function g (being also continuously differentiable)

$$g : V \rightarrow U$$

such that $\mathcal{V}(\mu, \mathbf{u}_1, \mathbf{u}_2) = 0$ for $(\mathbf{u}_1, \mathbf{u}_2) \in V$ precisely when $\mu = g(\mathbf{u}_1, \mathbf{u}_2)$.

Therefore, we get:

Theorem 9. *For two measurements satisfying (5.10), the elasticity problem $\varphi(\mu) = (\mathbf{u}_1, \mathbf{u}_2)$ is locally stably invertible in a neighborhood V around μ .*

Remark 4. Following the proof of the implicit function theorem, one could infer bounds on the neighborhood V . The implicit function theorem, though, can only yield a statement for values $(\mathbf{u}_1, \mathbf{u}_2)$ in the range of φ (see also [34, p.11] for this discussion). In practice, one is confronted with noisy data $(\mathbf{u}_1^\delta, \mathbf{u}_2^\delta)$ outside the range, and in all methods of quantitative elastography, regularization has been necessary to deal with the problem of measurement noise [40]. We therefore do not develop the implicit function approach further. Given the need for regularization in the actual solution of the problem, we consider two methods based on least-squares minimization: One is the approach for Tikhonov regularization, using the theory [34]. This is the subject of Section 5.4. The other is the Levenberg-Marquardt regularization, using the tangential cone condition. This is treated in Section 5.5.

5.4. Convergence for Tikhonov regularization: Geometric theory

In this section, we develop the tools of the geometric theory [34, 35]. We first give the quantities needed in the theory. Then we give the conditions the theory and its statements. We treat the application on the elasticity problem using the theory [136] in the spaces $\varphi : E \rightarrow F$ in (5.4). In actual experiments, the measured data will lie in L^2 . For the numerical realization, therefore, this mapping will be combined with the embedding $F \hookrightarrow L^2$ in Section 5.6.

Specification of auxiliary quantities for the geometric theory

For given $\mu_0, \mu_1 \in E$, we consider the one-dimensional path

$$t \mapsto \mathbf{P}(t) := \varphi(\mu_0 + t(\mu_1 - \mu_0)), \quad (5.12)$$

together with its derivatives $\mathbf{P}'(t) := \mathbf{V}(t)$ and $\mathbf{P}''(t) := \mathbf{A}(t)$.

Well-posedness according to geometric theory

First some definitions for the parameter set C : The diameter of C :

$$\text{diam } C := \sup_{x, y \in C} \|x - y\|_E \quad (5.13)$$

and the radius:

$$\text{rad}_{x_0} C := \sup_{x \in C} \|x - x_0\|_E. \quad (5.14)$$

We now investigate regularization of the least squares problem for the forward problem in (5.5). The essential conditions in the geometric theory [34, 35] are that there exist numbers $\alpha, R \in \mathbb{R}$ such that for all $\mu_0, \mu_1 \in C$ and for all $t \in \mathbb{R}$, we have

$$\|\mathbf{V}(t)\|_F \leq \alpha \|\mu_1 - \mu_0\|_E \quad (5.15)$$

$$\|\mathbf{A}(t)\|_F \leq \frac{1}{R} \|\mathbf{V}(t)\|_F^2. \quad (5.16)$$

Once this is assured, one additionally scales the diameter of the set C in such that one has

$$\alpha \text{diam } C \leq \pi R. \quad (5.17)$$

This condition can be fulfilled by providing more apriori information on the solution μ , i.e., tighter bounds on the allowed parameters in the minimization in (5.6).

Theorem 10. *Let conditions (5.15)-(5.17) be satisfied. Take φ_0 as attainable measurement datum, and μ_0 an apriori choice for the recovery of the material parameter. Let μ^\dagger be a minimal-norm solution:*

$$\mu^\dagger = \arg\min_E \{\|\mu - \mu_0\|_E : \varphi(\mu) = \varphi_0\}$$

5.4. Convergence for Tikhonov regularization: Geometric theory

Then there exists a neighborhood W of φ_0 , such that for all $\varphi^R \in W$, the Tikhonov regularization

$$\mu_\gamma^R := \operatorname{argmin}_{\mu \in C} \|\varphi(\mu) - \varphi^R\|_F^2 + \gamma \|\mu - \mu_0\|_E^2 \quad (5.18)$$

is well-posed for sufficiently small $\gamma \rightarrow 0$. In particular:

- There exists a solution $\mu_\gamma^R \in C \subset E$ in (5.18).
- The solution of (5.18) is unique.
- There is only one extremal point in C for the functional (5.18).

Moreover, for φ with injective linearization $\delta\varphi$ and for a sequence $R/\gamma \rightarrow 0$, one has the convergence property

$$\mu_\gamma^R \rightarrow \mu^\dagger \quad \text{for} \quad \gamma \rightarrow 0. \quad (5.19)$$

With R as in (5.16), the neighborhood W can be chosen as $\{\varphi^R : \|\varphi^R - \varphi_0\| < R\}$.

For a linear mapping φ , (5.18) would be well-posed for every \mathbf{u} [44]. The theorem essentially gives conditions (5.15), (5.16) on the nonlinearity which guarantee that the Tikhonov functional still possesses almost the same well-posedness properties as in the linear case.¹

For those φ which lie outside the neighborhood W , one has a minimum amount of regularization which one should apply [34, Proposition 5.1.16]:

Proposition 5. *Let \mathbf{A} in (5.12) satisfy $\|\mathbf{A}(t)\|_F \leq \beta \|\mu_1 - \mu_0\|_E^2$. Then there exists a minimum*

$$\gamma_{\min} := \beta \max \left\{ \operatorname{rad}_{\mu_0} C, \frac{2}{\pi} \operatorname{diam} C \right\} \quad (5.20)$$

with diam and rad as in (5.13), (5.14) such that the Tikhonov functional (5.18) is well-posed for $\gamma \geq \gamma_{\min}$ on the neighborhood $\{\varphi^{R_\gamma} \in C : \|\varphi^{R_\gamma} - \varphi_0\| < d_\gamma\}$, with $d_\gamma = \gamma \sqrt{\frac{\gamma^2}{\beta^2} - \operatorname{rad}_{\mu_0}^2} C$.

Together, Theorem 10 and Proposition 5 imply that the problem (5.18) is a well-posed and convergent regularization method for φ and $\gamma \in (0, \gamma'] \cup [\gamma_{\min}, \infty)$. For a sufficiently high level of regularization, thus, the measurement noise can be successfully compensated by the Tikhonov regularization. For sufficiently small levels of measurement noise, the Tikhonov regularization gives a result arbitrarily close to the minimal-norm solution μ^\dagger .

¹ The details of the proof of Theorem 10 can be found in [35], or in [34], Theorem 5.15(1-2); the condition (5.55) in [34] follows for injective $\delta\varphi$ from Def. 4.3.1, Lemma 5.1.12 and Lemma 5.1.13.

5. Convergent regularization methods for quantitative elastography

The velocity and acceleration in elasticity

Recall the quantities $\mathbf{P}(t)$, $\mathbf{V}(t)$ and $\mathbf{A}(t)$ which are defined in (5.12).

Lemma 3. *a) In the case of our model (5.1), the functions $\mathbf{P}(t) = (\mathbf{P}_1(t), \mathbf{P}_2(t))$, $\mathbf{V}(t) = (\mathbf{V}_1(t), \mathbf{V}_2(t))$ and $\mathbf{A}(t) = (\mathbf{A}_1(t), \mathbf{A}_2(t))$ are characterized by the following equations:*

$$\nabla \cdot [(\mu_0 + t(\mu_1 - \mu_0)) \varepsilon(\mathbf{P}_i(t))] = \mathbf{f}_i \quad i = 1, 2 \quad (5.21)$$

$$\nabla \cdot [(\mu_0 + t(\mu_1 - \mu_0)) \varepsilon(\mathbf{V}_i(t))] = -\nabla \cdot [(\mu_1 - \mu_0) \varepsilon(\mathbf{P}_i(t))] \quad i = 1, 2 \quad (5.22)$$

$$\nabla \cdot [(\mu_0 + t(\mu_1 - \mu_0)) \varepsilon(\mathbf{A}_i(t))] = -2 \nabla \cdot [(\mu_1 - \mu_0) \varepsilon(\mathbf{V}_i(t))] \quad i = 1, 2, \quad (5.23)$$

together with boundary conditions (5.2) for $\mathbf{P}_i(t)$ and homogeneous boundary conditions for $\mathbf{V}(t)$ and $\mathbf{A}(t)$, respectively.

b) Furthermore, one has that $\mathbf{V}_i(t)$ is equal to the linearization $\delta \mathbf{u}_i[\mu](\delta \mu)$, which is the solution of equation (5.7), with the reference state

$$\mu = \mu_0 + t(\mu_1 - \mu_0) \quad (5.24)$$

and the increment $\delta \mu = \mu_1 - \mu_0$.

Proof. a) The proof is by combining the definition of φ in (5.12) and formal differentiation of the model equation (5.1).

b) Let $\mathbf{u}_i = \mathbf{u}_i(\mu)$ satisfy the model (5.1) for given μ and $\mathbf{f} = \mathbf{f}_i$. Using the reference state μ in (5.24) and the increment $\delta \mu$, we have $\mathbf{u} = \mathbf{P}_i(t)$. Furthermore, with these choices, equation (5.7) reduces to equation (5.22). Therefore $\delta \mathbf{u}_i[\mu](\delta \mu) = \mathbf{V}_i(t)$. \square

Velocity and acceleration estimates in elasticity

Lemma 4. *Let $C' \subset C \subset H^{l+1}(\Omega)$ be compact with respect to the H^{l+1} -topology, where C is as defined in (5.6), satisfying*

$$\mu \in C' \implies \mathbf{u}_i \text{ in (5.1), (5.2) satisfy (5.10)} \quad (5.25)$$

The conditions (5.15) and (5.16) for $\mathbf{V}(t)$ and $\mathbf{A}(t)$ hold with $F = (H^{l+2}(\Omega))^2$.

Remark 5. To show the qualitative condition on the displacements \mathbf{u}_i formally is an open problem. An informal argumentation is given in [20, 3], see also [136].

Proof. Choose t, μ_0, μ_1 and take μ as in (5.24). For proving conditions (5.15) and (5.16), we adopt the following procedure: We first apply the regularity theory in 5.8.1. Then, we apply the linear stability estimates in the article [136]. To get a uniform estimate, the compactness of C is used.

Consider first the equations for $\mathbf{P}(t)$, $\mathbf{V}(t)$ and $\mathbf{A}(t)$ in Lemma 3. Consider first equation (5.21). Upon application of the regularity theory 5.8.1, we obtain

$$\|\mathbf{P}(t)\|_{l+2} \leq B_\mu \|\mathbf{f}\|_l \leq C_\mu \|\mathbf{f}\|_{l+1}.$$

5.4. Convergence for Tikhonov regularization: Geometric theory

Let us now turn to equation (5.22). Using regularity theory again, we have

$$\|\mathbf{V}_i(t)\|_{H^{l+2}} \leq D_\mu \|\nabla \cdot [(\mu_1 - \mu_0) \varepsilon(\mathbf{P}_i(t))]\|_{H^l}. \quad (5.26)$$

We invoke the Banach algebra property of $H^l(\Omega)$, and therefore can estimate the H^l -norm of the right-hand side as follows:

$$\begin{aligned} \|\nabla \cdot [(\mu_1 - \mu_0) \varepsilon(\mathbf{P}_i(t))]\|_{H^l} &= \|\delta\mu \nabla \cdot [\varepsilon(\mathbf{P}_i(t))] + \nabla \delta\mu : \varepsilon(\mathbf{P}_i(t))\|_{H^l} \\ &\leq \|\delta\mu\|_{H^l} \|\nabla \cdot [\varepsilon(\mathbf{P}_i(t))]\|_{H^l} + \|\nabla \delta\mu\|_{H^l} \|\varepsilon(\mathbf{P}_i(t))\|_{H^l} \\ &\leq 4\|\delta\mu\|_{H^{l+1}} \|\mathbf{P}_i(t)\|_{H^{l+2}} \quad i = 1, 2. \end{aligned} \quad (5.27)$$

Taking the inequalities (5.26) and (5.27) together, we obtain

$$\|\mathbf{V}_i(t)\|_{H^{l+2}} \leq D_\mu \|\delta\mu\|_{H^{l+1}} \|\mathbf{P}_i(t)\|_{H^{l+2}} \quad \text{for } i = 1, 2.$$

Written with the vector notation, we have the estimate

$$\|\mathbf{V}(t)\|_E \leq D_\mu \|\delta\mu\|_{H^{l+1}} \|\mathbf{P}(t)\|_F. \quad (5.28)$$

The same argument can be applied to $\mathbf{A}(t)$.

In summary, we obtain for each t :

$$\|\mathbf{P}(t)\|_F \leq B_\mu \|\mathbf{f}\|_{l+1} \quad (5.29)$$

$$\|\mathbf{V}(t)\|_F \leq 4D_\mu \|\mu_1 - \mu_0\|_E \|\mathbf{P}(t)\|_F \quad (5.30)$$

$$\|\mathbf{A}(t)\|_F \leq 4G_\mu \|\mu_1 - \mu_0\|_E \|\mathbf{V}(t)\|_F. \quad (5.31)$$

Insert now estimate (5.29) into (5.30). Assuming continuous dependence of the constants on μ , we use compactness of C' and define

$$\alpha := \sup_{\mu \in C'} B_\mu.$$

Using the maximal property of α , we obtain inequality (5.15).

Next we apply the stability theory for the linearized problem [136]. Consider the reference state μ as defined in (5.24). Then we calculate for $\delta\mu \in H^{l+1}(\Omega)$ the quantity $\delta\mathbf{u}_i = \delta\mathbf{u}_i^\mu(\delta\mu)$, which, by Lemma 3, equals $\mathbf{V}_i(t)$. Therefore the estimate (5.11) reads:

$$\|\mu_1 - \mu_0\|_{l+1} \leq K_\mu \|\mathbf{V}(t)\|_{l+2}. \quad (5.32)$$

Inserting this estimate into (5.32), we obtain that

$$\|\mathbf{A}(t)\|_{l+2} \leq G_\mu K_\mu \|\mathbf{V}(t)\|_{l+2}^2.$$

Then define

$$R := \frac{1}{\sup_{\mu \in C'} G_\mu K_\mu}.$$

Then an inequality of form (5.16) results. \square

5. Convergent regularization methods for quantitative elastography

- Remark 6.*
1. If we assume that the constants B_μ , D_μ and G_μ depend only on the upper and lower bounds in (5.5), then the assumption of compactness of C' in (5.25) be dropped.
 2. The constant α can be interpreted as sensitivity of the problem, see [34, Ch.4].
 3. The constant R can be interpreted as lower bound of the radius of curvature of any curve in the range $\varphi(C')$. Elements in the neighborhood $\{\varphi^R : \|\varphi^R - \varphi_0\| < R\}$ can be uniquely and stably projected onto $\varphi(C')$, which mimicks the favourable projection properties of convex sets in the case of linear problems [34, 4.1-4.2].

Application of geometric theory to elasticity problem

We now collect the results of Lemma 3 and Lemma 4, and consider that $\delta\varphi$ is injective (see Section 5.3). Applying the geometric theory in Theorem 10, we get

Theorem 11. *Let C' be the parameter set in Lemma 4, and let $\varphi^R \in \{\varphi^R \in C' : \|\varphi^R - \varphi_0\| < R\}$. Consider the functional defined in (5.33),*

$$\mu_\gamma^R := \operatorname{argmin}_{\mu \in C} \|\varphi(\mu) - \varphi^R\|_F^2 + \gamma \|\mu - \mu_0\|_E^2. \quad (5.33)$$

Then this problem has a well-defined solution for sufficiently small γ , with φ specified in equation (5.3) and E, F specified in the lemmas. One has that $\mu_\gamma^R \rightarrow \mu^\dagger$ for $\gamma \rightarrow 0$ provided $R/\gamma \rightarrow 0$.

As stated before, Problem (5.33) is also well-posed for sufficiently high values of γ . Proposition 5 assures that also for data which satisfy the condition $\operatorname{dist}(\varphi(C'), \varphi^R) \geq R$, one can choose a minimal γ_{\min} in (5.20) for an appropriate regularization parameter. (Due to (5.15), (5.16), β in the proposition can be chosen as α/R). This result actually justifies the use of choosing the regularization parameter as high as to compensate for measurement noise.

5.5. The Levenberg Marquardt iteration and its convergence properties

The Levenberg-Marquardt iteration (see [64]) is defined as

$$\mu_{k+1} - \mu_k = (d\varphi^* d\varphi + \gamma_k \mathbf{Id})^{-1} d\varphi^* (\varphi^\delta - \varphi(\mu)). \quad (5.34)$$

Here, $\gamma_k > 0$ are regularization parameters, and the linearization $d\varphi$ and the adjoint $d\varphi^*$ are as in (5.9) and (5.50). Let φ_0 be attainable measurement data in $F = (H^{l+2}(\Omega))^n$. Then this iterative regularization method serves to approximate a solution of the equation

$$\varphi(\mu^\delta) = \varphi^\delta,$$

5.5. The Levenberg Marquardt iteration and its convergence properties

where φ^δ are noisy measurement data in $W = \{\varphi^\delta : \|\varphi^\delta - \varphi_0\| < \delta\}$.

In the theoretical analysis, we prove a condition for convergence of this algorithm due to [59] (see also [64, Section 4.1]). For better readability, we use (5.9) and write $\delta\varphi = (\delta\mathbf{u}_1, \delta\mathbf{u}_2)$. We assume that we work in the subset C' described in (5.25).

Proposition 6. *Let \mathbf{R} be the first order Taylor remainder of the forward mapping φ in (5.3), i.e.,*

$$\mathbf{R}[\mu](\delta\mu) := \varphi(\mu + \delta\mu) - \varphi(\mu) - (\delta\mathbf{u}_1, \delta\mathbf{u}_2) \quad (5.35)$$

Then there exists $D' \in \mathbb{R}$ and a set V such that for all $\mu_1, \mu_0 \in V \subset C'$, the tangential cone condition

$$\|\mathbf{R}[\mu_0](\mu_1 - \mu_0)\|_F \leq D' \|\mu_1 - \mu_0\|_E \|\varphi(\mu_1) - \varphi(\mu_0)\|_F \quad (5.36)$$

is satisfied.

Proof. The outline of the proof is as follows: We start with the estimates for the Taylor remainder in (5.65). Then we use the linear stability theory (5.11) to obtain a Lipschitz estimate for the nonlinear problem φ . From this the tangential cone condition (5.36) follows.

The forward map with one measurement has been analyzed in the appendix 5.8.2, and Fréchet differentiability was obtained in (5.65). This result straightforwardly generalizes to differentiability of the forward map φ with two measurements. Therefore, we have for \mathbf{R} in (5.35)

$$\exists C \exists W : \forall \delta\mu \in W \quad \|\mathbf{R}[\mu](\delta\mu)\|_F \leq B \|\delta\mu\|_E^2. \quad (5.37)$$

Using the definition (5.35) and the reverse triangle inequality, we obtain

$$\|(\delta\mathbf{u}_1, \delta\mathbf{u}_2)\|_F - \|\varphi(\mu + \delta\mu) - \varphi(\mu)\|_F \leq B \|\delta\mu\|_E^2,$$

and hence we can estimate

$$\|(\delta\mathbf{u}_1, \delta\mathbf{u}_2)\|_F - B \|\delta\mu\|_E^2 \leq \|\varphi(\mu + \delta\mu) - \varphi(\mu)\|_F. \quad (5.38)$$

We want to show that $\|\delta\mu\|_E$ is a lower bound for the left hand side of (5.38). For this purpose, we now turn to the linear stability theory in (5.11): We choose $G \in \mathbb{R}$ such that

$$G \|\delta\mu\|_E \leq \|(\delta\mathbf{u}_1, \delta\mathbf{u}_2)\|_F. \quad (5.39)$$

Let $\delta\mu$ be in the neighborhood $W \cap B_{G-D}(\mu)$, where $D < \frac{G}{B}$ has been chosen.

For such $\delta\mu$, one has that

$$\begin{aligned} \|\delta\mu\|_E^2 &\leq \left(\frac{G}{B} - D\right) \|\delta\mu\|_E && \text{or, equivalently,} \\ B \|\delta\mu\|_E^2 &\leq G \|\delta\mu\|_E - BD \|\delta\mu\|_E. \end{aligned}$$

5. Convergent regularization methods for quantitative elastography

Employing (5.39), it then follows that

$$B\|\delta\mu\|_E^2 \leq \|(\delta\mathbf{u}_1, \delta\mathbf{u}_2)\|_F - BD\|\delta\mu\|_E,$$

and hence we have the estimate

$$BD\|\delta\mu\|_E \leq \|(\delta\mathbf{u}_1, \delta\mathbf{u}_2)\|_F - B\|\delta\mu\|_E^2. \quad (5.40)$$

Taking now into account both estimates (5.38) and (5.40), we obtain for $H = \frac{1}{BD}$

$$\|\delta\mu\|_E \leq H\|\varphi(\mu + \delta\mu) - \varphi(\mu)\|_F. \quad (5.41)$$

This is the Lipschitz continuity for the nonlinear problem φ .

From the estimate on the Taylor remainder (5.37), it then follows from Lipschitz continuity (5.41) that for $D' = \frac{1}{D}$ and $\mu \in E$,

$$\|\mathbf{R}[\mu](\delta\mu)\|_F \leq D'\|\delta\mu\|_E \|\varphi(\mu + \delta\mu) - \varphi(\mu)\|_F.$$

holds. Assuming continuous dependence of the constants on μ , we obtain the existence of a neighborhood, such that (5.36) holds. \square

Hanke [59] suggests to choose the regularization parameters γ_k in (5.34) a posteriori according to the discrepancy principle

$$\|\varphi^\delta - \varphi(\mu_k) - \delta\varphi[\mu_k](\mu_{k+1}(\gamma_k) - \mu_k)\| = q\|\varphi^\delta - \varphi(\mu_k)\| \quad (5.42)$$

for some $0 < q < 1$. With this choice of parameters, one has (see also [64, Thm. 4.2]) that the bounds on the Fréchet derivative in (5.8.2) and Proposition 6 imply

Theorem 12. *Let $0 < q < 1$ and let (5.1) be solvable in $B_\rho(\mu_0)$. The Levenberg Marquardt iterates (5.34) with exact data $\varphi^\delta = \varphi$, and a starting value satisfying $\|\mu_0 - \mu^\dagger\| < q/B$ and the regularization parameters γ_k determined as above converge monotonically towards a solution of $\varphi(\mu) = \varphi$ as $k \rightarrow \infty$.*

For noisy data with known noiselevel $\delta > 0$, one has to early stop the iteration in order not to accumulate artefacts. This, according to [59], can be done using a discrepancy principle again as a stopping criterion, i.e., one stops the iteration of μ_k^δ after step k^* , when for the residual one has

$$\|\varphi^\delta - \varphi(\mu_{k^*}^\delta)\| \leq \tau\delta \quad (5.43)$$

for the first time. Then one has the following convergence property:

Theorem 13. *Let the assumptions of Theorem 12 hold, and let $\|\mu_0 - \mu^\dagger\|$ be sufficiently small. Then the discrepancy principle (5.43) with $\tau > 1/q$ terminates the iteration after finitely many steps. If $\delta \rightarrow 0$, the iterates $\mu_{k^*}^\delta$ converge to a solution of $\varphi(\mu) = \varphi$.*

5.5.1. Remarks

- Choosing the set parameter set C' larger such that (5.10) is not satisfied at certain points loses the ellipticity property shown in [136]. For particular measurement data, this could potentially result in edges or singularities propagating and artifact production, though there is research on what can be retrieved when the ellipticity property is only lost at isolated points (see, e.g. [21]).
- A Lipschitz estimate for the nonlinear problem in incompressible quasi-static elastography, such as (5.41), has been provided by [8] as well in the context of a similar approach using the overdetermined theory [126]. The difference in that approach is that the overdetermined system is obtained without linearization, but directly for μ . In that proof, it is assumed that that the difference $\mu_1 - \mu_0$ (in our notation) lies in a finite-dimensional kernel K , and that an ellipticity condition for $n = 3$ is that

$$\exists C : \sum_{i=1}^2 |\varepsilon((\mathbf{u}_i(x)) * \boldsymbol{\xi} \times \boldsymbol{\xi})| \geq C |\boldsymbol{\xi}|^2,$$

using two measurements. For dimensions $n = 2$, apart from $\mu_1 - \mu_0 \perp K$, one can have resort to a condition $\det(\varepsilon(\mathbf{u}_1)) \neq 0$, which is (5.10) with $i = 1$. Then, in [8], the resulting Lipschitz stability theorem in H^4 is used to obtain convergence of the Landweber iteration, employing [13].

Note that for every numerical realization of the problem, one cannot expect to find parameters in $E = H^{l+1}(\Omega)$ from data with measurements in L^2 (which would be ill-posed as $l + 1$ differentiations). We therefore embed $F \hookrightarrow L^2$. This amounts to smoothing the data before it can enter the inversion process, and, in the terminology of [34], is also referred as *state-space regularization*. This method has been previously employed in other hybrid imaging problems for recovery of the conductivity, see e.g. [23] and [34, 5.3.1].

5.6. Minimization process

5.6.1. Setting of minimization

In the result on (5.33) in section 5.4, we considered for $\varphi : E \rightarrow F$ with source terms $(\mathbf{f}_1, \mathbf{f}_2)$ and the measured displacements $\boldsymbol{\varphi}^\delta = (\mathbf{u}_1^\delta, \mathbf{u}_2^\delta)$, which correspond to true displacement fields $(\mathbf{u}_1, \mathbf{u}_2)$ in (5.1) up to a noise level δ .

The general least-squares minimization problem aims to find the minimum

$$\operatorname{argmin}_{\mu \in C} \|\Psi(\mu)\|_{L^2}, \quad (5.44)$$

where

$$\Psi(\mu) := \boldsymbol{\varphi}^\delta - i \circ \varphi(\mu) \in L^2, \quad (5.45)$$

5. Convergent regularization methods for quantitative elastography

with $i : H^{l+2} \hookrightarrow L^2$ is the embedding into L^2 .

If we add a regularization term to the functional in (5.44), then Tikhonov regularization results:

$$\operatorname{argmin}_{\mu \in C} \|\varphi(\mu) - \varphi^\delta\|_{L^2}^2 + \gamma \|\mu - \mu_0\|_E^2. \quad (5.46)$$

Then we can consider two measurements $\mathbf{U} = \{(\mathbf{f}_1, \mathbf{u}_1^\delta), (\mathbf{f}_2, \mathbf{u}_2^\delta)\}$ and the following operator $\Psi_{\gamma, \mathbf{U}} : E \rightarrow L^2 \times E$, mapping

$$\Psi_{\gamma, \mathbf{U}} : \quad \mu \mapsto \begin{pmatrix} (\mathbf{u}_1^\delta, \mathbf{u}_2^\delta) - \varphi(\mu) \\ \sqrt{\gamma}(\mu - \mu_0) \end{pmatrix}.$$

Minimizing (5.46) is equivalent with minimizing the least-squares functional

$$\operatorname{argmin}_{\mu \in C} \|\Psi_{\gamma, \mathbf{U}}(\mu)\|_{L^2 \times E}^2 \quad (5.47)$$

We can either employ minimization algorithms with respect to (5.44), or to the regularized version to minimize (5.47). This is true for a steepest descent method, for a Landweber iteration, or a Levenberg Marquardt iteration.

5.6.2. Numerical inversions to recover shear modulus

We first explain the forward simulation and how the gradient is obtained.

Forward simulations

For the forward simulations of (5.1), we use the PS2 Finite Difference scheme exposed in the article [138] on a regular grid. We therefore use (compare [138, eq. (A2)]) the following discretization of the primitive terms in the model (5.1):

$$\begin{aligned} \frac{\partial}{\partial x} \left(\mu(x) \frac{\partial}{\partial x} f(x) \right) &\approx \frac{1}{h^2} [\mu_W f_{i-1} + \mu_E f_{i+1} - (\mu_W + \mu_E) f_i] \\ \frac{\partial}{\partial y} \left(\mu(x) \frac{\partial}{\partial x} f(x, y) \right) &\approx \frac{1}{4h^2} [\mu_N f_{i+1, j+1} - \mu_N f_{i-1, j+1} \\ &\quad + (\mu_N - \mu_S) f_{i+1, j} + (\mu_S - \mu_N) f_{i-1, j} \\ &\quad - \mu_S f_{i+1, j-1} + \mu_S f_{i-1, j-1}] \end{aligned}$$

Here, $\mu_N = \frac{1}{2}(\mu_{i, j} + \mu_{i, j+1})$, and similar for the other parameters. Shown is the discretization of the first equation in (5.1); the second equation is obtained by similar means (see [138]).

We used boundary data like in [20, (50)],

$$\begin{aligned} \mathbf{g}_1(\mathbf{x}) &= 1 + (\mathbf{x} \cdot \mathbf{e}_2) \mathbf{e}_1 + (\mathbf{x} \cdot \mathbf{e}_1) \mathbf{e}_2 \\ \mathbf{g}_2(\mathbf{x}) &= 1 + (\mathbf{x} \cdot \mathbf{e}_1) \mathbf{e}_1 + (\mathbf{x} \cdot \mathbf{e}_2) \mathbf{e}_2 \end{aligned}$$

These satisfy the invertibility condition in [20], which is a specialization of (5.10) (see also [136, 4.2]).

The reconstructions shown here use data from a 100x100 grid. The inversion is carried out on a 90x90 grid in Figure 5.4 and on a 60x60 grid in Table 5.1.

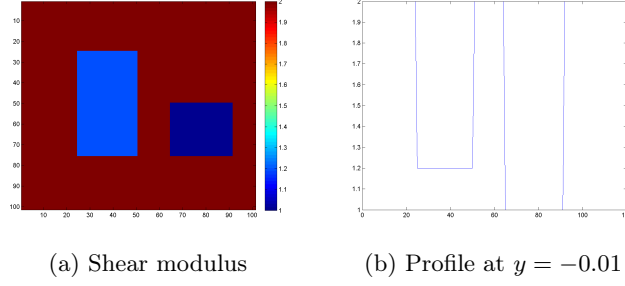


Figure 5.1.: Original shear modulus

Data and noise

The original shear modulus is shown in Figure 5.1: The measurement data are shown in Figure 5.2. Reconstructions from noise-free data are shown in (5.3). In Figure 5.4, noisy data with 1% noise are used. In Table 5.1, different noiselevels have been compared.

Inversions

Optimization

Landweber iterations for the Tikhonov functional (5.47) consist in the iteration prescription

$$\mu_{k+1} = \mu_k + \kappa \Psi^*(\varphi^\delta - \varphi(\mu)) \quad (5.48)$$

with Ψ as in (5.45), which is actually the steepest descent method with constant stepsize. We compare this algorithm to the Levenberg Marquardt iteration from (5.34)

$$\mu_{k+1} = \mu_k + (d\varphi^* d\varphi + \gamma_k \mathbf{Id})^{-1} d\varphi^*(\varphi^\delta - \varphi(\mu)) \quad (5.49)$$

In Section 5.5, we described the results of [59], which use in their idealized setting the discrepancy principles for the choice of the regularization parameter (5.42). It would, of course, be possible to determine γ_k according to these a posteriori choices. Though it is important for the theoretical analysis that such choices exist, the numerical determination would involve considerable computational effort. However, in practice, we got already satisfactory results with apriori parameters chosen ad hoc.

A minimal amount of line search has been used in order to take steps with a suitable order of magnitude. We note that according to the geometric theory, a more sophisticated line search involving the curvature of the forward problem is possible [34, 3.9].

To describe the implementation, note first that the adjoint $(\delta\varphi)^*$ acting on \mathbf{z} is given by

$$(\delta\varphi)^* \mathbf{z} = (\delta\mathbf{u}_1)^* \mathbf{z} + (\delta\mathbf{u}_2)^* \mathbf{z}, \quad (5.50)$$

5. Convergent regularization methods for quantitative elastography

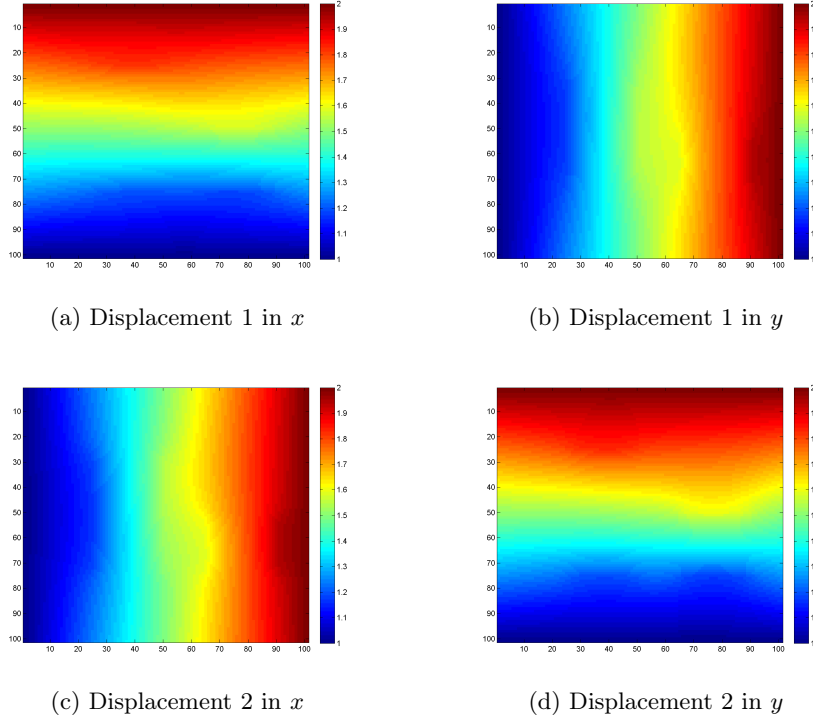


Figure 5.2.: Data used for the reconstructions with two measurements

with $(\delta \mathbf{u}_j)^*$ as in (5.66), i.e. $(\delta \mathbf{u}_j)^* \mathbf{z} = i^*(\varepsilon(\mathbf{u}_j) : \varepsilon(\mathbf{V}\mathbf{z}))$ for $j = 1, 2$.

Whereas theoretically, the state-space regularization $F \hookrightarrow L^2$ could be used in our setting, the approximation $i : H^1 \hookrightarrow L^2$ was used in [23] for a similar problem and shown to be already responsible for most of the output of the state-space regularization. In view of the runtime, it is therefore efficient to use H^1 -adjoints as an approximation. Here, one takes the scalar product

$$\langle x, y \rangle_{H^1(\Omega)} = \langle x, y \rangle_{L^2(\Omega)} + \beta \langle \nabla x, \nabla y \rangle_{L^2(\Omega)},$$

where $\beta > 0$ is a parameter controlling the smoothing in the embedding. As shown in [23, 3.1], for $w \in L^2(\Omega)$, the embedded (and smoothed) version i^*w is given by the solution of the following Neumann problem on Ω :

$$\begin{aligned} (\text{Id} - \beta^2 \Delta) i^* w &= w \\ \partial_\nu i^* w &= 0 \quad \text{on } \partial\Omega \end{aligned} \tag{5.51}$$

We can therefore compare the results for L^2 adjoints (which correspond to $i = \text{Id}$, and the H^1 -adjoints (with i given above in (5.51)) in each inversion.

Let us mention at last, that for numerical reasons, we did not implement (5.49) directly; like in [23], we used the sparse representation of the system. Precisely, for the step $\mu_{k+1} - \mu_k =: \tau_k$, we rename $d\varphi^* d\varphi \tau := w_1$. Then calculating w_1 with (5.50), there appear the quantities $\mathbf{y}_1^j := \delta \mathbf{u}_j \tau_k$ and $\mathbf{y}_2^j := \mathbf{V}(\delta \mathbf{u}_j \tau_k)$ for $j = 1, 2$.

5.6. Minimization process

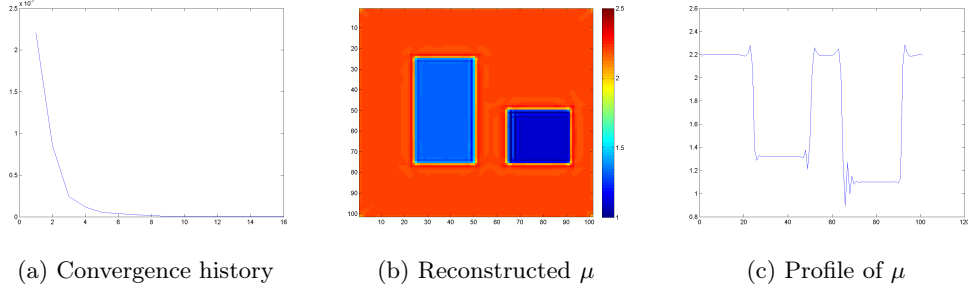


Figure 5.3.: Levenberg Marquardt iteration in H^1 , $\beta = 0.001$, noise-free data, convergence procedure and result with 2 meas.

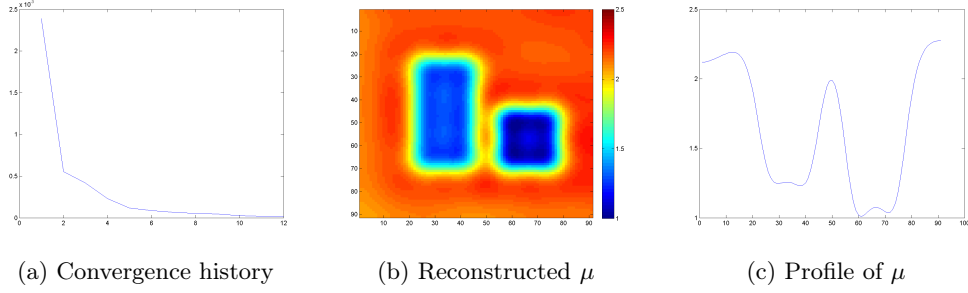


Figure 5.4.: Levenberg Marquardt iteration in H^1 , $\beta = 0.08$; data with 0.1% Gaussian noise, convergence procedure and result with 2 meas.

Instead of (5.49), one solves in each step k of the Levenberg Marquardt iteration the system

$$w_1 + \alpha_k \tau_k = \delta \varphi^*(\varphi^\delta - \varphi(\mu)) \quad (5.52)$$

$$w_1 - \beta^2 \Delta w_1 - w_2 = 0, \quad \partial_\nu w_1|_{\partial\Omega} = 0 \quad (5.53)$$

$$w_2 - \sum_j \varepsilon(\mathbf{u}_j) : \varepsilon(\mathbf{y}_2^j) = 0 \quad (5.54)$$

$$\mathbf{E}_\mu \mathbf{y}_j^1 + \mathbf{E}_\tau \mathbf{u}_j = 0, \quad \mathbf{y}_j^1|_{\partial\Omega} = 0, \quad j = 1, 2 \quad (5.55)$$

$$\mathbf{E}_\mu \mathbf{y}_j^2 - \mathbf{y}_j^1 = 0, \quad \mathbf{y}_j^2|_{\partial\Omega} = 0, \quad j = 1, 2 \quad (5.56)$$

The advantage of the system (5.52)-(5.56) is that it can be represented sparsely, such that all computations could be done on a workstation computer.

The stopping criterion (5.43) was used with $q = 0.46$.

Results and discussion

Two different algorithms have been tested, the Landweber iteration in Table 5.1 and the Levenberg Marquardt iteration in Figure 5.3 and Figure 5.4.

For noise-free data, the Landweber iteration gives satisfactory results, but

5. Convergent regularization methods for quantitative elastography

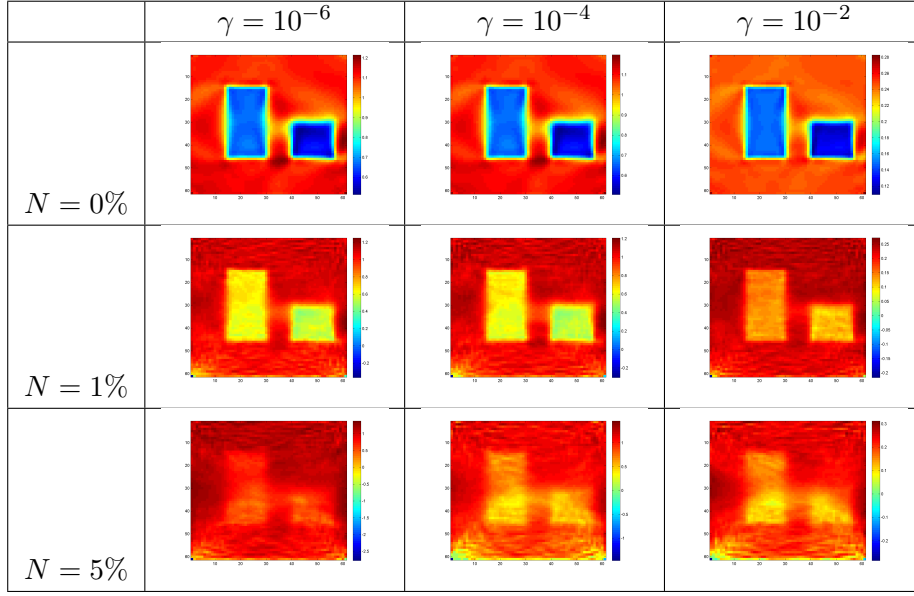


Table 5.1.: Landweber iteration in L^2 with 2 meas.: Relation of noise level N and regularization parameter γ

quicker convergence is obtained by the Levenberg Marquardt iteration. Edges can, of course, be not preserved ideally with the state-space regularization.

For noisy data, the Landweber iteration can be rendered stable by increasing the regularization parameter γ , but the fidelity of the reconstructions is not marked. Though smoothing clearly smears out the edges in the reconstruction, the Levenberg-Marquardt iteration preserves the information in the image better than the Landweber iteration.

As seen from comparison of Figure 5.3 and Figure 5.4, additional measurement noise can be coped with by increasing the value of β for the Levenberg-Marquardt iteration.

Note that, in comparison to the reconstruction in [23], we have to use higher values of β to compensate for the measurement noise. The reason of this seems to lie in the smoothing properties of the forward operator φ . This is reflected also in the different Sobolev orders of the stability estimates. Whereas the forward problem in [23] preserves the Sobolev order and their stability analysis is in $H^l(\Omega) \rightarrow H^l(\Omega)$, the forward problem in elasticity adds one order of differentiation, as we have $\varphi : H^{l+1}(\Omega) \rightarrow (H^{l+2}(\Omega))^2$.

A parameter study using the Levenberg-Marquardt iteration is planned for future work.

5.7. Conclusion

We treated the nonlinear problem of quantitative elastography and applied the results on the ellipticity and stability of the linearized problem. This yielded

two convergence analyses involving regularization: the Tikhonov regularization, which was analyzed with help of the geometric theory of Chavent, and the Levenberg-Marquardt iteration, which was analyzed with a result from Hanke. We obtained convergence results, and illustrated them together with data smoothing as an additional regularization strategy, to recover the shear modulus in compressible elastography with 2 measurements.

Acknowledgements

We thank Wolf Naetar and Peter Elbau for fruitful discussions and acknowledge support from the Austrian Science Fund (FWF) in project S10505-N20.

5.8. Technical results

5.8.1. Proof of a regularity result

Theorem 14. *Consider on the domain Ω the equation $\nabla \cdot (\mu \varepsilon(\mathbf{u})) = \mathbf{f}$ with μ in $H^{l+1}(\Omega)$, $0 < a \leq \|\mu\|_{l+1} < b$ and $\mathbf{u} = 0$ on $\partial\Omega$. Then we have that there exists a constant $C \in \mathbb{R}$ such that*

$$\|\mathbf{u}\|_{H^{l+2}(\Omega)} \leq C \|\mathbf{f}\|_{H^l(\Omega)} \quad (5.57)$$

for all possible $\mathbf{f} \in H^l(\Omega)$.

Proof. By results on elliptic boundary problems [51] (see also [86, Lemma 4.6]), we have that the solution is unique. Using the result on elliptic operators in [126, Thm.1], we obtain that the mapping $\mathbf{u} \mapsto \mathbf{f}$ is a Fredholm operator. Using the uniqueness of the solution, we can invert this mapping. Using the open mapping theorem [37, Ch.III, Thm. 12.1], we obtain continuity, which is equivalent to the inequality in the statement. \square

Lemma 5. *Let the conditions of Theorem 14 hold, and let μ lie additionally in $L^\infty(\Omega)$, and let $0 < \text{ess inf } \mu < \text{ess sup } \mu < \infty$. Then we have*

$$\|\mathbf{u}\|_{H_0^1} \leq C \|\mathbf{f}\|_{L^2},$$

with the constant C depending only on n , Ω , and on the essential bounds on μ .

Proof. Choose the representation of $\nabla \cdot (\mu \varepsilon(\mathbf{u})) = \mathbf{f}$ in the weak form,

$$B[\mathbf{u}, \mathbf{u}] = \int_{\Omega} \mathbf{u} \cdot \mathbf{f} \, d\mathbf{x},$$

with $B[\mathbf{u}, \mathbf{v}] = \int_{\Omega} \varepsilon(\mathbf{u}) : \varepsilon(\mathbf{v}) \, d\mathbf{x}$ (cf., eg. [36, 86]).

Now apply the inequalities of Cauchy-Schwarz, and the inequality of Cauchy with $\varepsilon > 0$, to get

$$B[\mathbf{u}, \mathbf{u}] \leq \varepsilon \int_{\Omega} |\mathbf{u}|^2 \, d\mathbf{x} + \frac{1}{4\varepsilon} \int_{\Omega} |\mathbf{f}|^2 \, d\mathbf{x}. \quad (5.58)$$

5. Convergent regularization methods for quantitative elastography

The term $B[\mathbf{u}, \mathbf{u}]$ on the left-hand side can be estimated from below with $C_3\|\mathbf{u}\|_{H_0^1}$ [86, Lemma 3.6]. The constant C_3 depends only on the essential supremum of μ .

The term $\|\mathbf{u}\|^2 d\mathbf{x}$ on the right-hand side can be estimated from above by Poincaré's inequality [86, Lemma 3.8], as there exists a constant C_P , depending only on Ω and n , such that $\|\mathbf{u}\|_{L^2} \leq C_P\|\mathbf{u}\|_{H_0^1}$.

Together, these estimates transform the inequality (5.58) to

$$C_3\|\mathbf{u}\|_{H_0^1} \leq \varepsilon C_P\|\mathbf{u}\|_{H_0^1} + \frac{1}{4\varepsilon} \int_{\Omega} \|\mathbf{f}\|^2 d\mathbf{x}.$$

An elementary computation then yields that for ε small enough, one has

$$\|\mathbf{u}\|_{H_0^1} \leq \frac{1}{4\varepsilon(C_3 - \varepsilon C_P)} \|\mathbf{f}\|_{L^2}^2.$$

Therefore the statement of the lemma is shown. \square

Proposition 7. *Let the conditions of Theorem 14 and Lemma 5 hold. Then the estimate (5.57) is uniform in μ , i.e., there exists a C , such that for all possible μ , the estimate is valid.*

Proof. We use the principle of uniform boundedness [37, Ch.III, Thm. 14.1]. With this, we have to show that for fixed $\mathbf{f} \in H^l(\Omega)$, the operator $\mathcal{A}_\mu : \mathbf{f} \rightarrow \mathbf{u}$ satisfies

$$\sup_{\mu} \|\mathcal{A}_\mu(\mathbf{f})\| = \sup_{\mu} \|\mathbf{u}\| < \infty.$$

Assume, on the contrary, that $\sup_{\mu} \|\mathbf{u}\| = \infty$. Then there exists a sequence $(\mu_k)_k \in C$ such that $\|\mathbf{u}(\mu_k)\|_{l+2} \rightarrow \infty$.

First observe that with Lemma 5 we have a uniform bound on $\|\mathbf{u}(\mu_k)\|_{H^1}$ by \mathbf{f} . Therefore $\|\mathbf{u}(\mu_k)\|_{q+2} \rightarrow \infty$ is only possible with $q \geq 0$.

Now choose from $0 \leq q \leq l$ the lowest q such that $\|\mathbf{u}(\mu_k)\|_{q+2} \rightarrow \infty$. Then consider the sequence

$$\mathbf{f} = \nabla \cdot (\mu_k \varepsilon(\mathbf{u}(\mu_k))) = \mu_k \nabla \cdot \varepsilon(\mathbf{u}(\mu_k)) + \varepsilon(\mathbf{u}_k) * \nabla \mu_k.$$

As $q \leq l$ is minimal, the second term (which has only one derivative in \mathbf{u}) is bounded in H^q . In the first term, the factor μ_k is bounded from below, but the second diverges. This is a contradiction to $\mathbf{f} \in H^q(\Omega)$.

Therefore $\sup_{\mu} \|\mathcal{A}_\mu(\mathbf{f})\| < \infty$ and we have a uniform estimate in μ . \square

5.8.2. Proof of Fréchet differentiability

We prove differentiability of the mapping $\mu \mapsto \mathbf{u}(\mu)$ for one measurement in the spaces $E \rightarrow F$ using regularity theory for elliptic systems with Sobolev coefficients in [126], i.e. precisely, estimate (5.57). This can then be directly used to obtain differentiability of φ in (5.9), e.g.

First define the operator $\mathbf{E}_\mu : H^{l+2}(\Omega) \times H^{l+2}(\Omega) \rightarrow H^l(\Omega) \times H^l(\Omega)$:

$$\mathbf{E}_\mu \mathbf{u} := \nabla \cdot (\mu \varepsilon(\mathbf{u})) \quad (5.59)$$

With this definition, the equation for the linearization $\delta \mathbf{u}_i$ in (5.7) is written

$$\mathbf{E}_\mu \delta \mathbf{u}(\delta \mu) = -\mathbf{E}_{\delta \mu} \mathbf{u}. \quad (5.60)$$

The corresponding first order Taylor remainder for the displacement \mathbf{u} is denoted

$$\mathbf{Re}[\mu](\delta \mu) := \mathbf{u}(\mu + \delta \mu) - \mathbf{u}(\mu) - \delta \mathbf{u}(\delta \mu). \quad (5.61)$$

As can be shown using (5.60), the Taylor remainder \mathbf{Re} satisfies the equation

$$\mathbf{E}_{\mu+\delta \mu} \mathbf{Re}[\mu](\delta \mu) = -\mathbf{E}_{\delta \mu} \delta \mathbf{u}(\delta \mu) \quad (5.62)$$

with homogeneous boundary data.

We now give two estimates for $\delta \mathbf{u}(\delta \mu)$ and $\mathbf{Re}[\mu](\delta \mu)$, respectively: First, we show that $\delta \mathbf{u} : \delta \mu \mapsto \delta \mathbf{u}(\delta \mu)$ is bounded:

$$\begin{aligned} \|\delta \mathbf{u}(\delta \mu)\|_{l+2} &\leq C \|\nabla \cdot (\delta \mu \varepsilon(\mathbf{u}))\|_l \\ &\leq C \|\delta \mu\|_{l+1} \|\mathbf{u}\|_{l+2} \end{aligned} \quad (5.63)$$

In the inequalities in (5.63), the regularity result (5.57) is used, as well as the Banach algebra property of H^l (see [1, Thm.5.23]).

Secondly, we give an estimate for the Taylor remainder. Using (5.62), (5.57) and the Banach algebra property of $H^l(\Omega)$, we have that

$$\begin{aligned} \|\mathbf{Re}[\mu](\delta \mu)\|_{l+2} &\leq C \|\nabla \cdot (\delta \mu \varepsilon(\delta \mathbf{u}))\|_l \\ &\leq C \|\delta \mu\|_{l+1} \|\delta \mathbf{u}\|_{l+2} \end{aligned} \quad (5.64)$$

Together with (5.63), we then conclude that

$$\|\mathbf{Re}[\mu](\delta \mu)\|_{H^{l+2}} \leq C \|\delta \mu\|_{H^{l+1}}^2 \quad (5.65)$$

The estimates in (5.63) and (5.64) are uniform for bounded parameters μ . This proves Fréchet differentiability of \mathbf{u} .

5.8.3. Calculation of the adjoint operator

In this section, we calculate the adjoint of the linearized operator $\delta \mathbf{u}$ in (5.7) resp. (5.60).

Note that $\delta \mathbf{u} : H^{l+1}(\Omega) \rightarrow H^{l+2}(\Omega) \times H^{l+2}(\Omega)$.

We now claim that the adjoint of $\delta \mathbf{u}$ is

$$\begin{aligned} \delta \mathbf{u}^* : H^{l+2}(\Omega) \times H^{l+2}(\Omega) &\rightarrow H^{l+1}(\Omega) \\ \delta \mathbf{u}^* \mathbf{z} &= i^*(\varepsilon(\mathbf{u}) : \varepsilon(\mathbf{V} \mathbf{z})) \end{aligned} \quad (5.66)$$

with the linear operator $\mathbf{V} : H^2 \rightarrow H^4 \supset H^2$ given by

$$\begin{aligned} \mathbf{E}_\mu \mathbf{V} \mathbf{z} &= \mathbf{z} && \text{on } \Omega \\ \mathbf{V} \mathbf{z} &= 0 && \text{on } \partial \Omega. \end{aligned} \quad (5.67)$$

5. Convergent regularization methods for quantitative elastography

Here, $i : H^{l+1} \rightarrow L^2$ is the embedding operator, and the operation $A : B$ denotes the matrix scalar product: $A : B = \sum_{ij} A_{ij} B_{ij}$.

To see assertion (5.66), we calculate first the L^2 -adjoint, and then infer (5.66) using

$$\delta \mathbf{u}|_F = \delta \mathbf{u}|_{L^2} \circ i \quad (5.68)$$

Take $\mathbf{z} \in L^2$ and calculate with the definitions (5.59), equation (5.60), the definition (5.67) and partial integration in L^2 :

$$\begin{aligned} \langle \delta \mathbf{u}(\delta \mu), \mathbf{z} \rangle_{L^2 \times L^2} &\stackrel{(5.67)}{=} \langle \delta \mathbf{u}(\delta \mu), \mathbf{E}_\mu \mathbf{V} \mathbf{z} \rangle_{L^2 \times L^2} \\ &\stackrel{(5.59)}{=} - \int_{\Omega} \mu \, \varepsilon(\delta \mathbf{u}(\delta \mu)) : \varepsilon(\mathbf{V} \mathbf{z}) \, d\mathbf{x} \\ &\stackrel{(5.59)}{=} \langle \mathbf{E}_\mu \delta \mathbf{u}(\delta \mu), \mathbf{V} \mathbf{z} \rangle_{L^2 \times L^2} \\ &\stackrel{(5.60)}{=} - \langle \mathbf{E}_{\delta \mu} \mathbf{u}, \mathbf{V} \mathbf{z} \rangle_{L^2 \times L^2} \\ &= \int_{\Omega} \delta \mu \, \varepsilon(\mathbf{u}) : \varepsilon(\mathbf{V} \mathbf{z}) \, d\mathbf{x} \\ &= \langle \delta \mu, \varepsilon(\mathbf{u}) : \varepsilon(\mathbf{V} \mathbf{z}) \rangle_{L^2} \end{aligned}$$

This shows that the adjoint acts on $\mathbf{z} \in L^2$ as $\varepsilon(\mathbf{u}) : \varepsilon(\mathbf{V} \mathbf{z})$.

For the embedding: Using, (5.68) we have that

$$\delta \mathbf{u}|_F^* = i^* \circ \delta \mathbf{u}|_{L^2}^*,$$

and as claimed in (5.66), we have that the adjoint $\delta \mathbf{u}|_F^*$ acts as $i^*(\varepsilon(\mathbf{u}) : \varepsilon(\mathbf{V} \mathbf{z}))$.

6. Texture generation for photoacoustic elastography

Authors & Contributions The authors are T. Glatz, TW and O. Scherzer. The development of this article was a gradual, cooperative process, and each of the authors made significant contributions to every aspect of the paper.

Publication status Published, reference [53]. The original publication is available at <http://dx.doi.org/10.1007/s10851-015-0561-4>.

Abstract:

Elastographic imaging is a widely used technique which can in principle be implemented on top of every imaging modality. In elastography, the specimen is exposed to a force causing local displacements, and imaging is performed before and during the displacement experiment. The computed mechanical displacements can either directly be used for clinical diagnosis, or deliver a basis for the deduction of material parameters. Photoacoustic imaging is an emerging image modality, which exhibits functional and morphological contrast. However, opposed to ultrasound imaging, for instance, it is considered a modality which is not suited for elastography, because it does not reveal speckle patterns. However, this is somehow counter-intuitive, because photoacoustic imaging makes available the whole frequency spectrum as opposed to single frequency standard ultrasound imaging. In this work, we show that in fact artificial speckle patterns can be introduced by using only a band-limited part of the measurement data. We also show that after introduction of artificial speckle patterns, deformation estimation can be implemented more reliably in photoacoustic imaging.

Texture generation for photoacoustic elastography

Thomas Glatz¹, Otmar Scherzer^{1,2} and Thomas Widlak¹

¹ Computational Science Center, University of Vienna,
Oskar-Morgenstern-Platz 1, 1090 Vienna, Austria

² RICAM, Austrian Academy of Sciences,
Altenberger Straße 69, 4040 Linz, Austria

Contents

6.1	Introduction	89
6.2	Elastographic imaging	90
6.3	Photoacoustic imaging	92
6.4	Photoacoustics with band-limited data	94
6.5	PAI elastography using texture information	96
6.6	Feasibility of texture generation: A regularization point of view	99
6.7	Experiments	104
6.8	Discussion	108
6.9	Conclusion	110

6.1. Introduction

Elastography is an imaging technology for visualization of biomechanical properties; among its current clinical applications are early detection of skin, breast and prostate cancer, detection of liver cirrhosis, and characterization of atherosclerotic plaque in vascular imaging (see for instance [7, 30, 40, 106, 132, 134, 137]).

Typically, elastography is implemented as an *on top imaging method* to various existing imaging techniques, such as ultrasound imaging (see for instance [75, 103]), magnetic resonance imaging (see for instance [81, 93]) or optical coherence tomography (see for instance [94, 127]). With all these techniques, it is possible to visualize momentum images, from which mechanical displacements \mathbf{u} can be calculated, which forms the basis of clinical examinations.

For motion estimation in *ultrasound elastography (USE)*, *optical coherence elastography (OCE)* and in certain variants of *magnetic resonance elastography (MRE)*, common techniques are optical flow and motion tracking algorithms [31, 49, 106, 109, 110, 121]; in USE and OCE, these are specifically referred to as *speckle tracking methods*. Speckle tracking can only be realized if the imaging data contains a high amount of correlated pattern information. This is the predominant structure in ultrasound imaging.

Photoacoustic imaging is an emerging functional and morphological imaging technology, which, for instance, is particularly suited for imaging of vascular systems [27, 77, 100]. Opposed to ultrasound imaging, photoacoustic imaging is considered to reveal few speckle patterns [78], which is considered an advantage for imaging but a disadvantage for elastography. Passive coupling of photoacoustic imaging and elastography has been reported in [43], where the contrasts of photoacoustic imaging, ultrasound, and US-elastography have been fused (see also [106, sec.4.9]). Active coupling of photoacoustic and elastography has not been reported so far. The reason for that is that motion estimation and speckle tracking cannot be implemented reliably because of homogeneous regions in monospectral photoacoustic imaging, which do not allow for detection of microlocal displacements.

In this paper, we provide a mathematically founded way of introducing speckle in photoacoustic imaging data. Theoretically, photoacoustic imaging is based on the assumption that the whole frequency spectrum of the pressure can be measured by the detectors. Common ultrasound imaging, on the contrary, is operating with a fixed single frequency mode. This superficial comparison motivates us to investigate, using [56, 57], how much effect band-limited measurements have on the imaging process. In fact, as we show by mathematical consideration, the use of band-limited data enforces speckling-like patterns in the reconstructions. Our suggested approach then consists of carefully choosing a frequency band of measurements and back-projecting these data. Because these data are speckled, they can be used to support tracking and optical flow techniques for displacement estimations.

6. Texture generation for photoacoustic elastography

Our method of choice for detecting displacements in the photoacoustic imaging data is the *optical flow*. In pure mathematical terms, the equation is well-defined only for smooth imaging data. The high contrast of photoacoustic data causes a violation of this smoothness assumption. To make the photoacoustic data applicable for optical flow computations one can smooth the data prior to estimating the optical flow field [33]. In this paper, we show that the proposed method of texture generation is a convergent regularization method; compared to other smoothing techniques, like for instance Gaussian filtering, it performs better on high-contrast image data.

The structure of the article is as follows: We first review the principles of elastography in Section 6.2. In Section 6.3 we review the principles of photoacoustic imaging and in Section 6.4, we treat the case of band-limited data in photoacoustics. Then, in Section 6.5, we describe the methods to create texture patterns in photoacoustic imaging and use them for motion estimation for photoacoustic elastography. Section 6.6 provides a regularization point of view on texture generation: Anticipating the necessity of smoothing high contrast image data before optical flow processing, we show that smooth imaging data is in fact very well approximated by the proposed texture generation process. In Section 6.7, we show the results of imaging experiments. The paper ends with a discussion (Section 6.8).

6.2. Elastographic imaging

In this section we explain the basic principles of elastography. In theory, elastography can be implemented on top of any imaging technique. Below, we review mathematical models which are used for qualitative elastography.

6.2.1. Experiments and measurement principle

According to [40], elastography consists of the following consecutive steps:

1. The specimen is exposed to a mechanical source. Imaging is performed before and during source exposition.
2. **Qualitative elastography:** From the images the tissue displacement \mathbf{u} is determined.
3. **Quantitative elastography:** Mechanical properties are computed from the displacement \mathbf{u} .

In the literature there have been documented various ways to perturb the tissue, such as quasi-static, transient and time-harmonic excitation.

In this paper we focus on qualitative elastography in the quasi-static case, which is reviewed below.

6.2.2. Motion estimation in quasi-static qualitative elastography

Although it is theoretically possible to perform quantitative imaging all at once, in practice, qualitative imaging is performed beforehand. Depending on the used modalities different models are used for qualitative elastography (see for instance [106]):

We start from images $f(\mathbf{x}, t)$, which are recorded during the mechanical excitation. These images can be B-scan data in US-imaging, MRI magnitude images, OCT images, or in principle, images from any modality [106, 133].

In a *quasi-static* experiment, there are two images: before and after the mechanical excitation from the exterior. These images we denote as $f_1(\mathbf{x}) = f(\mathbf{x}, t_1)$ and $f_2(\mathbf{x}) = f(\mathbf{x}, t_2)$.

In the following, we derive the model for the continuous case, but later we specialize to the quasi-static case.

The most general model of continuity mechanics is the relation

$$f(\mathbf{x}(t), t) = \rho(t), \quad (6.1)$$

describing the change of intensity in a particle transported along the trajectory $\mathbf{x}(t)$. The displacement is then given by $\mathbf{u} = \dot{\mathbf{x}}(t)$. Taking the derivative in (6.1) and using $\frac{\partial \rho}{\partial t} + f \nabla \cdot \mathbf{u} = 0$ [123], we obtain an equation for the displacement vector field:

$$\nabla f \cdot \mathbf{u} + f_t = -f \nabla \cdot \mathbf{u}. \quad (6.2)$$

In the practice of elastography, it is almost always assumed that the tissue is incompressible, satisfying $\nabla \cdot \mathbf{u} = 0$, as well as $\rho(t) = \text{const.}$

The common models in elastography therefore are based either on

$$f(\mathbf{x}(t), t) = \text{const.} \quad (6.3)$$

or on the linearization

$$\nabla f \cdot \mathbf{u} + f_t = 0, \quad (6.4)$$

which is also called the *optical flow constraint*.

A model such as (6.3) can serve as a basis for an *image registration* model to recover (also larger) displacements $\mathbf{u} = \dot{\mathbf{x}}(t)$ from f (see [89] for general methods and for the special application [62] for detection of the movement of the heart, e.g.). In general, these are computationally expensive.

An alternative to registration is *block matching* [31]. Additionally to (6.3), one assumes here that the displacement is constant in defined regions; using a target block, one compares the image patterns in subsequent frames by using a correlation measure.

Alternatives are *optical flow* methods [139]. These methods are based on (6.4). This is the method used and analysed in this article.

6. Texture generation for photoacoustic elastography

We now consider the variant (6.4) in the *quasi-static case*. Here we are calculating the spatial dependent flow $\mathbf{u}(\mathbf{x})$ only by solving:

$$\nabla f_1 \cdot \mathbf{u} + (f_2 - f_1) = 0 . \quad (6.5)$$

The equation is underdetermined with respect to \mathbf{u} . Optical flow algorithms are designed to approximate a minimal norm solution \mathbf{u}^\dagger of (6.5). For instance, the variational Horn-Schunck model [61], consisting in computing

$$\mathbf{u} = \underset{\mathbf{v}}{\operatorname{argmin}} \|\nabla f_1 \cdot \mathbf{v} + (f_2 - f_1)\|_{L^2(\Omega)}^2 + \lambda \int_{\Omega} |\nabla_{\mathbf{x}} \mathbf{v}|^2 d\mathbf{x} , \quad (6.6)$$

approximates (for $\lambda \rightarrow 0$) a minimizer of the constrained optimization problem:

$$\int_{\Omega} |\nabla_{\mathbf{x}} \mathbf{v}|^2 d\mathbf{x} \text{ subject to } \nabla f_1 \cdot \mathbf{v} = f_1 - f_2 . \quad (6.7)$$

6.2.3. The role of texture in motion estimation

In ultrasound imaging and optical coherence tomography, texture is provided by patterns in the images referred to as *speckle*. These are correlated texture patterns which provide a signature of the points. Block-matching-type algorithms are therefore often called as *speckle tracking* algorithms [31, 105]. Sometimes, any motion estimation in USE or OCE is comprehensively referred to as *speckle tracking* [113, 139].

In MRI, it was observed that part of tissue motion is invisible in magnitude images because of homogeneous regions. To overcome this limitation, artificial tags have been introduced in the image [49, 110]. These make motion estimation possible in regions where no intensity is initially present.

Artificial speckle or texture introduction is a frequently used technique for deformation detection in material science. Here, often airbrush techniques are being used as a pre-processing step to correlation techniques [74, 142].

In the next section, we review photoacoustic imaging. In Section 6.4 we demonstrate that band-limitation of the measurement data creates a speckle-like texture pattern in photoacoustic image data.

6.3. Photoacoustic imaging

Photoacoustic imaging (PAI) is among the most prominent coupled-physics techniques [14]. It operates with laser excitation and records acoustic pressure, as the coupled modality. We first review the imaging formation in PAI.

6.3.1. Mathematical modeling

Commonly, in Photoacoustics, the wave equation is used to describe the propagation of the acoustic pressure p :

$$\begin{aligned} p_{tt} - \Delta_{\mathbf{x}} p &= I_t f, & \text{in } \mathbb{R}^n \times (0, T], \\ p &= 0, & \text{in } \mathbb{R}^n \times (-\infty, 0). \end{aligned} \quad (6.8)$$

The function I models the laser excitation and is usually considered a time dependent δ -distribution. The function f represents the capability of the medium to transfer electromagnetic waves into pressure waves; f is material dependent and is visualized in photoacoustic imaging.

Details of deduction of (6.8) from the Euler equations and the diffusion equation of thermodynamics can be found for instance in [118].

If we assume the excitation to be perfectly focused in time (that is $I(t) = \delta(t)$), equation (6.8) can be reformulated as a homogeneous initial value problem [118]

$$\begin{aligned} p_{tt} - \Delta_{\mathbf{x}} p &= 0, & \text{in } \mathbb{R}^n \times (0, \infty), \\ p(t=0) &= f, & \text{in } \mathbb{R}^n, \\ p_t(t=0) &= 0, & \text{in } \mathbb{R}^n. \end{aligned} \quad (6.9)$$

This (direct) problem is well-posed under suitable smoothness assumptions on f (see, e.g., [45]). We denote by

$$\mathcal{P}f(\mathbf{x}, t) = p(\mathbf{x}, t), \quad \mathbf{x} \in \mathbb{R}^n, \quad t \in (0, \infty), \quad (6.10)$$

the operator that maps the initial pressure f to the solution of (6.9).

Remark 7. Since we want to apply a convolution to our solution p , we have to extend it to negative values of t in a way that the wave equation (6.9) is still fulfilled. We distinguish the causal extension $\mathcal{P}f = 0$ for $t < 0$ (that we denote again with the letter \mathcal{P}), and the even extension

$$\mathcal{P}_{\text{even}}f(\mathbf{x}, t) := \begin{cases} \mathcal{P}f(\mathbf{x}, t), & t \geq 0, \\ \mathcal{P}f(\mathbf{x}, -t), & t < 0. \end{cases} \quad (6.11)$$

6.3.2. Photoacoustic imaging as an inverse problem

In Photoacoustics, we assume the pressure to be measured on a surface Γ over time. The inverse problem now consists of reconstructing the initial pressure f in (6.9) from these data, ideally given as trace of the solution on Γ . For the sake of simplicity of notation, we are denoting this operator by

$$\mathcal{P}f = p|_{\Gamma \times (0, \infty)} \quad (6.12)$$

as well. Here, \mathcal{P} is mapping f to the trace of the solution p of (6.9) at the surface Γ . The *Photoacoustic inverse problem* consists in solving equation (6.12) for f .

6. Texture generation for photoacoustic elastography

This problem obtains a unique solution, provided Γ is a so-called uniqueness set (for a review over existing results see [69]). These uniqueness sets contain the case of a closed measurement surface surrounding the photoacoustic source.

For some of the most important simple geometrical shapes of closed manifolds Γ , there exist analytical reconstruction formulae of series expansion and/or filtered backprojection type (see again [69] and the references therein, for instance [42, 46, 47, 48, 97, 98, 99, 104, 112]).

This paper focuses on the case where Γ is a sphere in \mathbb{R}^2 (circle) or \mathbb{R}^3 . For photoacoustic reconstruction, we make use of the explicit filtered backprojection formulas established in [47, 48]. Since we will have to deal with initial sources not necessarily of compact support, we remark that a result in [6] guarantees injectivity of the photoacoustic problem provided certain integrability conditions on the source hold. Particularly, the photoacoustic mapping is injective if and only if the source is L^p -integrable on the entire space, where $p \leq 2n/(n-1)$.

6.4. Photoacoustics with band-limited data

We create speckle patterns computationally from photoacoustic data using band-limited measurements for back-projection and approximating the initial source f . To be more precise, instead of measuring the exact trace of the solution of (6.9) at Γ , we instead assume to measure the band-limited data $m = \phi *_t p$ (see Definition 3).

The mathematical background is an application of some results by Haltmeier [56, Lmm. 3.1] (see also [57, 58]) to convolution kernels which do not necessarily have compact support. Before we state the theorem, we define the Radon und Fourier transform (based on [60, p.1 ff]):

Definition 1. *The Radon transform $\mathcal{R}\varphi(\theta, s)$ maps $\varphi(\mathbf{x})$ to its integrals over hyperplanes in \mathbb{R}^n with distance $s \in \mathbb{R}$ to the origin and unit normal vector $\theta \in S^{n-1}$. Namely,*

$$\mathcal{R}\varphi(\theta, s) = \int_{\theta \cdot \mathbf{y} = s} \varphi(\mathbf{y}) d\mathbf{y}. \quad (6.13)$$

In the case $n = 1$, the Radon transform corresponds to the absolute value of the function. In the case where φ is rotationally symmetric, the Radon transform $\mathcal{R}\varphi$ is independent of θ . We can therefore write

$$\mathcal{R}\varphi(\theta, s) = \phi(s) \quad (6.14)$$

for a suitable, even function $\phi : \mathbb{R} \rightarrow \mathbb{R}$.

Definition 2. *The n -dimensional Fourier transform $\widehat{\varphi}(\boldsymbol{\kappa})$ of φ is defined as*

$$\widehat{\varphi}(\boldsymbol{\kappa}) = \frac{1}{(2\pi)^{n/2}} \int_{\mathbb{R}^n} \varphi(\mathbf{y}) e^{-i\mathbf{y} \cdot \boldsymbol{\kappa}} d\mathbf{y}. \quad (6.15)$$

If not stated differently, the Fourier transform of a time-dependent function $q(\mathbf{x}, t)$ is with respect to the time variable, i.e.

$$\widehat{q}(\mathbf{x}, \kappa) = \frac{1}{\sqrt{2\pi}} \int_{\mathbb{R}} q(\mathbf{x}, t) e^{-it\kappa} dt .$$

Definition 3. The n -dimensional convolution $f *_x g$ is defined, as usual, by

$$f *_x g(\mathbf{x}) = \int_{\mathbb{R}^n} f(\mathbf{y}) g(\mathbf{x} - \mathbf{y}) d\mathbf{y} , \quad (6.16)$$

where f, g functions from \mathbb{R}^n to \mathbb{R} . The sub-index in $*_x$ thereby clarifies the variable, in which the convolution is performed.

In a formal manner, the following theorem has been stated already by Haltmeier [56]. However, there is a subtle difference to our work, which is that the convolution function Ψ has compact support in [56, Lemma 3.1], which is not the case here.

Theorem 15. Let $p = \mathcal{P}f$ be a solution of (6.10) with initial pressure $f \in H^1(\mathbb{R}^n)$, with compact support. Moreover, let $\Psi \in L^p(\mathbb{R}^n)$, for some p such that $1 \leq p < n/(n-1)$, be radially symmetric, i.e., $\Psi(\mathbf{x}) = \psi(|\mathbf{x}|)$. Then

$$(\mathcal{P}(\Psi *_x f))(\mathbf{x}, t) = (\mathcal{R}\Psi *_t \mathcal{P}_{\text{even}}f)(\mathbf{x}, t) , \quad (6.17)$$

for all $\mathbf{x} \in \mathbb{R}^n$, $t > 0$.

Under the assumptions of the theorem the proof is analogous to the proof in [56, Lemma 3.1]. It employs that the Radon transform, in an *almost everywhere* sense, is injective on L^p -functions for $1 \leq p < n/(n-1)$ [125]. Note, however, that because of the non-compactness of the support of the function Ψ , the minimal smoothness assumptions on the imaging data f and the convolution kernel are not clarified so far, and are open to basic research.

For application of Theorem 15 to the measured, *causal* band-limited data, we need to give a relation to the data *even* in time, as they appear in the theorem. This relation is given in the following proposition:

Proposition 1. Let $1 \leq p < n/(n-1)$. Moreover, let $\Psi \in L^p(\mathbb{R}^n)$ be radially symmetric. Then (see (6.14)) $\phi(s) := \mathcal{R}\Psi(\theta, s)$ is even and independent of θ . Moreover, let

$$m(\mathbf{x}; t) = (\phi *_t \mathcal{P}f)(\mathbf{x}; t) \quad \text{on } \Gamma \times (0, \infty) .$$

Then,

$$m_{\text{even}}(\mathbf{x}, t) = (\phi *_t \mathcal{P}_{\text{even}}f)(\mathbf{x}, t) \quad \text{on } \Gamma \times (0, \infty) , \quad (6.18)$$

where $\mathbf{x} \in \Gamma, t \in (0, \infty)$ can be computed from the causal measurement data $m(\mathbf{x}, t)$, via the Fourier relation

$$\widehat{m_{\text{even}}}(\mathbf{x}, \kappa) = 2\text{Re}(\widehat{m}(\mathbf{x}, \kappa)) \quad \text{on } \Gamma \times (0, \infty) .$$

6. Texture generation for photoacoustic elastography

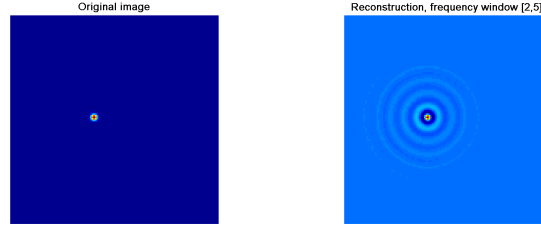


Figure 6.1.: Point source (left) and textured reconstruction (right)

Proof. Let p denote the solution of (6.9). Since $p(\mathbf{x}; t)$ is real-valued, it follows that

$$\widehat{p}(\mathbf{x}, -\kappa) = \overline{\widehat{p}(\mathbf{x}, \kappa)} \quad \forall \mathbf{x} \in \mathbb{R}^n, \kappa \in \mathbb{R},$$

and therefore

$$\widehat{\mathcal{P}_{\text{even}} f}(\mathbf{x}, \kappa) = 2 \operatorname{Re}(\widehat{p}(\mathbf{x}, \kappa)) \quad \forall \mathbf{x} \in \mathbb{R}^n, \kappa \in \mathbb{R}.$$

Thus, from (6.18) it follows that

$$\begin{aligned} \widehat{m_{\text{even}}}(\mathbf{x}, \kappa) &= \widehat{\phi}(\kappa) \widehat{\mathcal{P}_{\text{even}} f}(\mathbf{x}, \kappa) \\ &= \widehat{\phi}(\kappa) 2 \operatorname{Re}(\widehat{\mathcal{P} f}(\mathbf{x}, \kappa)) \\ &= 2 \operatorname{Re}(\widehat{\phi}(\kappa) \widehat{\mathcal{P} f}(\mathbf{x}, \kappa)) \\ &= 2 \operatorname{Re}(\widehat{m}(\mathbf{x}, \kappa)) \quad \forall \mathbf{x} \in \Gamma, \forall \kappa \in \mathbb{R}, \end{aligned}$$

where in the third equality we use that $\widehat{\phi}$ is real-valued, since ϕ is a real-valued and even function. \square \square

Proposition 1 gives a simple relation between convolved m_{even} and measurement data m . In fact Theorem 15 and Proposition 1 then show that

$$(\mathcal{P}(\Psi *_x f))(\mathbf{x}, t) = (\mathcal{R}\Psi *_t \mathcal{P} f)_{\text{even}}(\mathbf{x}, t), \quad (6.19)$$

which can be computed directly from the measurement data $\mathcal{P} f$.

6.5. PAI elastography using texture information

The results of Section 6.4 give the theoretical background on the influence of band-limitation of the measurement data on the photoacoustic imaging. In the following subsection we describe how to find pairs of filter functions ϕ and Ψ in practice. Moreover, we give an example of a pair of oscillating functions, that we use in what follows to create speckle-like patterns on photoacoustic images. The rest of the paper treats the case of two spatial dimensions. Since the theoretical considerations from Section 6.4 are valid in any spatial dimension, the application to 3D images works in complete analogy to the two-dimensional case described below.

6.5.1. Speckle generation in 2D Photoacoustics

We assume to measure the bandpass data

$$m = \phi *_t \mathcal{P}f ,$$

where

$$\phi(t) = \frac{2\sqrt{2} \cos(\kappa_0 t) \sin(at)}{\sqrt{\pi} t} , \quad (6.20)$$

is the Fourier transform of the bandpass filter:

$$\widehat{\phi}(\mathbf{x}, \kappa) = \chi_{[\kappa_{\min}, \kappa_{\max}]}(|\kappa|) . \quad (6.21)$$

Here $2a = \kappa_{\max} - \kappa_{\min}$ is the bandwidth and $\kappa_0 = \kappa_{\min} + a$ is the center frequency of the filter.

The results of Section 6.4 describe the equivalence relationship of the filter for the measurement data in time and a resulting filter in space for the imaging data. But since we actually want to compute this space filter explicitly, it is convenient to make use of the so-called *Fourier-slice* theorem for the Radon transform [60, p.4][125], that relates the Fourier transform of the Radon transform (in radial direction) to the Fourier transform of the image (in all spatial dimensions).

The corresponding point-spread function Ψ is given by

$$\Psi(\mathbf{x}) = \frac{\kappa_{\max} J_1(\kappa_{\max} |\mathbf{x}|) - \kappa_{\min} J_1(\kappa_{\min} |\mathbf{x}|)}{\sqrt{2\pi} |\mathbf{x}|} , \quad (6.22)$$

where J_1 is the first-kind Bessel function of order 1. By using an asymptotic estimate of J_1 for large arguments, it is easy to check that $\Psi \in L^p(\mathbb{R}^2)$ iff $p > 4/3$, which means that Ψ fulfils the integrability requirements demanded in Theorem 15. This ensures that the result actually applies to the used filter.

Note that the function pair (6.20), (6.22) does not have compact support, so that we really need the extension to L^p functions in Theorem 15.

Our suggested approach for texture generation then is this: We choose κ_{\max} and κ_{\min} to determine the impulse response ϕ . Then we compute m_{even} and solve the photoacoustic inverse problem with data m_{even} . Theorem 15 then ensures that this yields the perturbed reconstruction

$$f *_x \Psi . \quad (6.23)$$

With the right choice of κ_{\min} and κ_{\max} , this is a natural candidate for a textured variant of the photoacoustic data f .

In Figure 6.1, a point source and its photoacoustic reconstruction from band-limited data (i.e., data convolved with the impulse response in (6.20)) are shown. The oscillations introduced by the present band-limited photoacoustic reconstruction method introduce additional texture on the image.

6. Texture generation for photoacoustic elastography

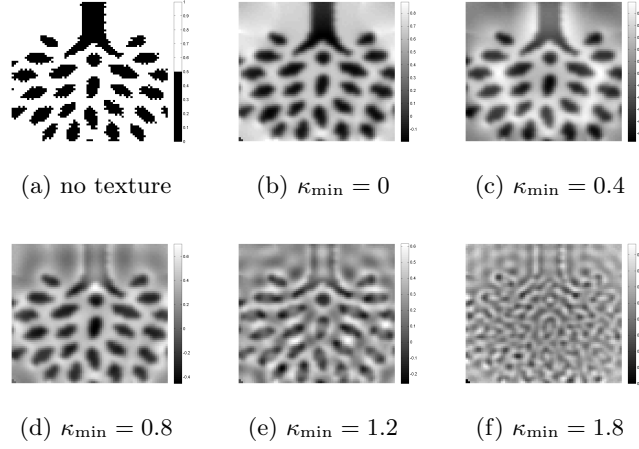


Figure 6.2.: The filling-in-effect of the bandpass limitation: homogeneous regions are filled by the neighboring structures. Different versions computed with $\kappa_{\max} = 10$, with varying κ_{\min} .

In Figure 6.2, a sample containing homogeneous regions is shown, together with the effect of band-limitation for fixed $\kappa_{\max} = 10$, but varying values of κ_{\min} . In this more complex sample, we see that the oscillations introduced by band-limitation serve to fill in homogeneous regions of the sample, and the structure of the edges is propagated locally around the shapes. This exhibits, particular for larger values, a texture pattern in the image. The use of this texture in estimating the optical flow between two photoacoustic images is investigated in the following sections.

6.5.2. Principle of PAI elastography

In the previous subsection, we introduced a texture method for photoacoustic images. We now will study how motion estimation can be performed and amended by adding texture to photoacoustic images.

We emphasize that the initial pressure f introduced in (6.9) in the photoacoustic forward problem is spatially varying and can either represent the image before (i.e., f_1) or after (f_2) mechanical deformation as described in Section 6.2.2.

The main concept in the proposed method of *photoacoustic elastography* is to perform the following steps in the first step in Section 6.2.1:

- a) record a PAI image f_1 using the texture-generating method
- b) perturb the tissue using a mechanical source
- c) record the perturbed configuration f_2 using the texture-generation method

We will now estimate the displacement \mathbf{u} as in the second step in Section 6.2.1.

6.6. Feasibility of texture generation: A regularization point of view

Remark 8. We emphasize that the convolution introduced in (6.23) commutes with rigid deformations: From (6.16), we have

$$f *_x \Psi(\mathbf{x}) = \int_{\mathbb{R}^n} \Psi(\mathbf{y}) f(\mathbf{x} - \mathbf{y}) d\mathbf{y},$$

hence

$$\begin{aligned} f *_x \Psi(\mathbf{x} - \mathbf{z}) &= \int_{\mathbb{R}^n} \Psi(\mathbf{y}) f(\mathbf{x} - \mathbf{y} - \mathbf{z}) d\mathbf{y} \\ &= (f(\mathbf{x} - \mathbf{z}) *_x \Psi)(\mathbf{x}), \end{aligned}$$

which implies commutation with translations.

For a rotation $\mathbf{R} : \mathbf{x} \mapsto \mathbf{R}\mathbf{x}$, we have

$$f *_x \Psi(\mathbf{R}\mathbf{x}) = \int_{\mathbb{R}^n} \Psi(\mathbf{y}) f(\mathbf{R}\mathbf{x} - \mathbf{y}) d\mathbf{y}. \quad (6.24)$$

On the other hand,

$$\begin{aligned} (f(\mathbf{R}\mathbf{x}) *_x \Psi)(\mathbf{x}) &= \int_{\mathbb{R}^n} \Psi(\mathbf{y}) f(\mathbf{R}\mathbf{x} - \mathbf{R}\mathbf{y}) d\mathbf{y} \\ &= \int_{\mathbb{R}^n} \Psi(\mathbf{R}^{-1}\mathbf{z}) f(\mathbf{R}\mathbf{x} - \mathbf{z}) d\mathbf{z}. \end{aligned}$$

Due to rotation invariance of Ψ , we have that $\Psi(\mathbf{R}^{-1}\mathbf{y}) = \Psi(\mathbf{y})$, therefore we have the same result as on the right hand side of (6.24).

For any rigid motion, the texture created by our method behaves strictly as a material characteristic advected with the vector field.

One might conjecture that for non-linear deformations \mathbf{u} , the convolution does not commute with forward transport along \mathbf{u} . An example of the different variants is given in Figure 6.3 for simulated data and a non-linear vector field (later employed in Experiment 2). This is shown for two values of the band-width, $\kappa_{\min} = 0.4$ and $\kappa_{\min} = 1.8$

In the first picture, the image f is textured, and then transported. In the second picture, the image f is transported, then textured. The third picture shows the difference. In fact, for the deformations we used, this difference in the optical flow is not significant. This is shown in the experiments of Section 6.7.

6.6. Feasibility of texture generation: A regularization point of view

The Horn-Schunck method (6.6) is a special instance of Tikhonov regularization [118, 3.1]. In this section, we show that adapting the Horn-Schunck method to textured images introduced in Section 6.4, yields a convergent regularization scheme in the sense of Theorem 16 below.

6. Texture generation for photoacoustic elastography

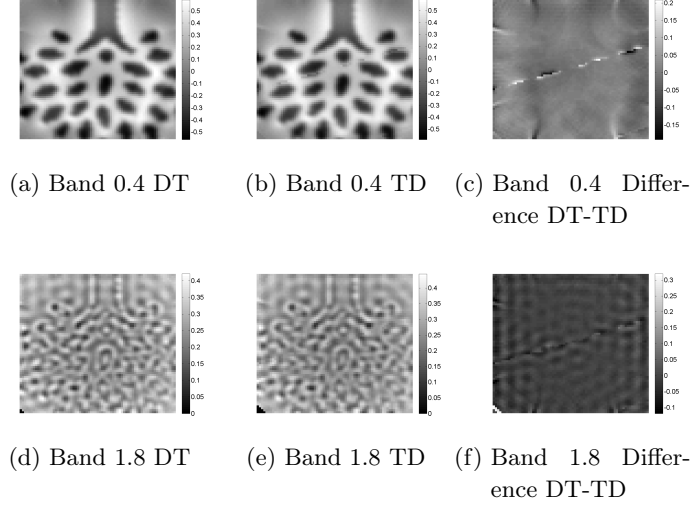


Figure 6.3.: The difference of the order of deformation (D) and texturation (T), with texture from $\kappa_{\min} = 0.4$ (first row) and $\kappa_{\min} = 1.8$ (second row). See text for discussion.

Note first that the optical flow equation (6.4), (6.5) is only well-defined if the image data f , f_1 and f_2 , respectively, are smooth enough. This is typically not the case in photoacoustic imaging, because the images have high contrast, or in other words f_1 and f_2 can have jump interfaces. In order to make the smoothness statement precise we have to formulate the optical flow equation in a function space setting.

6.6.1. Optical flow equation in a function space setting

Our optical flow algorithm choice for elastography is the Horn-Schunck method (6.6). To make sure that it is well-posed we have to make sure ensure that (6.5) holds in an L^2 -setting, or in other words that the optical flow residual is an element of $L^2(\Omega)$ and that the flow is in $H_0^1(\Omega)$.

To further proceed we introduce the parameter $0 < \varepsilon < 1$, and associate

$$\kappa_{\max} = 1/\varepsilon \text{ and } \kappa_{\min} = \varepsilon .$$

Accordingly we define the parametric family of functions,

$$\Psi_\varepsilon(\mathbf{x}) = \frac{\frac{1}{\varepsilon} J_1\left(\frac{1}{\varepsilon}|\mathbf{x}|\right) - \varepsilon J_1(\varepsilon|\mathbf{x}|)}{\sqrt{2\pi}|\mathbf{x}|}, \quad (6.25)$$

and introduce the operators

$$\begin{aligned} F : H_0^1(\Omega) &\rightarrow L^2(\Omega), & \mathbf{u} &\mapsto \nabla f_1 \cdot \mathbf{u}, \\ F_\varepsilon : H_0^1(\Omega) &\rightarrow L^2(\Omega), & \mathbf{u} &\mapsto \nabla(f_1 * \Psi_\varepsilon) \cdot \mathbf{u}. \end{aligned} \quad (6.26)$$

6.6. Feasibility of texture generation: A regularization point of view

With these operators the quasi-static optical flow equation (6.5) can be rewritten as

$$F\mathbf{u} = f_1 - f_2 . \quad (6.27)$$

In contrast, if we base optical flow calculations on speckled data $f *_{\mathbf{x}} \Psi_\varepsilon$, then the according quasi-static optical flow equation (6.5) reads as follows:

$$F_\varepsilon \mathbf{u} = (f_1 - f_2) *_{\mathbf{x}} \Psi_\varepsilon . \quad (6.28)$$

In the following we prove that F and F_ε are well-defined and continuous:

Lemma 1. *Let $f_1 \in H_0^2(\Omega)$. Then the operators F , F_ε in (6.27), (6.28) are well-defined and bounded.*

Proof. Let $\mathbf{a} \in H_0^1(\Omega)$.

Then, by using the Euclidean Cauchy-Schwarz inequality, continuity of the Sobolev-embedding from $H^1(\Omega)$ into $L^4(\Omega)$ and the Poincaré-Friedrichs inequality [2] it follows that:

$$\int_{\Omega} |\mathbf{a} \cdot \mathbf{u}|^2 d\mathbf{x} \leq \int_{\Omega} |\mathbf{a}|^2 |\mathbf{u}|^2 \leq \left(\int_{\Omega} |\mathbf{a}|^4 \int_{\Omega} |\mathbf{u}|^4 \right)^{1/2} \quad (6.29)$$

$$\leq C_1 \|\mathbf{a}\|_{H^1(\Omega)}^2 C_2 \|\mathbf{u}\|_{H^1(\Omega)}^2 \leq C \|\nabla \mathbf{u}\|_{L^2(\Omega)}^2 . \quad (6.30)$$

Thus for either choice $\mathbf{a} = \nabla f_1$ and $\mathbf{a} = \nabla f_1 *_{\mathbf{x}} \Psi_\varepsilon$ the continuity assertion about F and F_ε follows. \square \square

Moreover, in the following, we derive an estimate for the operator perturbation $\|F - F_\varepsilon\|$. Therefore, we use the following lemma:

Lemma 2. *Let Ψ_ε as defined in (6.25). Let $f_1, f_2 \in H_0^2(\Omega)$. Then the following statements hold:*

1. $\lim_{\varepsilon \rightarrow 0} \|\nabla (f_1 - f_1 *_{\mathbf{x}} \Psi_\varepsilon)\|_{H^1(\Omega)}^2 = 0$.
2. The operator $F - F_\varepsilon$ is bounded, and the operator norm $\|F - F_\varepsilon\|$ goes to zero, as $\varepsilon \rightarrow 0$.
3. The L^2 -distance $\|f_i - f_i *_{\mathbf{x}} \Psi_\varepsilon\|_{L^2(\mathbb{R}^n)} = \mathcal{O}(\varepsilon)$, with $i = 1, 2$ as $\varepsilon \rightarrow 0$.

Proof. The function $f_i \in H_0^2(\Omega)$, where $i = 1, 2$, is identified with the function $f_i : \mathbb{R}^2 \rightarrow \mathbb{R}$, which is vanishing outside of Ω . With this extension it follows that

$$\|\nabla (f_1 - f_1 *_{\mathbf{x}} \Psi_\varepsilon)\|_{H^1(\Omega)}^2 \leq \|\nabla (f_1 - f_1 *_{\mathbf{x}} \Psi_\varepsilon)\|_{H^1(\mathbb{R}^2)}^2 .$$

In the following let us denote by \mathbb{B}_r a ball with radius r in \mathbb{R}^2 . Then by using the equivalence of the Sobolev norm to the Fourier representation [2, p. 252], it

6. Texture generation for photoacoustic elastography

follows that

$$\begin{aligned}
& \|\nabla(f_1 - f_1 *_{\mathbf{x}} \Psi_\varepsilon)\|_{H^1(\mathbb{R}^2)}^2 \\
& \leq C \|(1 + |\xi|)|\xi|\widehat{f}_1|(1 - \Psi_\varepsilon)\|_{L^2(\mathbb{R}^n)}^2 \\
& \leq C \left(\int_{\mathbb{B}_\varepsilon} (1 + |\xi|^2)|\xi|^2|\widehat{f}_1|^2 + \int_{\mathbb{R}^2 \setminus \mathbb{B}_{\frac{1}{\varepsilon}}} (1 + |\xi|^2)|\xi|^2|\widehat{f}_1|^2(1 - \widehat{\Psi}_\varepsilon) \right), \tag{6.31}
\end{aligned}$$

by splitting the integral into an inner and outer part. Since we have $\widehat{\Psi}_\varepsilon \equiv 1$ on the annulus $|\xi| \in (\varepsilon, \frac{1}{\varepsilon})$, the integral vanishes in this area. Since $\widehat{f} \in L^\infty(\mathbb{R}^2)$ (due to the absolute integrability of f), the integrand in the first term can be bounded by $C(1 + \varepsilon^2)\varepsilon^2$. This implies that the first integral is of order ε^4 , as ε goes to zero. That is,

$$\begin{aligned}
& \|\nabla(f_1 - f_1 *_{\mathbf{x}} \Psi_\varepsilon)\|_{H^1(\Omega)}^2 \\
& \leq C \int_{\mathbb{R}^2 \setminus \mathbb{B}_{\frac{1}{\varepsilon}}} (1 + |\xi|^2)|\xi|^2|\widehat{f}_1|^2(1 - \widehat{\Psi}_\varepsilon) + \mathcal{O}(\varepsilon^4),
\end{aligned}$$

as $\varepsilon \rightarrow 0$. Due to the Lebesgue dominated convergence theorem and the assumption that $f \in H^2(\mathbb{R}^n)$, the remaining term converges to zero as well. This shows the first assertion. Statement two then follows immediately from (6.29) by choosing

$$\mathbf{a} = \nabla(f_1 - f_1 *_{\mathbf{x}} \Psi_\varepsilon).$$

To prove the last statement, we use Plancherel's identity and the fact that $f_i \in H_0^1(\Omega)$ to estimate

$$\begin{aligned}
\|f_i - f_i *_{\mathbf{x}} \Psi_\varepsilon\|_{L^2}^2 &= \|\widehat{f}_i - \widehat{\Psi}_\varepsilon \widehat{f}_i\|_{L^2}^2 = \int_{\mathbb{R}^2} |\widehat{f}_i|^2 (1 - \widehat{\Psi}_\varepsilon) \\
&= \int_{\mathbb{B}_\varepsilon} |\widehat{f}_i|^2 + \int_{\mathbb{R}^2 \setminus \mathbb{B}_{\frac{1}{\varepsilon}}} |\widehat{f}_i|^2 \\
&\leq \int_{\mathbb{B}_\varepsilon} |\widehat{f}_i|^2 + \frac{1}{(1 + 1/\varepsilon^2)} \int_{\mathbb{R}^2 \setminus \mathbb{B}_{\frac{1}{\varepsilon}}} (1 + |\xi|^2) |\widehat{f}_i|^2
\end{aligned} \tag{6.32}$$

Using the same argumentation as in (6.31), both terms are of order $\mathcal{O}(\varepsilon^2)$ as $\varepsilon \rightarrow 0$, which finishes the proof. \square \square

Remark 9. In Lemma 2, we try to demand the minimal smoothness assumptions on f_1 necessary to guarantee the validity of statement 1. Note that, analogous to the considerations in (6.32), we could employ higher smoothness of f to receive a convergence rate estimate for $\|F - F_\varepsilon\|$.

6.6.2. General regularization theory

In the following we review a classical result from regularization theory [91, Thm.11, p. 21] (in a slightly simplified form). The referenced theorem says that Tikhonov regularization with an operator perturbation is a convergent regularization procedure.

Let $F : W \rightarrow Y$ be a bounded operator between Hilbert spaces W and Y . For y in the range of F a minimum-norm-solution w^\dagger satisfies

$$w^\dagger = \operatorname{argmin}_W \{ \|w\|_W : Fw = y \} .$$

Theorem 16. *Let $F, F_\varepsilon : W \rightarrow Y$ be bounded linear operators between Hilbert spaces W, Y with*

$$\|F - F_\varepsilon\| \rightarrow 0 . \quad (6.33)$$

Moreover, let $y \in R(F)$ and y^δ satisfy

$$\|y - y^\delta\| \rightarrow 0 . \quad (6.34)$$

Let Tikhonov regularized solutions according to F_ε be defined as

$$w_{\alpha,\varepsilon}^\delta := \operatorname{argmin} \|F_\varepsilon w - y^\delta\|_Y^2 + \alpha \|w\|_W^2 . \quad (6.35)$$

Then there exists a parameter choice $\alpha := \alpha(\delta, \varepsilon)$ such that

$$\lim_{\delta \rightarrow 0, h \rightarrow 0} w_{\alpha,h}^\delta = w^\dagger . \quad (6.36)$$

6.6.3. Application of general regularization theory to the optical flow problem

We apply the general Theorem 16 to Horn-Schunck regularization. To establish the coherence we take $W = H_0^1(\Omega), Y = L^2(\Omega)$ and F, F_ε as in (6.27),(6.28). Note that according to Lemma 2, we have that $F_\varepsilon \rightarrow F$. We set

$$\begin{aligned} w &= \mathbf{u}, & y &= f_2 - f_1, & \delta &= \varepsilon, \\ y^\delta &= (f_2 - f_1) *_{\mathbf{x}} \Psi_\varepsilon \rightarrow y . \end{aligned}$$

Therefore, with $\varepsilon \rightarrow 0$, both the model perturbation condition (6.33) as well as the data perturbation condition (6.34) hold.

Define now $\mathbf{u}_{\alpha,\varepsilon}$ as the regularized solution (6.35) for our case:

$$\mathbf{u}_{\alpha,\varepsilon} := \operatorname{argmin}_{\mathbf{v}} \|\nabla(f_1 * \Psi_\varepsilon) \cdot \mathbf{v} - (f_2 - f_1) * \Psi_\varepsilon\|_{L^2}^2 + \alpha \|\mathbf{v}\|_{H_0^1}^2 . \quad (6.37)$$

Now we easily derive that the minimizer according (6.37) provides a convergent regularization scheme:

6. Texture generation for photoacoustic elastography

Corollary 1. *For given $f_1, f_2 \in H_0^2(\Omega)$ let there exist a solution \mathbf{u} of (6.5). Then there exists a solution \mathbf{u}^\dagger of (6.7) (i.e. it is a minimum norm solution).*

Moreover, let $\mathbf{u}_{\alpha,\varepsilon}$ be the minimizer of (6.37). Then there exists a parameter choice $\alpha = \alpha(\varepsilon)$, such that

$$\lim_{\varepsilon \rightarrow 0^+} \mathbf{u}_{\alpha,\varepsilon} = \mathbf{u}^\dagger. \quad (6.38)$$

Remark 10. The above results show that if the input image sequence for the optical flow is in $H_0^2(\Omega)$, then the Horn-Schunck regularized solutions with band-filtered data approximate the solution of the constrained optimization problem (6.6) and (6.7) if the band tends to cover the whole frequency range. In practice, a limited frequency range gives already quite accurate reconstructions. On the other hand we also have outlined that image data smoothing is indispensable for optical flow computations because the optical flow equation is not well-defined when discontinuities or singularities appear in the images.

6.7. Experiments

There are many different varieties of experiments one can perform. In this section, we present a first selection, using structures which contain homogeneous regions, similar to vascular structures. The computed displacements (with the parameters described below) are shown in Figures 5-8.

6.7.1. Simulations

We simulate photoacoustic measurement data using the k-wave toolbox [129]. For reconstruction, we use a filtered back-projection algorithm. Displacement vector fields have been simulated using the FEM and mesh-generating packages GetDP and Gmsh [41, 50].

6.7.2. Material, displacement and parameters

The synthetic material was chosen to exhibit homogeneous regions surrounded by edges. In each experiment, we evaluated a rigid deformation (Experiment 1 and 3) and a non-rigid deformation (Experiment 2 and 4).

In Experiments 1 and 2, we use a tree structure designed by Brian Hurshman and licensed under CC BY 3.0¹.

6.7.3. Texture Modes

We compare the proposed texture creation in (6.23) to different alternative versions of filling in homogeneous regions in the image data. To this purpose, we choose one the following texture operators T . (We give the different abbreviations we use for these texture modes in Tables 6.1, 6.2, 6.3.)

¹ <http://thenounproject.com/term/tree/16622/>

For the band-limitation-induced texture in (6.23), we set $\kappa_{\max} = 10$, and compare $\Psi_{\kappa_{\min}}$ for different values of κ_{\min} , precisely we compare

$$T : \quad f \mapsto f * \Psi_{0.4} \quad (6.39)$$

which is referred to as *Band 0.4*, and

$$T : \quad f \mapsto f * \Psi_{1.8} \quad (6.40)$$

which is referred to as *Band 1.8*.

Other possible operations on the image to fill in homogeneous regions are:

$$T : \quad f \mapsto f + r \quad (6.41)$$

where r is Gaussian random noise of 30 %, abbreviated as *Gaussian 0.3*;

$$T : \quad f \mapsto f * \sigma \quad (6.42)$$

where σ is a Gauss kernel of size 3×3 pixels, abbreviated as *Gauss Conv 3×3* ;

$$T : \quad f \mapsto f * \chi \quad (6.43)$$

where χ is constant with $\text{supp}(\chi)$ being a rectangle of pixel length 3, with $\int_{\Omega} \chi = 1$, referred to as *Aver Conv 3×3* ;

$$T : \quad f \mapsto SP(f) \quad (6.44)$$

where SP is Salt and Pepper noise applied to the image with parameter $p = 0.1$. This is referred to as *Salt and Pepper 0.1*.

The baseline condition, with which these texture variants are compared, is taking the original image with no texture at all, that is

$$T : \quad f \mapsto f, \quad (6.45)$$

abbreviated as *none* in the tables.

In Tables 6.2, 6.3, the choices for T in (6.39), (6.40), (6.45), (6.41) are compared, along with different variants to mix them with texture, specified below in (6.46), (6.47).

In Table 6.1, the results for all choices of T outlined above are compared.

6.7.4. Deformation

By forward-projecting and interpolating, we compute, for image data f , the deformed image $W(f, \mathbf{u})$, for which

$$W(f, \mathbf{u})(\mathbf{x} + \mathbf{u}(\mathbf{x})) = f(\mathbf{x})$$

holds.

6. Texture generation for photoacoustic elastography

Texture Mode	AAE	AE Eabs	AE Erel	s-warp	o-warp
none	0.1780	0.0617	2.9980	0.4886	0.4886
Gauss 0.3 SW	0.1830	0.0628	3.0553	0.5471	0.4886
Band FBP 0.4	0.0905	0.0135	0.6583	0.1285	0.1821
Band FBP 0.4 SW	0.0882	0.0141	0.6909	0.1298	0.1958
Band FBP 1.8	0.0461	0.0190	0.9233	0.0538	0.2313
Band FBP 1.8 SW	0.1217	0.0184	0.8933	0.0536	0.2313
Gauss Conv 3x3	0.1730	0.0544	2.6470	0.4722	0.4886
Gauss Conv 3x3 SW	0.1731	0.0545	2.6480	0.4723	0.4863
Aver Conv 3x3	0.1632	0.0411	1.9985	0.3997	0.4595
Aver Conv 3x3 SW	0.1641	0.0417	2.0298	0.4036	0.4613
SaltPepper 0.1	0.2036	0.0051	0.2473	0.3961	0.0715
SaltPepper 0.1 SW	0.0851	0.0196	0.9552	0.4519	0.2536

Table 6.1.: Different texture modes for Experiment 2, with 10% noise, $\lambda = 11.2202$ (see also Figure 6.6)

For computing the data for the optical flow computation, the preferred choice follows principle 6.5.2, first applying the deformation, then the texture. Therefore we set

$$f_1 = T(f)$$

as well as

$$f_2 = T(W(f, \mathbf{u})). \quad (6.46)$$

Alternatively, we compare these with violating principle 6.5.2, first applying the texture, then deforming the image:

$$f_2 = W(T(f), \mathbf{u}). \quad (6.47)$$

The latter choice will be referred to with the letters DT in Tables 6.1, 6.2, 6.3.

We also define

$$f_1^O = f(\mathbf{x}), \quad f_2^O = W(f, \mathbf{u}). \quad (6.48)$$

for the validation.

6.7.5. Optical flow computation

With f_1 and f_2 determined as above, we compute

$$\mathbf{u} = \underset{\mathbf{v}}{\operatorname{argmin}} \|\nabla Q(f_1) \cdot \mathbf{v} - (Q(f_2) - Q(f_1))\|_{L^2}^2 + \alpha \|\mathbf{v}\|_{H_0^1}. \quad (6.49)$$

Here, we apply

$$Q : f \mapsto f + r,$$

with r being additive Gaussian noise calibrated to 10 % of the maximum value of f .

This procedure has been applied to all results in Tables 6.1, 6.2 and 6.3. – The effect of noise addition to texture is studied separately for the case of Experiment 2 (see Figure 6.4).

6.7.6. Validation

The field which is computed with the optical flow algorithm should approximately match the correct motion field. In order to study how PAI and textured PAI images behave under mechanical deformations, we adopt the following validation procedure to compare the computed vector field with *ground-truth* data:

Synthetic Data verification

- Choose a particular vector field \mathbf{u}_0 , as well as a reference image f_1
- Choose a texture method T
- Compute f_1 , f_2 as in subsection 6.7.4
- Compute the optical flow $\mathbf{u}(\mathbf{x})$ as in (6.49)
- Compare the result \mathbf{u} against the ground-truth vector field \mathbf{u}_0

Error measures To compare the computed flows produced to the ground truth field, we use the angular and distance error, and to assess the prediction quality of the flow, we calculate the warping error. To define these error measures, write

$$\begin{aligned}\mathbf{u}_0(\mathbf{x}) &= r_0(\mathbf{x}) e^{i\varphi_0(\mathbf{x})} \\ \mathbf{u}(\mathbf{x}) &= r(\mathbf{x}) e^{i\varphi(\mathbf{x})}.\end{aligned}$$

Then we define the

- average angular error (AAE)

$$\int_{\Omega} |\varphi(\mathbf{x}) - \varphi_0(\mathbf{x})| d\mathbf{x}$$

- average endpoint error (AEE)

$$\int_{\Omega} \|\mathbf{u} - \mathbf{u}_0\| d\mathbf{x}$$

- average relative endpoint error (AEErel)

$$\int_{\Omega} \frac{1}{\|\mathbf{u}_0\|} \|\mathbf{u} - \mathbf{u}_0\| d\mathbf{x}$$

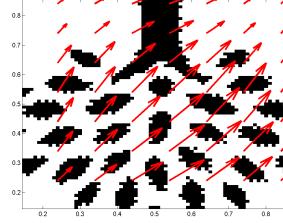
- the warping error w.r.t. the textured images (s-warp)

$$\int_{\Omega} \|f_2(\mathbf{x}) - W(f_1, \mathbf{u})\| d\mathbf{x},$$

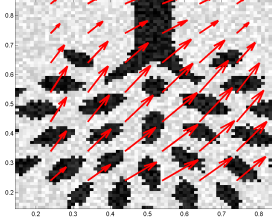
6. Texture generation for photoacoustic elastography

- the warping error w.r.t. the original images (o-warp)

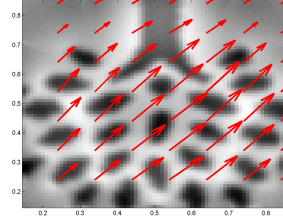
$$\int_{\Omega} \|W(f, \mathbf{u}_0)(\mathbf{x}) - W(f, \mathbf{u})\| d\mathbf{x}.$$



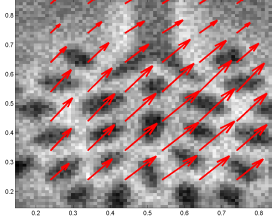
(a) none + 0% noise



(b) none + 30% noise



(c) Band 0.4 + 0% noise



(d) Band 0.4 + 30% noise

Texture Mode	AAE	AEEabs	AEErel	Warping
none + 0% noise	0.2499	0.0445	3.3232	0.3739
none + 5% noise	0.2494	0.0445	3.3233	0.3847
none + 10% noise	0.2492	0.0444	3.3199	0.3949
none + 20% noise	0.2515	0.0445	3.3229	0.4166
none + 30% noise	0.2493	0.0445	3.3270	0.4369
Band 0.4 + 0% noise	0.1880	0.0101	0.7548	0.0737
Band 0.4 + 5% noise	0.1876	0.0101	0.7546	0.0803
Band 0.4 + 10% noise	0.1883	0.0101	0.7560	0.0928
Band 0.4 + 20% noise	0.1929	0.0101	0.7583	0.1224
Band 0.4 + 30% noise	0.1825	0.0101	0.7522	0.1560

(e) Errors for $\lambda = 12.5893$

Figure 6.4.: Comparison of different noise levels in Experiment 1 (see also Figure 6.5), the average over 10 experiments has been taken

6.8. Discussion

As mentioned in the introduction, elastography often relies on speckle tracking methods, including correlation techniques and optical flow. It is clear that such

methods have a problem with homogeneous regions. As for the optical flow, this can be seen from (6.4), where the data term for homogeneous regions provides no information at all.

In Experiments 1-4, we used several pieces of synthetic data showing homogeneous regions and investigated the effect of the homogeneity in several regions of the data (see Figs. 6.5a-6.8a).

The visualization of the computed motion fields in Figs. 6.5c, 6.6c, 6.7c and 6.8c shows aberrations from the respective ground truth fields. Comparing the values for the angular, distance and warping errors in Table 6.2 to 6.3 shows these aberrations, if one restricts to the untextured original images.

We then applied the texture generation methods introduced in Section 6.5. The results in section 6.7 show that addition of texture is able to alleviate this problem of homogeneous regions to a considerable amount. The effect shows up in the different error types.

For the specimens we used, the angular error decreases about 20-30 % compared to the original error, and in extreme cases the decrease is as high as 75 % (as seen from Table 6.2). As seen from Figs. 6.5h-6.8h, where the errors were plotted as a function of the regularization parameters, the distance error reaches its minimum in the textured variant at lower regularization values than the original data. In this context, we note that the angular error is a monotonically increasing function of the regularization parameters in the cases we investigated. In some cases (as seen from Fig. 6.5h and Fig. 6.7h), the textured versions give also a lower distance error for the optimal regularization value; in other cases, with the motion estimation we used, the distance error is about the same magnitude as in the original versions.

The fact that the displacement estimation using the texture-method results in a vector field with optimum distance error at smaller regularization values (therefore also allowing a smaller angular error) points at the fact that the texture variant itself acts like a regularizer.

The optimum frequency windows for the texture generating method differ for the rigid and the non-rigid deformations we used. Whereas for the rigid deformations, the window with $\kappa_{\min} = 0.4$ gave best results, the non-rigid deformations best results with $\kappa_{\min} = 1.8$.

The possible non-commutation, which we mentioned in the Remark of Subsection 6.5.2, does not influence the result of the optical flow computations in a significant way, as seen from Tables 6.2-6.3.

The results are relatively robust to noise, as seen from Figure 6.4. While there are changes up to one tenth in the angular error, the band-pass-filtered images perform better than the original images, even with addition of 30% noise.

Notice that, in Experiments 1-4, we studied the addition of noise to a static image and then deformed it. This does not give a significant change in the accuracy of the optical flow (see Tables 6.2 and 6.3). See also Table 6.1 for other results in that direction.

6. Texture generation for photoacoustic elastography

The effect of adding texture seems to come from a filling-in-effect in the optical flow equation (6.4). Although the regularization term is responsible for such an interpolation usually, here this filling-in-effect originates from the data term; the function Ψ seems to propagate the information from within the objects out across the edges and boundaries. This seems also to alleviate the aperture problem in optical flow, as the new texture creates also new gradients around edges. This may account for the lessening of the angular error.

Overall, the results point at the phenomenon that an effect which has deteriorating the image quality in one contrast (here the photoacoustic contrast) can have an advantageous effect on another contrast (here the mechanical contrast, which is inherent in the displacement \mathbf{u}).

6.9. Conclusion

We studied the topic of texture generation in photoacoustics, and applied band-width filter techniques for generating such texture in the reconstructed images. This kind of texture was mathematically characterized. Then we tested an application of the PAI texture for elastography purposes. It turned out that the texture generation technique has the potential to fill in otherwise untextured regions. The displacements can be better measured then, making photoacoustic elastography viable.

Acknowledgements

We thank Joyce McLaughlin, Paul Beard and Ben Cox for helpful discussions and acknowledge support from the Austrian Science Fund (FWF) in projects S10505-N20 and P26687-N25.

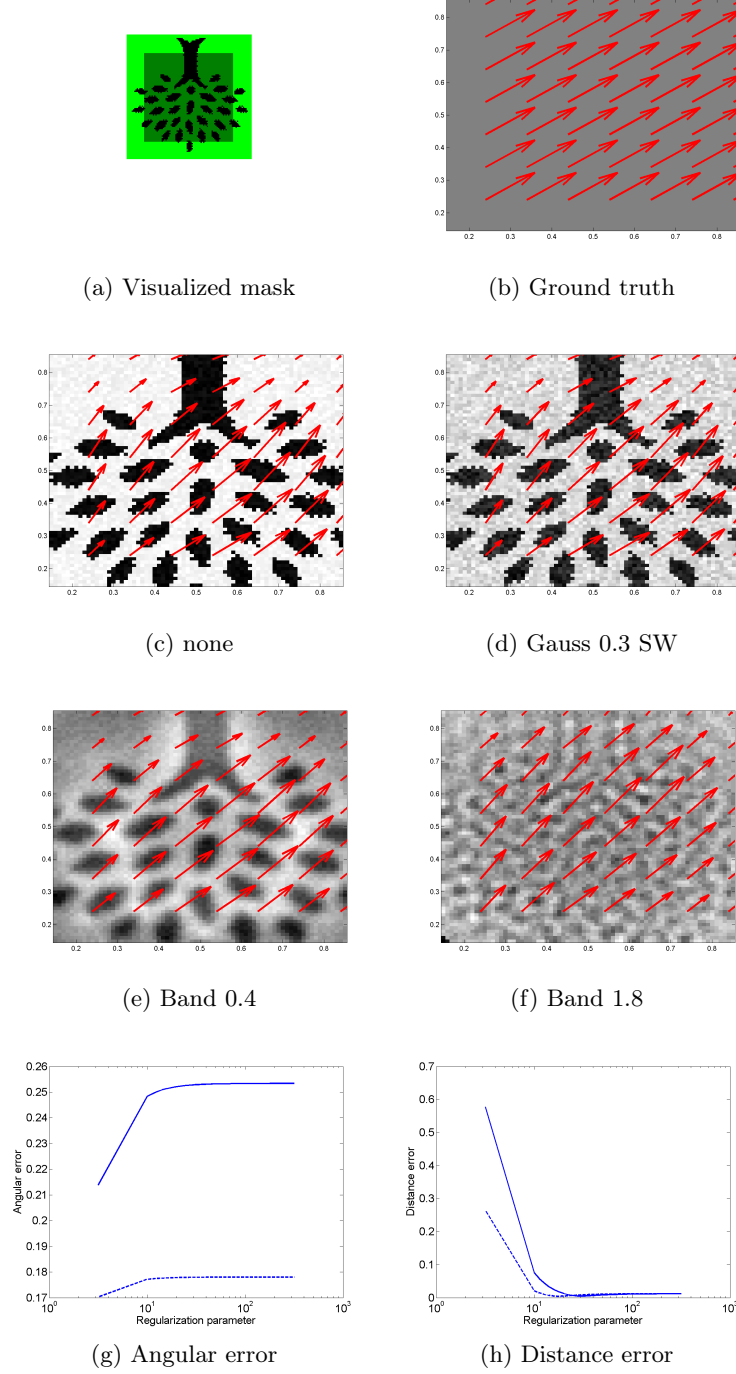


Figure 6.5.: (Experiment 1) Computed vector fields for $\lambda = 12.5893$. a Visualized mask. b Ground truth. c none. d Gauss Tex 0.3 TD. E Band 0.4 DT. f Band 1.8 DT. g-h Angular distance error measures for regularization parameter $10^{-3} \leq \lambda \leq 10^3$, full line: original data; dashed line: Band-limitation texture $\kappa_{min} = 0.4$.

6. Texture generation for photoacoustic elastography

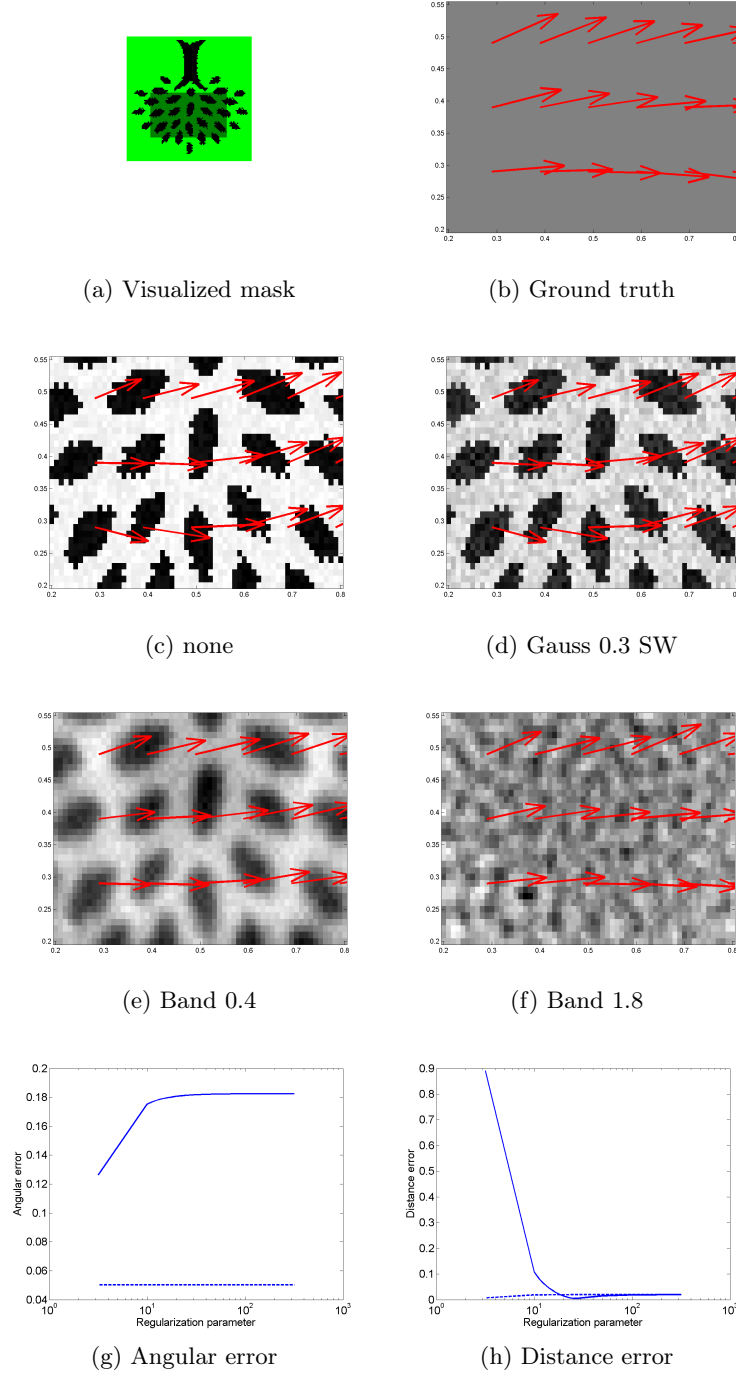


Figure 6.6.: (Experiment 2) Computed vector fields for $\lambda = 12.5893$. a Visualized mask. b Ground truth. c none. d Gauss Tex 0.3 TD. E Band 0.4 DT. f Band 1.8 DT. g-h Angular distance error measures for regularization parameter $10^{-3} \leq \lambda \leq 10^3$, full line: original data; dashed line: Band-limitation texture $\kappa_{min} = 1.8$.

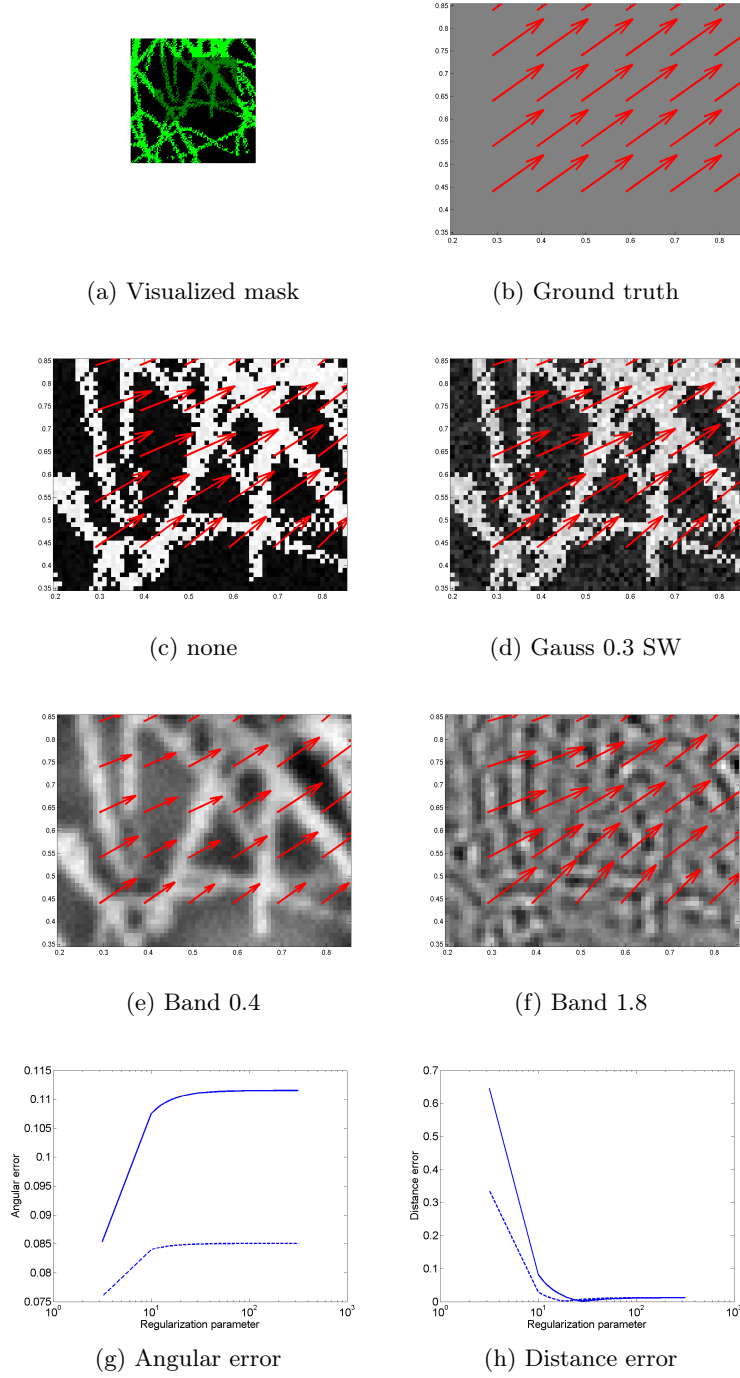


Figure 6.7.: (Experiment 3) Computed vector fields for $\lambda = 11.2202$. a Visualized mask. b Ground truth. c none. d Gauss Tex 0.3 TD. E Band 0.4 DT. f Band 1.8 DT. g-h Angular distance error measures for regularization parameter $10^{-3} \leq \lambda \leq 10^3$, full line: original data; dashed line: Band-limitation texture $\kappa_{min} = 0.4$.

6. Texture generation for photoacoustic elastography

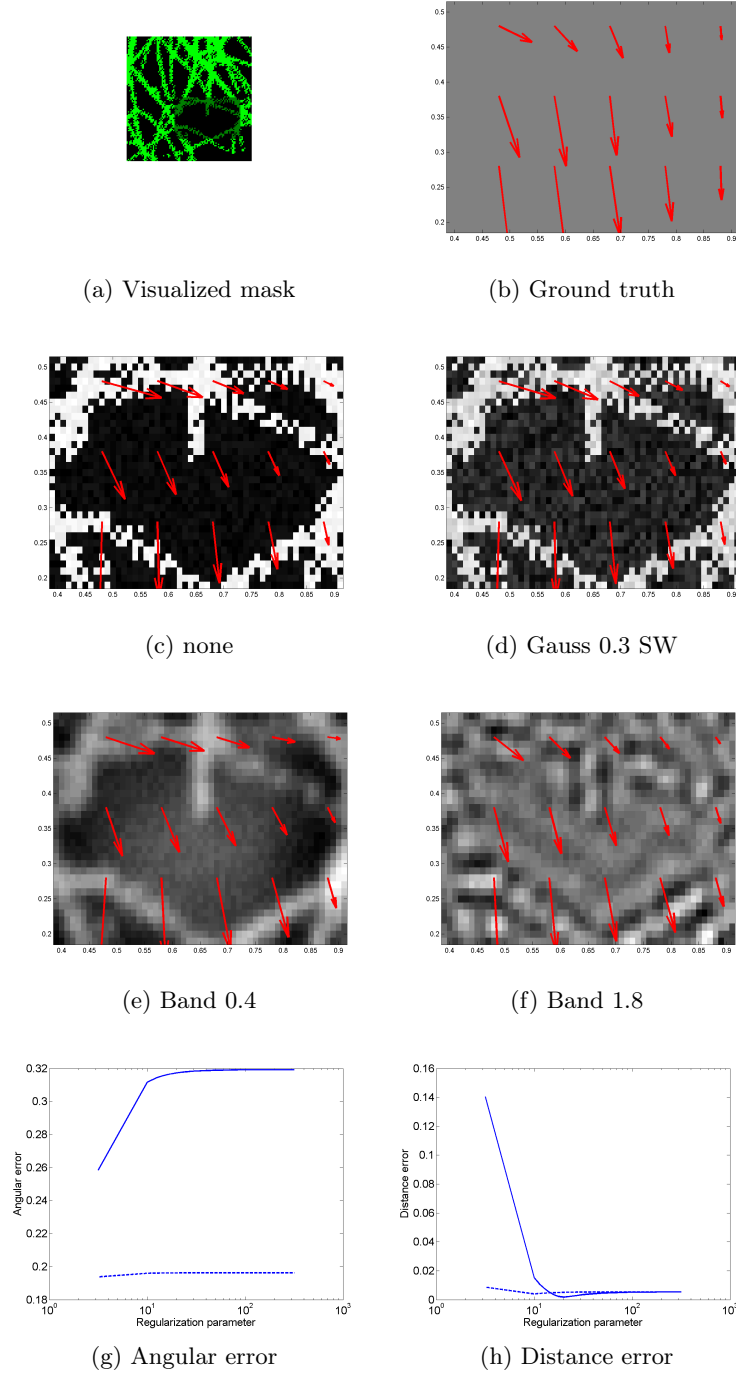


Figure 6.8.: (Experiment 4) Computed vector fields for $\lambda = 11.2202$. a Visualized mask. b Ground truth. c none. d Gauss Tex 0.3 TD. E Band 0.4 DT. f Band 1.8 DT. g-h Angular distance error measures for regularization parameter $10^{-3} \leq \lambda \leq 10^3$, full line: original data; dashed line: Band-limitation texture $\kappa_{min} = 1.8$.

Table 6.2.: Experiments 1 and 2: Error analysis

Texture Mode	AAE	AEEabs	AEErel	Warping
none	0.2499	0.0445	3.3232	0.3739
Gauss 0.3 SW	0.2429	0.0448	3.3480	0.4391
Gauss 0.1 noise	0.2500	0.0447	3.3386	0.3970
Band 0.4	0.1962	0.0105	0.7838	0.0945
Band 1.8	0.2344	0.0114	0.8531	0.0434

(a) Rigid experiment, $\lambda = 12.5893$ (see Figure 6.5)

Texture Mode	AAE	AEEabs	AEErel	Warping
none	0.1780	0.0617	2.9980	0.4886
Gauss 0.3 SW	0.1761	0.0620	3.0145	0.5393
Gauss 0.1 noise	0.1778	0.0617	3.0013	0.5060
Band 0.4	0.0913	0.0135	0.6607	0.1309
Band 1.8	0.1188	0.0190	0.9231	0.0552

(b) Non-rigid experiment, $\lambda = 12.5893$ (see Figure 6.6)

Table 6.3.: Experiments 3 and 4: Error analysis

Texture Mode	AAE	AEEabs	AEErel	Warping
none	0.1089	0.0635	4.7460	0.4382
Gauss 0.3 SW	0.1106	0.0637	4.7639	0.4991
Gauss 0.1 noise	0.1084	0.0636	4.7567	0.4580
Band 0.4	0.0805	0.0214	1.5985	0.1829
Band 1.8	0.1313	0.0093	0.6966	0.0556

(a) Rigid experiment, $\lambda = 11.2202$ (see Figure 6.7)

Texture Mode	AAE	AEEabs	AEErel	Warping
none	0.2962	0.0112	1.3676	0.2053
Gauss 0.3 SW	0.2975	0.0111	1.3577	0.2795
Gauss 0.1 noise	0.3017	0.0114	1.3969	0.2298
Band 0.4	0.3259	0.0024	0.3063	0.0388
Band 1.8	0.2128	0.0044	0.5320	0.0283

(b) Non-rigid experiment, $\lambda = 11.2202$ (see Figure 6.8)

7. Texture generation for compressional photoacoustic elastography

Authors & Contributions The authors are J. W. Schmid, B. Zabihian, TW, T. Glatz, M. Liu, W. Drexler and O. Scherzer. The development of this article was a gradual, cooperative process, and each of the authors made significant contributions to this paper, the authors from the Computational Science Center (see affiliations next page) on the modelling and algorithmic part, and the authors of the Center for Medical Physics on the experimental parts.

Publication status Published, reference [120]. The original publication is available at <http://dx.doi.org/10.1117/12.2079672>.

Abstract:

Elastography is implemented by applying a mechanical force to a specimen and visualizing the resulting displacement. As a basis of elastographic imaging typically ultrasound, optical coherence tomography or magnetic resonance imaging are used. Photoacoustics has not been viewed as a primary imaging modality for elastography, but only as a complementary method to enhance the contrast in ultrasound elastography. The reason is that photoacoustics is considered speckle free [3], which hinders application of speckle tracking algorithms. However, while conventional ultrasound only uses a single frequency, photoacoustics utilizes a broad frequency spectrum. We are therefore able to generate artificial texture by using a frequency band limited part of the recorded data. In this work we try to assess the applicability of this technique to photoacoustic tomography. We use Agar phantoms with predefined Young's moduli and laterally apply a $50\mu\text{m}$ static compression. Pre- and post compression data are recorded via a Fabry P  rot interferometer planar sensor setup and reconstructed via a non-uniform-FFT reconstruction algorithm. A displacement vector field, between pre- and post compressed data is then determined via optical flow algorithms. While the implementation of texture generation during post processing reduces image quality overall, it turns out that it improves the detection of moving patterns and is therefore better suited for elastography.

Texture generation for compressional photoacoustic elastography

J. W. Schmid^{1,2}, B. Zabihian², T. Widlak¹, T. Glatz¹, M. Liu², W.
Drexler² and O. Scherzer^{1,3}

¹ Computational Science Center, University of Vienna,
Oskar-Morgenstern-Platz 1, 1090 Vienna, Austria

² Center for Medical Physics and Biomedical Engineering, Medical University of
Vienna,

Währinger Gürtel 18-20, 1090 Vienna, Austria

³ RICAM, Austrian Academy of Sciences,
Altenberger Straße 69, 4040 Linz, Austria

Contents

7.1	INTRODUCTION	119
7.2	Experimental	120
7.3	Conclusion and Outlook	123

7.1. INTRODUCTION

Elastography is used for visualizing elastic properties of a specimen or probe. Clinical applications include the detection of skin, breast and prostate cancer, detection of liver cirrhosis, and characterization of atherosclerotic plaque in vascular imaging (see for instance [40, 106, 134]). Elastography is an *on top* imaging method: Basically, every imaging technique can be used as basis for elastographic imaging, such as ultrasound imaging (see for instance [75]), magnetic resonance imaging (see for instance [93]) or optical coherence tomography (see for instance [127]). With all these techniques, it is possible to visualize momentum images, from which mechanical displacements \mathbf{u} can be calculated, which forms the basis of clinical examinations.

For motion estimation in *ultrasound elastography (USE)*, *optical coherence elastography (OCE)* and in certain variants of *magnetic resonance elastography (MRE)*, common techniques are optical flow and motion tracking algorithms [31, 106] – in USE and OCE, these are specifically referred to as *speckle tracking algorithm*. Speckle tracking can only be realized if the imaging data contains a certain amount of correlated pattern information.

Photoacoustics has as yet not been used as underlying imaging technique for elastography, but only as supplement to enhance contrast in US-elastography [43]. This can be attributed to the weak speckle patterns in photoacoustics, which generally is considered advantageous for imaging, but makes it less suited for speckle tracking algorithms. However, recently it has been shown [52] that an artificial texture pattern can be introduced by simulating the effect of a band-limited part of the measurement data on the imaging data. In this way the artificial speckle patterns improves the deformation estimation with generic speckle tracking algorithms.

7.1.1. Speckle tracking and texture generation in photoacoustic tomography

Optical flow is the apparent motion of objects in a sequence of images. In mathematical terms it is a vector displacement $\mathbf{u} = \frac{d\mathbf{x}}{dt}$ connecting pixels of the same intensity in a movie. That is

$$f(\mathbf{x}(t); t) = \text{const} . \quad (7.1)$$

In practice the optical flow is calculated sequentially for two successive images and under the assumptions of small displacements from the optical flow equation

$$\nabla f_1 \cdot \mathbf{u} + (f_2 - f_1) = 0 , \quad (7.2)$$

which is the linearization of (7.1).

While common ultrasound imaging is operating with a fixed single frequency mode, in photoacoustics the specimen is excited with a short laser pulse, that is

7. Texture generation for compressional photoacoustic elastography

mathematically interpreted as a delta pulse. Photoacoustic reconstructions show clear cut images with large homogeneous regions. Such data are not well suited for the optical flow algorithm, which consists in determining

$$\mathbf{u}_\alpha := \operatorname{argmin}_{\mathbf{v}} \left\{ \|\nabla f_1 \cdot \mathbf{v} + (f_2 - f_1)\|_{L^2(\Omega)}^2 + \alpha \|\nabla \mathbf{v}\|_{L^2(\Omega)}^2 \right\}, \quad (7.3)$$

In homogeneous regions where $\nabla f_1 = 0$, the optical flow equation allows every flow \mathbf{u} and the optical flow method (7.3) *extrapolates* values of \mathbf{u}_α into this region, which are favored by the regularization functional $\|\nabla \mathbf{v}\|_{L^2(\Omega)}^2$. Moreover, mathematically, equation (7.2) is not well-defined if f_1 has jumps. This can be avoided by convolving the imaging data f , resulting in $f * \Psi$. With such data the optical flow algorithms becomes:

$$\mathbf{u}_\alpha := \operatorname{argmin}_{\mathbf{v}} \left\{ \|\nabla(f_1 * \Psi) \cdot \mathbf{v} + (f_2 - f_1) * \Psi\|_{L^2(\Omega)}^2 + \alpha \|\nabla \mathbf{v}\|_{L^2(\Omega)}^2 \right\}. \quad (7.4)$$

The kernel Ψ is chosen to simulate the speckle pattern of ultrasound images (see [52]) and has the form:

$$\Psi(\mathbf{x}) = \frac{\nu_{\max} J_1(\nu_{\max} |\mathbf{x}|) - \nu_{\min} J_1(\nu_{\min} |\mathbf{x}|)}{\sqrt{2\pi} |\mathbf{x}|}. \quad (7.5)$$

In particular this kernel provides the imaging data for band-filtered sensor data with band $[\nu_{\min}, \nu_{\max}]$. Here J_1 is the first-kind Bessel function of order 1.

7.2. Experimental

7.2.1. Photoacoustic Tomography System and Experiment

The photoacoustic tomography (PAT) system consists of a FP (Fabry P  rot) polymer film sensor for interrogation [28, 29]. A 50 Hz pulsed laser source and a subsequent optical parametric oscillator (OPO) provide optical pulses. The photoacoustic signal is recorded via the FP-sensor head. The sensor head consists of an approximately 38 μm thick polymer (Parylene C) which is sandwiched between two dichroic dielectric coatings. These dichroic mirrors have a noteworthy transmission characteristic. Light from 600 to 1200 nm can pass the mirrors largely unabated, whereas the reflectivity from 1500 to 1650 nm (sensor interrogation band) is about 95% [140].

The incident photoacoustic wave produces a linear change in the optical thickness of the polymer film. The light from a continuous wave laser is focused on the surface of the sensor. The laser is operating within the interrogation band and can now determine the change of thickness at the interrogation point via FP-interferometry.

7.2.2. Phantoms

Our phantoms consist of Agar with ink inclusions. The inclusions make up 12-16% of the entire sample mass and themselves contain 2.5-3% of India ink. The

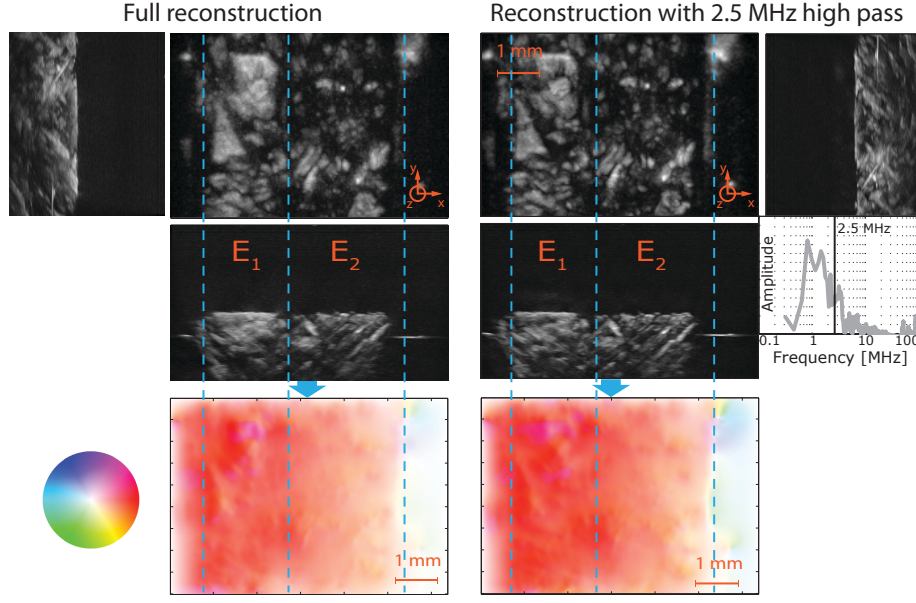


Figure 7.1.: **Top:** Maximum intensity projections (MIP) in all 3 dimensions of a single data set, reconstructed via non-uniform FFT. The left hand side shows the full reconstruction, whereas the right hand side is reconstructed using a hard band pass filter. On the right, a Fourier spectrum averaged over the two spatial dimensions is shown. The hard high pass filter at 2.5 MHz for the reconstruction is marked. **Bottom:** Color wheel encoded optical flow vector fields, derived via the maximum intensity projection in the xy -plane. This is an average over 6 consecutive measurements with a displacement of $50 \mu\text{m}$. The abating displacement towards the right can be seen. Also the band limited derived map is more homogeneous. The color shows the direction of the optical flow, the intensity the vector length.

inclusions are below 1 mm in diameter and have the same agar concentration as the rest of the sample. All proportions are according to mass and are determined via an electronic scale with milligram increments.

One slab with 1% agar and one with 1.97% agar have been created. These samples are wedged into a vice which consisted of a modified translation stage, with increments of $10 \mu\text{m}$. This is then mounted onto the PAT system, where one jaw is fixed, while the other can move freely in the x -axis.

7.2.3. Evaluation

The two samples have been squeezed consecutively 6 times in $50 \mu\text{m}$ steps and recorded. The step size of the data acquisition was $60 \mu\text{m}$ and the field of view $6.36 \times 6.36 \text{ mm}$. The acquisition time was 250 seconds. The sample was constantly

7. Texture generation for compressional photoacoustic elastography

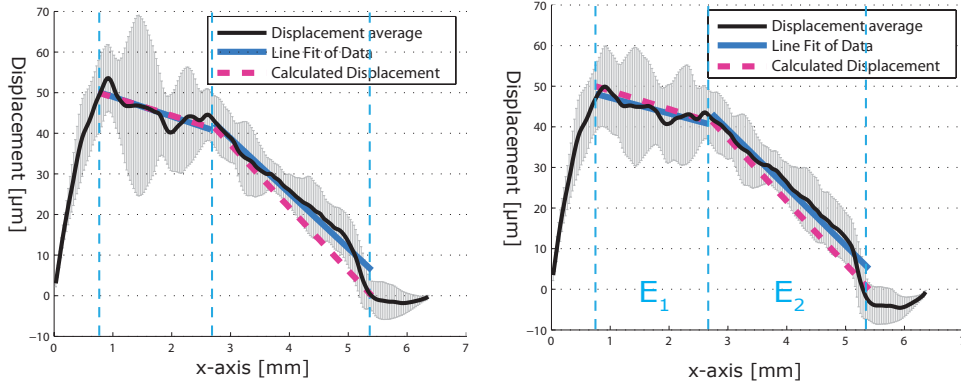


Figure 7.2.: Mean Displacements averaged over 6 measurements and along the y -axis. The blue lines are weighted linear fits over the two regions with previously known thicknesses. The dashed magenta lines are the calculated ideal displacement as shown in table 7.1.t The left hand side shows the results for the full data, whereas on the right hand side the results for the band limited reconstruction, with added texture are shown. The error bars on the right are significantly smaller than on the left.

moisturized during acquisition to prevent the phantom from drying out. The reconstruction was undertaken with a non-uniform FFT reconstruction algorithm [119, 122] using an upsampling factor of 2. From the final reconstruction 2.16 mm of the y -axis had to be cropped, since the sample ended there. Fig.7.1 shows the resulting MIPs. On the left hand side the full reconstruction is shown, whereas on the right hand side a hard Bandpass of 2.5 MHz has been used. The optical flow is calculated using a regularization parameter of $\alpha = 0.15$. This parameter was determined using a warping function which would minimize the L^2 -norm between f_1 warped with the optical flow data and f_2 .

A color coded optical flow map, averaged over all 6 measurements, is shown at the bottom of Fig.7.1. Here the abating of the signal, towards the right jaw can be seen. Also the high pass limited reconstruction map is more homogeneous.

7.2.4. Quantitative Evaluation

For a quantitative analysis we average all x -axis displacements along the y -axis and over the 6 displacement maps. Using the values of the reduced Young's modulus provided by [96] and shown in Table 7.1, for our 1% and 2% concentration sample. Additionally we use the overall displacement $D_o=50\mu\text{m}$ and derive the thickness of the regions ℓ_1 and ℓ_2 from the measured data. In our case we are able to use a simple mechanical spring model in which the stress is proportional to the relative change in thickness and given by Young's modulus: $\sigma = E \frac{dD}{dx}$. We define W as the work per unit area which we want to minimize: $W = \sigma \frac{dy}{dt} = E \left(\frac{dD}{dt} \right)^2$.

7.3. Conclusion and Outlook

	Young's modulus (kPa)	Calculated slope ($\mu\text{m}/\text{mm}$)	2.5 MHz reconstruction slope ($\mu\text{m}/\text{mm}$)	Full reconstruction slope ($\mu\text{m}/\text{mm}$)
Region 1 (2%)	327	5.4	3.7	4.8
Region 2 (1%)	95	18.5	14.4	13.7
Region2/Region1		3.42	3.86	2.85

Table 7.1.: In Column 3 the theoretically calculated slope of the displacement curve, using the values for E from [3] are shown. In column 4 and 5 the slope of the line fit from the data for a full reconstruction and a high pass limited reconstruction (added texture) is shown.

Our boundary condition is: $\ell_1 \frac{dD}{dx} + \ell_2 \frac{dD}{dx} = D_o$. Using this we are able to derive the slope of the two regions: $\frac{dD_1}{dx} = \frac{D_o E_2}{E_1 \ell_2 + E_2 \ell_1}$ and $\frac{dD_2}{dx} = \frac{D_o E_2}{E_1 \ell_2 + E_2 \ell_1}$.

These quantitative results are compared to line fits as can be seen in Fig. 7.2. The line fits and the results are compared in Table 7.1.

7.3. Conclusion and Outlook

We were able to show that quantitative elastography via photoacoustics is feasible and can give reliable results for rather small differences in Young's modulus (factor 3) and very small displacements. Further the minimum displacement resolution is well below the opto-acoustical resolution of the system and reaches up to few μm . The speckle free nature of photoacoustic and its adverse effect on the application on photoacoustic elastography could be ameliorated by generating artificial texture, which made the optical flow algorithm more reliable and reduced the variance of the measurements. In the future we will try to automatize our system and conduct a precise characterization and error analysis. Additionally a qualitative strain map of biological tissue is planned with this setup.

Acknowledgements

This work has been funded by the Austrian Science Fund (FWF) within the Project P26687 - "Interdisciplinary Coupled Physic Imaging" and the European project FAMOS (FP7 ICT 317744). Many thanks to José A. Iglesias and Boris Hermann for helpful discussions

Part III.

Appendix

Bibliography

- [1] R. A. Adams. *Sobolev Spaces*. Academic Press, New York, 1975.
- [2] R. A. Adams and Fournier J. J. F. *Sobolev Spaces*. Pure and Applied Mathematics. Elsevier, Amsterdam, 2 edition, 2003.
- [3] A. Adler, R. Gaburro, and W. Lionheart. Electrical impedance tomography. In O. Scherzer, editor, *[117]*, pages 599–652. Springer, 2011.
- [4] S. R. Aglyamov and A. R. Skovoroda. Mechanical properties of soft biological tissues. *Biophysics*, 45(6):1103–1111, 2000.
- [5] M. S. Agranovich. Elliptic singular integro-differential operators. *Russ. Math. Surv.*, 20(5):1–121, 1965.
- [6] M. Agranovsky, C. Berenstein, and P. Kuchment. Approximation by spherical waves in L^p -spaces. *J. Geom. Anal.*, 6(3):365–383, 1996.
- [7] F. Aigner, L. Pallwein, M. Schocke, A. Lebovici, D. Junker, G. Schäfer, F. Pedross, W. Horninger, W. Jaschke, E. J. Hallpern, and F. Frauscher. Comparison of real-time sonoelastography with T2-weighted endorectal magnetic resonance imaging for prostate cancer detection. *J. Ultrasound Med.*, 30:643–649, 2011.
- [8] A. Ammari, H. Waters and H. Zhang. Stability analysis for magnetic resonance elastography. Preprint, ENS, 2014. <http://arxiv.org/abs/1409.5138v1>.
- [9] H. Ammari. *An Introduction to Mathematics of Emerging Biomedical Imaging*. Mathématiques & Applications. Springer, 2008.
- [10] H. Ammari, E. Bretin, J. Garnier, H. Kang, H. Lee, and A. Wahab. *Mathematical Methods in Elasticity Imaging*. Princeton Series in Applied Mathematics. Princeton University Press, 2015.
- [11] H. Ammari, P. Garapon, and F. Jouve. Separation of scales in elasticity imaging: a numerical study. *J. Comput. Math.*, 28:354–370, 2010.
- [12] H. Ammari, P. Garapon, H. Kang, and H. Lee. A method of biological tissues elasticity reconstruction using magnetic resonance elastography measurements. *Quart. Appl. Math.*, 66:139–176, 2008.

Bibliography

- [13] H. Ammari, L. Giovangigli, Nguyen L. H., and J.-K. Seo. Admittivity imaging from multi-frequency micro-electrical impedance tomography. Preprint, ENS, 2014. <http://arxiv.org/abs/1403.5708v1>.
- [14] S. Arridge and O Scherzer. Imaging from coupled physics. *Inverse Probl.*, 28(8):080201, 2012.
- [15] S. Arridge and J. Schotland. Optical tomography: forward and inverse problems. *Inverse Probl.*, 25:123010, 2009.
- [16] G. Bal. Hybrid inverse problems and internal functionals. In G. Uhlmann, editor, *[117]*, pages 325–368. Cambridge University Press, 2012.
- [17] G. Bal. Hybrid inverse problems and systems of partial differential equations. *arXiv*, arXiv:1210.0265, 2012. To appear in: *Contemporary Mathematics*.
- [18] G. Bal. Hybrid inverse problems and systems of partial differential equations. In *Inverse Problems and Applications*, volume 615 of *Contemporary Mathematics*, pages 15–48. American Mathematical Society, 2014.
- [19] G. Bal, C. Bellis, S. Imperiale, and F. Monard. Reconstruction of constitutive parameters in isotropic linear elasticity from noisy full-field measurements. *arXiv*, arXiv:1310.5131v1, 2013.
- [20] G. Bal, C. Bellis, S. Imperiale, and F. Monard. Reconstruction of constitutive parameters in isotropic linear elasticity from noisy full-field measurements. *Inverse Probl.*, 30(12):125004, 2013.
- [21] G. Bal, K. Hoffmann, and K. Knudsen. On the propagation of singularities for a class of linearised hybrid inverse problems. Work in preparation, Technical University of Denmark, 2014.
- [22] G. Bal and S. Moskow. Local inversions in ultrasound modulated optical tomography. *Inverse Probl.*, 30:025005, 2014.
- [23] G. Bal, W. Naetar, O. Scherzer, and J. Schotland. The Levenberg-Marquardt iteration for numerical inversion of the power density operator. *J. Inverse Ill-Posed Probl.*, 21(2):265–280, February 2013.
- [24] P. E. Barbone and J. C. Bamber. Quantitative elasticity imaging: What can and cannot be inferred from strain images. *Phys. Med. Biol.*, 47:2147–2164, 2002.
- [25] P. E. Barbone and N. H. Gokhale. Elastic modulus imaging: on the uniqueness and nonuniqueness of the elastography inverse problem in two dimensions. *Inverse Probl.*, 20(4):283–296, 2004.

- [26] P. E. Barbone and A. A. Oberai. Elastic modulus imaging: some exact solutions of the compressible elastography inverse problem. *Phys. Med. Biol.*, 52(6):1577–1593, 2007.
- [27] P. Beard. Biomedical photoacoustic imaging. *Interface Focus*, 1:602–631, 2011.
- [28] P.C. Beard. Two-dimensional ultrasound receive array using an angle-tuned fabry-perot polymer film sensor for transducer field characterization and transmission ultrasound imaging. *IEEE Trans. Ultrason., Ferroelectr., Freq. Control*, 52(6):1002–1012, June 2005.
- [29] P.C. Beard, F. Perennes, and T.N. Mills. Transduction mechanisms of the fabry-perot polymer film sensing concept for wideband ultrasound detection. *IEEE Trans. Ultrason., Ferroelectr., Freq. Control*, 46(6):1575–1582, November 1999.
- [30] R. Biswas, P. Patel, D. W. Park, T. J. Cichonski, M. S. Richards, J. M. Rubin, J. Hamilton, and W. F. Weitzel. Venous elastography: validation of a novel high-resolution ultrasound method for measuring vein compliance using finite element analysis. *Sem. Dial.*, 23(1):105–109, 2010.
- [31] L. N. Bohs, B. J. Geiman, M. E. Anderson, S. C. Gebhart, and G. E. Trahey. Speckle tracking for multi-dimensional flow estimation. *Ultrason.*, 38:369–375, 2000.
- [32] M. Bonnet and A. Constantinescu. Inverse problems in elasticity. *Inverse Probl.*, 21:R1–R50, 2005.
- [33] A. Bruhn, C. Schnoerr, and J. Weickert. Lucas/Canade meets Horn/Schunck: Combining local and global optic flow methods. *Int. J. Comput. Vision*, 61(3):211–231, 2005.
- [34] G. Chavent. *Nonlinear Least Squares for Inverse Problems*. Springer, Dordrecht, 2009.
- [35] G. Chavent and K. Kunisch. On weakly nonlinear inverse problems. *SIAM J. Appl. Math.*, 56(2):542–572, 1996.
- [36] P. G. Ciarlet. *Mathematical elasticity, volume I: Three-dimensional elasticity*, volume 20 of *Mathematics and its Applications*. North-Holland, Amsterdam, 1988.
- [37] J. B. Conway. *A Course in Functional Analysis. 2nd ed.*, volume 96 of *Graduate Texts in Mathematics*. Springer Verlag, New York, Berlin, Heidelberg, 1990.

Bibliography

- [38] R. Dautray and J.-L. Lions. *Mathematical analysis and numerical methods for science and technology. Volume 5*. Springer-Verlag, Berlin, 2000. Evolution problems I.
- [39] A. Douglis and L. Nirenberg. Interior estimates for elliptic systems of partial differential equations. *Comm. Pure Appl. Math.*, 8:503–508, 1955.
- [40] M. M. Doyley. Model-based elastography: a survey of approaches to the inverse elasticity problem. *Phys. Med. Biol.*, 57:R35–R73, 2012.
- [41] P. Dular, C. Geuzaine, F. Henrotte, and W. Legros. A general environment for the treatment of discrete problems and its application to the finite element method. *IEEE Trans. Magn.*, 34(5):3395–3398, 1998.
- [42] P. Elbau, O. Scherzer, and R. Schulze. Reconstruction formulas for photoacoustic sectional imaging. *Inverse Probl.*, 28(4):045004, 2012.
- [43] S. Y. Emelianov, S. R. Aglyamov, J. Shah, S. Sethuraman, W. G. Scott, R. Schmitt, M. Motamedi, A. Karpouk, and A. Oraevsky. Combined ultrasound, optoacoustic and elasticity imaging. *Proc. SPIE*, 5320:101–12, 2004.
- [44] H. W. Engl, M. Hanke, and A. Neubauer. *Regularization of inverse problems*, volume 375 of *Mathematics and its Applications*. Kluwer Academic Publishers Group, Dordrecht, 1996.
- [45] L. C. Evans. *Partial Differential Equations*, volume 19 of *Graduate Studies in Mathematics*. American Mathematical Society, Providence, RI, 1998.
- [46] J. A. Fawcett. Inversion of n -dimensional spherical averages. *SIAM J. Appl. Math.*, 45(2):336–341, 1985.
- [47] D. Finch, M. Haltmeier, and Rakesh. Inversion of spherical means and the wave equation in even dimensions. *SIAM J. Appl. Math.*, 68(2):392–412, 2007.
- [48] D. Finch and Rakesh. Trace identities for solutions of the wave equation with initial data supported in a ball. *Math. Methods Appl. Sci.*, 28:1897–1917, 2005.
- [49] Y. B. Fu, C. K. Chui, C. L. Teo, and E. Kobayashi. Motion tracking and strain map computation from quasi-static magnetic resonance elastography. In B. Fichtinger, A. Martel, and T. Peters, editors, *Medical Image Computing and Computer-Assisted Intervention MICCAI 2011*, volume 6891 of *Lecture Notes in Computer Science*, pages 428–435. Springer, 2011.
- [50] C. Geuzaine and J.-F. Remacle. Gmsh: a three-dimensional finite element mesh generator with built-in pre- and post-processing facilities. *Numer. Meth. in Engineering*, 79(11):1309–1331, 2009.

- [51] D. Gilbarg and N. Trudinger. *Elliptic Partial Differential Equations of Second Order*. Classics in Mathematics. Springer Verlag, Berlin, 2001. Reprint of the 1998 edition.
- [52] T. Glatz, O. Scherzer, and T. Widlak. Texture generation for photoacoustic elastography. *arXiv*, arXiv:1407.6982, 2014.
- [53] T. Glatz, O. Scherzer, and T. Widlak. Texture generation for photoacoustic elastography. *J. Math. Imaging Vision*, 2015.
- [54] N. H. Gokhale, P. E. Barbone, and A. A. Oberai. Solution of the nonlinear elasticity imaging inverse problem: the compressible case. *Inverse Probl.*, 24(8):045010, 2008.
- [55] E. M. Haacke, R. W. Brown, M. R. Thompson, and R. Venkatesan. *Magnetic Resonance Imaging: Physical Principles and Sequence Design*. Wiley, New York, 1999.
- [56] M. Haltmeier. A mollification approach for inverting the spherical mean Radon transform. *SIAM J. Appl. Math.*, 71(5):1637–1652, 2011.
- [57] M. Haltmeier, O. Scherzer, and G. Zangerl. Influence of detector bandwidth and detector size to the resolution of photoacoustic tomography. In F. Breiteneker and I. Troch, editors, *Argesim Report no. 35: Proceedings Mathmod 09 Vienna*, pages 1736–1744, 2009.
- [58] M. Haltmeier and G. Zangerl. Spatial resolution in photoacoustic tomography: effects of detector size and detector bandwidth. *Inverse Probl.*, 26(12):125002, 2010.
- [59] M. Hanke. A regularizing Levenberg–Marquardt scheme, with applications to inverse groundwater filtration problems. *Inverse Probl.*, 13(1):79–95, 1997.
- [60] S. Helgason. *Integral Geometry and Radon Transform*. Springer, New York, NY, 2011.
- [61] B. K. P. Horn and B. G. Schunck. Determining optical flow. *Artificial Intelligence*, 17:185–203, 1981.
- [62] Ledesma-Carbayo M. J., J. Kybic, M. Desco, A. Santos, M. Sühling, P. Hunziker, and M. Unser. Spatio-temporal nonrigid registration for ultrasound cardiac motion estimation. *IEEE Trans. Med. Imag.*, 24(9):1113–1126, 2005.
- [63] L. Ji and J. McLaughlin. Recovery of the Lamé parameter μ in biological tissues. *Inverse Probl.*, 20:1–24, 2004.

Bibliography

- [64] B. Kaltenbacher, A. Neubauer, and O. Scherzer. *Iterative regularization methods for nonlinear ill-posed problems*, volume 6 of *Radon Series on Computational and Applied Mathematics*. Walter de Gruyter GmbH & Co. KG, Berlin, 2008.
- [65] A. S. Khalil, R. C. Chan, A. H. Chau, B. E. Bouma, and M. R. K. Mofrad. Tissue elasticity estimation with optical coherence elastography: toward mechanical characterization of *in vivo* soft tissue. *Ann. Biomed. Eng.*, 33:1631–1639, 2005.
- [66] S. G. Krein. *Linear Equations in a Banach Space*. Birkhäuser, Boston, 1982.
- [67] T. A. Krouskop, T. M. Wheeler, F. Kallel, B. S. Garra, and T. Hall. Elastic moduli of breast and prostate tissues under compression. *Ultrason. Imaging*, 20:260–274, 1998.
- [68] P. Kuchment. Mathematics of hybrid imaging: a brief review. In I. Sabadini and D. C. Struppa, editors, *The Mathematical Legacy of Leon Ehrenpreis*, pages 183–208, Berlin, 2012. Springer.
- [69] P. Kuchment and L. Kunyansky. Mathematics of thermoacoustic tomography. *European J. Appl. Math.*, 19:191–224, 2008.
- [70] P. Kuchment and L. Kunyansky. Mathematics of photoacoustic and thermoacoustic tomography. In O. Scherzer, editor, *[117]*, pages 817–867. Springer, 2011.
- [71] P. Kuchment and D. Steinhauer. Stabilizing inverse problems by internal data. *Inverse Probl.*, 28(8):084007, 2012.
- [72] P. Kuchment and D. Steinhauer. Stabilizing inverse problems by internal data II. non-local internal data and generic linearized uniqueness. Preprint, Texas A&M University, 2014. <http://arxiv.org/abs/1407.0763>.
- [73] L. D. Kudrayavtsev. Implicit function. In M. Hazewinkel, editor, *Encyclopedia of Mathematics*. Springer, 2001.
- [74] D. Lecompte, A. Smits, S. Bussuyt, H. Sol, H. Vantomme, D. Van Hemelrijck, and A. M. Habraken. Quality assessment of speckle patterns for digital image correlation. *Opt. Laser Eng.*, 44(11):1132–1145, 2006.
- [75] R. M. Lerner, K. J. Parker, J. Holen, R. Gramiak, and R. C. Waag. Sonoelasticity: medical elasticity images derived from ultrasound signals in mechanically vibrated targets. *Acoust. Imaging*, 16:317–327, 1988.
- [76] M. Levy, H. E. Bass, and R. R. Stern. *Handbook of Elastic Properties of Solids, Liquids, and Gases. Volume III: Elastic Properties of Solids:*

Biological and Organic Materials, Earth and Marine Sciences. Academic Press, 2001.

- [77] C. Li and L. V. Wang. Photoacoustic tomography and sensing in biomedicine. *Phys. Med. Biol.*, 54:R59–R97, 2009.
- [78] L. Li and L. V. Wang. Speckle in photoacoustic tomography. *Proc. SPIE*, 6095:60860Y, 2006.
- [79] A. E. H. Love. *A Treatise on the mathematical theory of elasticity*. Dover, New York, 1944.
- [80] N. Mandache. Exponential instability in an inverse problem for the schrödinger equation. *Inverse Probl.*, 17:1435–1444, 2001.
- [81] A. Manduca, T. E. Oliphant, M. A. Dresner, J. L. Mahowald, S. A. Kruse, E. Amromin, J. P. Felmlee, J. F. Greenleaf, and R. L. Ehman. Magnetic resonance elastography: Non-invasive mapping of tissue elasticity. *Med. Image Anal.*, 5:237–354, 2001.
- [82] A. McLaughlin, J. Oberai and J.-R. Yoon. Formulas for detecting a spherical stiff inclusion from interior data: a sensitivity analysis for the Helmholtz equation. *Inverse Probl.*, 28:084004, 2012.
- [83] J. McLaughlin and D. Renzi. Shear wave speed recovery in transient elastography and supersonic imaging using propagating fronts. *Inverse Probl.*, 22:681–706, 2006.
- [84] J. McLaughlin and D. Renzi. Using level set based inversion of arrival times to recover shear wave speed in transient elastography and supersonic imaging. *Inverse Probl.*, 22:707–725, 2006.
- [85] J. McLaughlin, D. Renzi, K. Parker, and Z. Wu. Shear wave speed recovery using moving interference patterns obtained in sonoelastography experiments. *J. Acoust. Soc. Amer.*, 121(4):2438–2446, 2007.
- [86] J. McLaughlin, A. Thomas, and J.-R. Yoon. Basic theory for generalized linear solid viscoelastic models. In G. Bal, D. Finch, P. Kuchment, J. Schotland, P. Stefanov, and G. Uhlmann, editors, *Tomography and Inverse Transport Theory*, volume 559 of *Contemp. Math.*, pages 101–134, Providence, RI, 2011. Amer. Math. Soc.
- [87] J. McLaughlin and J.-R. Yoon. Unique identifiability of elastic parameters from time-dependent interior displacement measurement. *Inverse Probl.*, 20:25–45, 2004.
- [88] J. McLaughlin, N. Zhang, and A. Manduca. Calculating tissue shear modulus and pressure by 2D log-elastographic methods. *Inverse Probl.*, 26:085007, 2010.

Bibliography

- [89] J. Modersitzki. *Numerical Methods for Image Registration*. Oxford University Press, New York, 2003.
- [90] C. Montalto and P. Stefanov. Stability of coupled-physics inverse problems with one internal measurement. *Inverse Probl.*, 29(12):125004, 2013.
- [91] V. A. Morozov. *Methods for Solving Incorrectly Posed Problems*. Springer, New York, Berlin, Heidelberg, 1984.
- [92] J. R. Munkres. *Topology*. Prentice Hall, Upper Saddle River, NJ, 2 edition, 2000.
- [93] R. Muthupillai, D. J. Lomas, P. J. Rossman, J. F. Greenleaf, A. Manduca, and R. L. Ehman. Magnetic resonance elastography by direct visualization of propagating acoustic strain waves. *Science*, 269:1854–1857, 1995.
- [94] A. Nahas, M. Bauer, S. Roux, and A. C. Boccara. 3D static elastography at the micrometer scale using Full Field OCT. *Biomed. Opt. Express*, 4(10):2138–2149, 2013.
- [95] F. Natterer and F. Wübbeling. *Mathematical Methods in Image Reconstruction*, volume 5 of *Monographs on Mathematical Modeling and Computation*. SIAM, Philadelphia, PA, 2001.
- [96] V.T. Nayar, J.D. Weiland, C.S. Nelson, and A.M. Hodge. Elastic and viscoelastic characterization of agar. *Journal of the Mechanical Behavior of Biomedical Materials*, 7:60–68, 2012.
- [97] S. Nilsson. *Application of Fast Backprojection Techniques for Some Inverse Problems of Integral Geometry*. PhD thesis, Linköping University, Dept. of Mathematics, 1997.
- [98] S. J. Norton. Reconstruction of a two-dimensional reflecting medium over a circular domain: Exact solution. *J. Acoust. Soc. Amer.*, 67(4):1266–1273, 1980.
- [99] S. J. Norton and M. Linzer. Ultrasonic reflectivity imaging in three dimensions: Exact inverse scattering solutions for plane, cylindrical and spherical apertures. *IEEE Trans. Biomed. Eng.*, 28(2):202–220, 1981.
- [100] R. Nuster, P. Slezak, and G. Paltauf. Imaging of blood vessels with CCD-camera based three-dimensional photoacoustic tomography. *Proc. SPIE*, 8943:894357, 2014.
- [101] A. A. Oberai, N. H. Gokhale, and G. R. Feijoo. Solution of inverse problems in elasticity imaging using the adjoint method. *Inverse Probl.*, 19:297–313, 2003.

- [102] M. O'Donnel, A.R. Skovoroda, B.M. Shapo, and S.Y. Emelianov. Internal displacement and strain imaging using ultrasonic speckle tracking. *IEEE Trans. Son. Ultrason.*, 41:314–325, 1994.
- [103] J. Ophir, I. Cespedes, H. Ponnekanti, Y. Yazdi, and X. Li. Elastography: a quantitative method for imaging the elasticity of biological tissues. *Ultrason. Imaging*, 13:111–134, 1991.
- [104] V. P. Palamodov. *Reconstructive Integral Geometry*, volume 98 of *Mono-graphs in Mathematics*. Birkhäuser Verlag, Basel, 2004.
- [105] X. Pan, J. Gao, S. Tao, K. Liu, J. Bai, and J. Luo. A two-step optical flow method for strain estimation in elastography: simulation and phantom study. *Ultrasons*, 54:990–996, 2014.
- [106] K. J. Parker, M. M. Doyley, and D. J. Rubens. Imaging the elastic properties of tissue: the 20 year perspective. *Phys. Med. Biol.*, 56:R1–R29, 2011.
- [107] K. J. Parker and R. M. Lerner. Sonoelasticity of organs: shear waves ring a bell. *J. Ultrasound Med.*, 11:387–392, 1992.
- [108] K. J. Parker, L. S. Taylor, S. Gracewski, and D. J. Rubens. A unified view of imaging the elastic properties of tissue. *J. Acoust. Soc. Amer.*, 117(5):2705–2712, 2005.
- [109] P. R. Prasad and S. Bhattacharya. Improvements in speckle tracking algorithms for vibrational analysis using optical coherence tomography. *J. Biomed. Opt.*, 18(4):18, 2014.
- [110] J. L. Prince and E. R. McVeigh. Motion estimation from tagged MR image sequences. *IEEE Trans. Med. Imag.*, 11(2):238–249, 1992.
- [111] K. R. Raghavan and A. E. Yagle. Forward and inverse problems in elasticity imaging of soft-tissues. *IEEE Trans. Nucl. Sci.*, 41:1639–1648, 1994.
- [112] A.G. Ramm. Inversion of the backscattering data and a problem of integral geometry. *Phys. Lett. A*, 113:172–176, 1985.
- [113] J. Revell, M. Mirmehdi, and D. McNally. Computer vision elastography: speckle adaptive motion estimation for elastography using ultrasound sequences. *IEEE Trans. Med. Imag.*, 24(6):755–766, 2005.
- [114] E. Rodrigues Ferreira, A. A. Oberai, and P. E. Barbone. Uniqueness of the elastography inverse problem for incompressible nonlinear planar hyperelasticity. *Inverse Probl.*, 28(12):065008, 2012.

Bibliography

- [115] A. Samani, J. Zubovits, and D. Plewes. Elastic moduli of normal and pathological human breast tissues: an inversion-technique-based investigation of 159 samples. *Phys. Med. Biol.*, 52:1565–1576, 2007.
- [116] A. P. Sarvazyan, A. R. Skovoroda, S. Y. Emelianov, L. B. Fowlkes, J. G. Pipe, R. S. Adler, R. B. Buxton, and P. L. Carson. Biophysical bases of elasticity imaging. *Acoust. Imaging*, 21:223–240, 1995.
- [117] O. Scherzer, editor. *Handbook of Mathematical Methods in Imaging*. Springer, New York, 2011.
- [118] O. Scherzer, M. Grasmair, H. Grossauer, M. Haltmeier, and F. Lenzen. *Variational methods in imaging*, volume 167 of *Applied Mathematical Sciences*. Springer, New York, 2009.
- [119] J. Schmid, T. Glatz, B. Zabihian, W. Liu, M. Drexler, and O. Scherzer. Computational realization of a non-equidistant grid sampling in photoacoustics with a non-uniform fft. *arXiv*, arXiv:1501.02946, 2015.
- [120] J. Schmid, B. Zabihian, T. Widlak, T. Glatz, M. Liu, W. Drexler, and O. Scherzer. Texture generation in compressional photoacoustic elastography. In *Photons Plus Ultrasound: Imaging and Sensing 2015*, volume 9323–100 of *Proceedings of SPIE*, 2015.
- [121] J. M. Schmitt. OCT elastography: imaging microscopic deformation and strain of tissue. *Opt. Express*, 3(6):199–211, 1998.
- [122] R. Schulze, G. Zangerl, M. Holotta, D. Meyer, F. Handle, R. Nuster, G. Paltauf, and O. Scherzer. On the use of frequency-domain reconstruction algorithms for photoacoustic imaging. *J. Biomed. Opt.*, 16(8):086002, 2011.
- [123] L. A. Segal. *Mathematics Applied to Continuum Mechanics*. MacMillan Publishing, London, 1977.
- [124] M. M. Sette, P. Goethals, J. D’hooge, H. Van Brussel, and J. V. Sloten. Algorithms for ultrasound elastography: a survey. *Comput. Methods Biomech. Biomed. Engin.*, 14(3):283–292, 2011.
- [125] D. C. Solomon. Asymptotic formulas for the dual Radon transform and applications. *Math. Z.*, 195(3):321–343, 1987.
- [126] V. A. Solonnikov. Overdetermined elliptic boundary-value problems. *J. Sov. Math.*, 1(4):477–512, 1973.
- [127] C. Sun, B. Standish, and V. X. D. Yang. Optical coherence elastography, current status and future applications. *J. Biomed. Opt.*, 16(4):043001, 2011.

- [128] L. S. Taylor, D. J. Rubens, and K. J. Parker. Artifacts and artifact reduction in sonoelastography. In S. C. Schneider, M. Leva, and B. R. McAvoy, editors, *Proceedings of the IEEE Ultrasonics Symposium*, volume 2, pages 1849–1852, New York, 2000. IEEE.
- [129] B. E. Treeby and B. T. Cox. K-Wave: MATLAB toolbox for the simulation and reconstruction of photoacoustic wave fields. *J. Biomed. Opt.*, 15:021314, 2010.
- [130] E. E. W. Van Houten, K. D. Paulsen, M. I. Miga, F. E. Kenney, and J. B. Weaver. An overlapping subzone technique for MR-based elastic property reconstruction. *Magn. Reson. Med.*, 42:779–786, 1999.
- [131] J. N. Wall, P. Olsson, and E. E. W. van Houten. On an inverse problem from magnetic resonance elastic imaging. *SIAM J. Appl. Math.*, 71(5):1578–1605, 2011.
- [132] H. J. Wang, C. S. Changchien, C. H. Hung, E. L. Eng, W. C. Tung, K. M. Kee, C. H. Chen, T. H. Hu, C. M. Lee, and S. N. Lu. Fibroscan and ultrasonography in the prediction of hepatic fibrosis in patients with chronic viral hepatitis. *J. Gastroenterol.*, 44:439–436, 2009.
- [133] C. W. Washington and M. I. Miga. Modality independent elastography (MIE): a new approach to elasticity imaging. *IEEE Trans. Med. Imag.*, 23(9):1117–1128, 2004.
- [134] S. Wejcinski, A. Farrokh, S. Weber, A. Thomas, T. Fischer, T. Slowinski, W. Schmidt, and F. Degenhardt. Multicenter study of ultrasound real-time tissue elastography in 779 cases for the assessment of breast lesions: improved diagnostic performance by combining the BI-RADS®-US classification system with sonoelastography. *Ultraschall Med.*, 31:484–491, 2010.
- [135] T. Widlak and O. Scherzer. Hybrid tomography for conductivity imaging. *Inverse Probl.*, 28(8):084008, 2012.
- [136] T. Widlak and O. Scherzer. Stability in the linearized problem of quantitative elastography. *Inverse Probl.*, 31:035005, 2015.
- [137] D. A. Woodrum, A. J. Romano, A. Lerman, U. H. Pandya, D. Brosh, P. J. Rossman, L. O. Lerman, and R. L. Ehman. Vascular wall elasticity measurement by magnetic resonance imaging. *Magn. Reson. Med.*, 56:593–600, 2006.
- [138] J. Zahradník and E. Priolo. Heterogeneous formulations of elastodynamic equations and finite-difference schemes. *Geophys. J. Int.*, 120:663–673, 1995.

Bibliography

- [139] T. Zakaria, Z. Qin, and R. L. Maurice. Optical flow-based B-mode elastography: application in the hypertensive rat carotid. *IEEE Trans. Med. Imag.*, 29(2):570–578, 2010.
- [140] E. Zhang, J. Laufer, and P. Beard. Backward-mode multiwavelength photoacoustic scanner using a planar Fabry-Perot polymer film ultrasound sensor for high-resolution three-dimensional imaging of biological tissues. *App. Opt.*, 47:561–577, 2008.
- [141] Y. Zhang, R. T. Brodell, E. N. Mostow, C. J. Vinyard, and H. Marie. *In vivo* skin elastography with high-definition optical videos. *Skin Res. Technol.*, 15:271–282, 2009.
- [142] P. Zhou and K. E. Goodson. Subpixel displacement and deformation gradient measurement using digital image/speckle correlation (DISC). *Opt. Eng.*, 40(8):1613–1620, 2001.

Abstracts

Abstract in english

While classical imaging methods, such as ultrasound, computed tomography or magnetic resonance imaging, are well-known and mathematically understood, a host of physiological parameters relevant for diagnostic purposes cannot be obtained by them. This gap is recently being closed by the introduction of hybrid, or coupled-physics imaging methods. They connect more than one physical modality, and aim to provide quantitative information on optical, electrical or mechanical parameters with high resolution.

Central to this thesis is the mechanical contrast of elastic tissue, especially Young's modulus or the shear modulus. Different methods of qualitative elastography provide interior information of the mechanical displacement field. From this interior data the nonlinear inverse problem of quantitative elastography aims to reconstruct the shear modulus. In this thesis, the elastography problem is seen from a hybrid imaging perspective; methods from coupled-physics inspired literature and regularization theory have been employed to recover displacement and shear modulus information.

The overdetermined systems approach by G. Bal is applied to the quantitative problem, and ellipticity criteria are deduced, for one and several measurements, as well as injectivity results. Together with the geometric theory of G. Chavent, the results are used for analyzing convergence of Tikhonov regularization. Also, a convergence analysis for the Levenberg Marquardt method is provided.

As a second mainstream project in this thesis, elastography imaging is developed for extracting displacements from photoacoustic images. A novel method is provided for texturizing the images, and the optical flow problem for motion estimation is shown to be regularized with this texture generation. The results are tested in cooperation with the Medical University Vienna, and the methods for quantitative determination of the shear modulus evaluated in first experiments.

In summary, the overdetermined systems approach is seen to have powerful connections to the theoretical analysis of the elastography problem, and a novel method for photoacoustic elastography was developed for the qualitative and quantitative imaging problem.

Zusammenfassung auf deutsch

Während klassische bildgebende Verfahren wie Ultraschall, Computertomographie oder magnetische Resonanz-Tomographie wohlbekannt sind und mathematisch gut verstanden werden, gibt es eine Vielzahl an physiologischen Parametern von diagnostischer Relevanz, die durch jene Verfahren nicht abgebildet werden können. Diese Lücke wird seit einiger Zeit durch Einführung hybrider Methoden, bzw. Methoden mit gekoppelter Physik, zu schließen versucht. Diese Methoden verbinden mehr als eine physikalische Modalität und zielen darauf ab, quantitative Informationen über optische, elektrische oder mechanische Parameter mit hoher Auflösung zu gewinnen.

Im Mittelpunkt dieser Dissertation steht der mechanische Kontrast elastischer Gewebe, besonders der Young'sche Modul bzw. der Schermodul.

Verschiedene Methoden der qualitativen Elastographie stellen innere Informationen des mechanischen Verschiebungsfeldes zur Verfügung. Von diesen inneren Daten zielt das nichtlineare Problem der quantitativen Elastographie darauf ab, den Schermodul zu rekonstruieren.

In dieser Dissertation wird das Rekonstruktionsproblem der Elastographie aus der Perspektive der hybriden Bildgebungsmethoden gesehen; Methoden der Literatur über gekoppelte Physik-Verfahren und die Theorie der Regularisierungsmethoden wurden eingesetzt, um die Information über Verschiebung und den Schermodul zu gewinnen.

Der Ansatz von G. Bal, das Problem als überdeterminiertes System zu betrachten, wird auf das quantitative Bildgebungsproblem angewendet, und Elliptizitätskriterien werden für Probleme mit einem oder mehreren Messdaten abgeleitet, sowie Eindeutigkeitsresultate. Zusammen mit der Theorie von G. Chavent werden die Resultate dafür verwendet, die Konvergenz der Tikhonov-Regularisierung zu analysieren. Ebenso wird eine Konvergenzanalyse für das Levenberg-Marquardt-Verfahren gegeben. Als zweites Hauptstück dieser Dissertation wird elastographische Bildgebung dafür verwendet, die Verschiebung aus photoakustischen Bildern zu extrahieren. Eine neue Methode wurde gefunden, diese Bilder mit Textur zu versehen; es wird gezeigt, dass diese Methode das optische Fluss-Problem zur Abschätzung der Verschiebung regularisiert. Die Ergebnisse wurden in Zusammenarbeit mit der Medizinischen Universität Wien getestet, und die Methoden für quantitative Bestimmung des Schermoduls in ersten Experimenten evaluiert.

Zusammenfassend wird gezeigt, dass der Ansatz der überdeterminierten Systeme über bedeutende Verbindungen zur theoretischen Analyse des Elastographie-Problems hat, und eine neue Methode für photoakustische Elastographie wird entwickelt, die das qualitative als auch das quantitative Bildgebungsproblem adressiert.

Zusammenfassung auf deutsch

Während klassische bildgebende Verfahren wie Ultraschall, Computertomographie oder magnetische Resonanz-Tomographie wohlbekannt sind und mathematisch gut verstanden werden, gibt es eine Vielzahl an physiologischen Parametern von diagnostischer Relevanz, die durch jene Verfahren nicht abgebildet werden können. Diese Lücke wird seit einiger Zeit durch Einführung hybrider Methoden, bzw. Methoden mit gekoppelter Physik, zu schließen versucht. Diese Methoden verbinden mehr als eine physikalische Modalität und zielen darauf ab, quantitative Informationen über optische, elektrische oder mechanische Parameter mit hoher Auflösung zu gewinnen.

Im Mittelpunkt dieser Dissertation steht der mechanische Kontrast elastischer Gewebe, besonders der Young'sche Modul bzw. der Schermodul.

Verschiedene Methoden der qualitativen Elastographie stellen innere Informationen des mechanischen Verschiebungsfeldes zur Verfügung. Von diesen inneren Daten zielt das nichtlineare Problem der quantitativen Elastographie darauf ab, den Schermodul zu rekonstruieren.

In dieser Dissertation wird das Rekonstruktionsproblem der Elastographie aus der Perspektive der hybriden Bildgebungsmethoden gesehen; Methoden der Literatur über gekoppelte Physik-Verfahren und die Theorie der Regularisierungsmethoden wurden eingesetzt, um die Information über Verschiebung und den Schermodul zu gewinnen.

Der Ansatz von G. Bal, das Problem als überdeterminiertes System zu betrachten, wird auf das quantitative Bildgebungsproblem angewendet, und Elliptizitätskriterien werden für Probleme mit einem oder mehreren Messdaten abgeleitet, sowie Eindeutigkeitsresultate. Zusammen mit der Theorie von G. Chavent werden die Resultate dafür verwendet, die Konvergenz der Tikhonov-Regularisierung zu analysieren. Ebenso wird eine Konvergenzanalyse für das Levenberg-Marquardt-Verfahren gegeben. Als zweites Hauptstück dieser Dissertation wird elastographische Bildgebung dafür verwendet, die Verschiebung aus photoakustischen Bildern zu extrahieren. Eine neue Methode wurde gefunden, diese Bilder mit Textur zu versehen; es wird gezeigt, dass diese Methode das optische Fluss-Problem zur Abschätzung der Verschiebung regularisiert. Die Ergebnisse wurden in Zusammenarbeit mit der Medizinischen Universität Wien getestet, und die Methoden für quantitative Bestimmung des Schermoduls in ersten Experimenten evaluiert.

Zusammenfassend wird gezeigt, dass der Ansatz der überdeterminierten Systeme über bedeutende Verbindungen zur theoretischen Analyse des Elastographie-Problems hat, und eine neue Methode für photoakustische Elastographie wird entwickelt, die das qualitative als auch das quantitative Bildgebungsproblem adressiert.

Curriculum vitae

Education

2013-2014	University assistant (with teaching) at the Computational Science Center, University of Vienna
2011-2015	Doctoral studies in mathematics: “Elastography as a hybrid imaging technique” at the Computational Science Center, University of Vienna, Austria, supervised by Univ.-Prof. Dr. Otmar Scherzer
2011:	Master’s degree in mathematics with distinction: “Hybrid Impedance Tomography” at the Computational Science Center, University of Vienna, Austria, supervised by Univ.-Prof. Dr. Otmar Scherzer
2010:	Master’s degree in philosophy with distinction Title of thesis: “Molyneux’ question in British Empiricism”, Faculty for Philosophy and Education, University of Vienna

Research Interests

hybrid and coupled-physics imaging, inverse problems, image processing, optical flow, vision

Teaching

- Course for 2nd term: “Übungen zur Einführung in die Analysis” (Faculty of Mathematics, University of Vienna, summer term 2014; 33 participants)
- Course for freshmen in mathematics: “Tutorium zur Einführung ins mathematische Arbeiten” (Faculty of Mathematics, University of Vienna, winter term 2013; together with teaching assistant, in total 120 participants)
- Work as a private tutor

Talks at workshops and international conferences

- *Stability in linearized quantitative elastography*. Workshop on Theoretical and Applied Computational Inverse Problems. Vienna (Austria), May 6, 2014.

Curriculum vitae

- (together with T. Glatz) *Texture generation for PAI elastography*. Internal PAI workshop. Obergurgl (Austria), March 8, 2014.
- *Stability for quantitative elastographic reconstruction*. CSASC 2013: Joint Mathematical Conference of the Catalan Mathematical Society, Slovenian Mathematical Society, Austrian Mathematical Society, Slovak Mathematical Society, and Czech Mathematical Society. Koper (Slovenia), June 11, 2013.
- *Multi-frame optical flow with application for elastography*. Project meeting. Bratislava (Slovakia), July 25, 2013.
- *Conductivity imaging by acoustical detection*. Internal PAI workshop. Linz (Austria), October 24, 2011.
- *Approaches to hybrid conductivity imaging*. 7th International Congress on Industrial and Applied Mathematics (ICIAM 2011): Minisymposium on “Hybrid methods in medical imaging”. Vancouver (Canada), July 22, 2011.

Other activities

- Organization of minisymposium on *Multi-Frame Motion Estimation and Optical Flow Algorithms*, SIAM Conference on Imaging, May 2014, Hong Kong.
- Poster, together with W. Naetar: *Hybrid conductivity imaging*. Introductory Workshop on Inverse Problems. Cambridge (UK), July 26, 2011.

Publications

- (in preparation) T. Widlak and O. Scherzer. *Convergent regularization methods for quantitative elastography*. University of Vienna, Austria, 2015.
- J. Schmid, B. Zabihian, T. Widlak, T. Glatz, M. Liu, W. Drexler and O. Scherzer. *Texture generation in compressional photoacoustic elastography*. *Proceedings of SPIE*, 9323–100, 2015.
- T. Widlak and O. Scherzer. *Stability in the linearized problem of quantitative elastography*. *Inverse Problems*, 31(3):035005, 2015.
- T. Glatz, O. Scherzer, and T. Widlak. *Texture generation for photoacoustic elastography*. *Journal of Mathematical Imaging and Vision*, (published online first) 2015.
- T. Widlak and O. Scherzer. *Hybrid tomography for conductivity imaging*. *Inverse Problems*, 28(8):084008, 2012.